FEASIBILITY STUDY OF A SYNTHESIS PROCEDURE FOR ARRAY FEEDS TO IMPROVE RADIATION PERFORMANCE OF LARGE DISTORTED REFLECTOR ANTENNAS

SEMIANNUAL STATUS REPORT

submitted to
NASA Langley Research Center
for
Grant No. NAG-1-859

by

W.L. Stutzman
K. Takamizawa
P. Werntz
J. LaPean
R. Barts
B. Shen

Virginia Polytechnic Institute and State University
Bradley Department of Electrical Engineering
Blacksburg, Virginia 24061-0111

SATCOM Report No. 92-4

September 1992

semiannu.al
10/21/92

TABLE OF CONTENTS

I. INTRODUCTION

1.1 Project Organization

Virginia Tech has several activities which support the NASA Langley effort in the area of large aperture radiometric antenna systems. These activities are summarized in Table 1.1-1. This semi-annual report reports on all of these.

Table 1.1-2 lists major reflector antenna research areas at Virginia Tech together with the graduate students responsible for the work.

Table 1.1-1

Personnel at Virginia Tech Performing Reflector Antenna Research

Reflector Antenna Research at Virginia Tech

1. "Feasibility Study of a Synthesis Procedure for Array Feeds to Improve Radiation Performance of Large Distorted Reflector Antennas"
   GAs: Ko Takamizawa, Jim LaPean, Paul Werntz, B. Shen
   Project: NASA Grant NAG-1-859; VT 4-26132
   Term: 02/25/88 - 12/31/92

Personnel Active in Reflectors but not Supported by NASA

2. R. Michael Barts
   "Design of Array Feeds for Large Reflector Antennas," NASA Graduate Researchers Program Grant NGT-50413; completed, but work continues.

3. Derrick Dunn, M.S. student
   Support: GEM Fellowship (6/91 to 12/92); NASA Traineeship (1/93 -)

Table 1.1-2

Reflector Antenna Research Activities at Virginia Tech

I. Technology Development

1.1. Operation and testing of full commercial reflector code (GRASP7) - Takamizawa

1.2. Documentation of analysis techniques for reflector computations - Takamizawa

1.3. Canonical cases - Dunn

1.4. Beam efficiency studies - Shen

II. Wide Scanning Antenna Systems

2.1. Documentation of wide scanning antenna principles - Werntz

2.2. Type 1 dual-reflector design - LaPean

2.3. Type 2 tri-reflector antenna design - Werntz

2.4. Support of Type 1 and 2 hardware model - LaPean and Werntz

2.5. Spherical reflector antenna designs - Shen

2.6. Other concepts

Cylindrical reflector family

Toroidal reflector family

Hybrid concepts

III. Reflector System Optimization - Takamizawa

3.1. Comparison of optimization techniques

3.2. Error functional definition

IV. Arrays for Large Radiometric Antennas - Barts

4.1. Analysis techniques in lossy radiometric systems using arrays.

4.2. Feed array architectures for radiometers

4.3. Feed component technology readiness evaluation

4.4. Calibration issues

1.2 Summary of Configurations Designed for Wide Scanning

Three basic reflector configurations have been extensively evaluated. These three designs, which are listed in Table 1.2-1, provide a range of options for future system constraints. They essentially provide a tradeoff in scan performance with mechanical complexity.

Subsequent chapters give the details on the analysis results. Here we summarize performance results and mechanical characteristics. The configuration geometry is common to all configuration. The z-axis is normal to the aperture plane and is the main beam direction for zero scan. The xz-plane is the plane of offset. Below are listed the common electrical performance parameters.

Frequencies: 18 and 37 GHz, plus others as needed.

Polarization: Linear, x-directed

Main reflector projected aperture size (D): 10.63 m

Scan planes:

θ = maximum of stated scan range

ϕ = 0°, 45°, 90°, 135°, 180°

Crosspolarization (XPOL):

Peak crosspolarization relative to scanned main beam peak over the main beam.

Aperture efficiency (ϵ_{ap}):

Ratio of actual gain to the gain of a uniform amplitude-uniform phase aperture of the same size as the entire main reflector.

Beam efficiency (BE):

Beam solid angle contained in the main beam out to 2.5 times the no-scan half power beamwidth divided by the beam solid angle of the entire pattern.

Results are presented for the 10.63 m diameter LaRC test article. The results can be applied directly to the long term goal case of a 25-m diameter main reflector by frequency scaling. That is, our study case represents the following

D = 10.63 m = 638 λ @ 18 GHz

D = 10.63 m = 1311 λ @ 37 GHz

and results apply to

D = 25 m = 638 $\lambda \Rightarrow$ f = 7.7 GHz

D = 25 m = 1311 $\lambda \Rightarrow$ f = 15.7 GHz

Table 1.2-1 compares the electrical performance parameter values for the three configurations for the worst case scan position over the intended scan range. Table 1.2-2 gives the exact geometries and reflector sizes for each configuration.

With complex geometries such as these antenna systems, it is necessary to investigate sensitivities to position and angle errors. This was done for the Type 1 and spherical reflector antennas; see Tables 1.2-3 and -4. (Tests were not performed at 37 GHz due to excessive computer run time.) The results indicate that there are no special sensitivities in these geometries.

Comparison of the three configurations show that Type 1 (formerly called Type 6) is spillover limited and not phase-error limited. So in spite of its limited scan range, the Type 1 antenna performs well with frequency increase; also, the implication of spillover loss on radiometric performance are much less severe than phase error loss. The Type 2 structures are phase-error limited, but offer much wider scan than the Type 1 antenna. The spherical reflector suffers from neither increasing spillover or phase error loss with frequency. If the mechanical motion of the flat mirror (and possibly feed tilting) are allowed, the spherical configuration is an excellent choice.

1.3 Test Approach

Table 1.3-1 lists our recommendations for a hardware test plan.

Table 1.3-1
Recommended Test Plan

A. Using ACTS 2.7 meter Reflector
   1. Repeat one experiment for which previous data are available.
   2. Type 2 manual motion
      Manually position tertiary reflector to scan beam.
   3. Type 2 with actuated tertiary.
   4. Type 2 (with actuated tertiary) and an array feed to scan in offset plane.
   5. Type 2 with a reconfigurable tertiary.

   NOTE: Tests 2, 3, 4, and 5 should be done at two frequencies (12 and 18 GHz).

B. Offset Spherical Reflector
   1. Obtain an offset (main) reflector similar in size.
   2. Build and test shaped dual subreflectors and flat minor.

Table 1.2-1

Summary of Wide Scanning Reflector Performance Characteristics - Results from Electromagnetic Design and Evaluation at 18 GHz

Type	Main Reflector Size	Electromagnetic Performance at the Scan Limit Which Yields Maximum Gain Loss						
		Gain Loss (dB)	Aperture Efficiency (%)	Beam Efficiency (%)	HP (deg)	$BW_{10\ dB}$ (deg)	Sidelobe Level (dB)	XPOL (dB)
1. Offset Cassegrain (max scan angles: $\theta = 0.5°$, $\phi = 0°$)	D = 10.63 m	0.76	62.30	89.77	0.13°	0.21°	-22.78	-53.90
2. Offset Tri-Reflector-Cassegrain II (max scan angles: $\theta = 5°$, $\phi = 90°$)	D = 8 m	1.05	60.60	95.42	0.17°	0.3	-19.39	-25.24
3. Spherical main reflector: Tri-reflector with a flat mirror* (max scan angles: $\theta = 5°$, ϕ = any)	10 x 12 m	0.4 dB	50	92	0.15°	0.27°	-28	-25

* Gaussian feed with -15 dB taper at ±22.4° (15 GHz results extrapolated to 18 GHz)

Table 1.2-2

Summary of Wide Scanning Reflector Configuration Characteristics

	Reflector Shapes				Suboptics Sizes (fractional area of main reflector)				Motion at Scan Limit			
Type	Main	Sub	Tertiary	Mirror	Sub	Tertiary	Mirror	Area Eff.*	Sub	Tertiary	Mirror	Feed
1. Offset Cassegrain Design scan range: 1.0° half-cone	Parabolic	Hyperbolic	---	---	1.5m (14%)	None	None	98%	Δx:±0.25m Δy:±0.25m Δz:0 to 0.5m α,β:±7°	NA	NA	Fixed
2. Offset Tri-Reflector Design scan range: ±2.5°, ±5°	Parabolic	Shaped	Shaped	---	3.16x2.1 (10.3%)	1.45x1.38 (3.1%)	None	87%	No Motion	α=±7.7% β=±16°	N/A	Fixed
3. Spherical main reflector (tri-reflector with a flat mirror) Design scan range: ±5°	Spherical	Shaped	Shaped	Flat	3.2x4.6 (12%)	2.7x4.2 (9.5%)	2.8x4.2 (9.8%)	70%	No Motion	No Motion	Tilted half of θ_s scan and equal to ϕ_s scan	Tilted twice (neg) ϕ_s scan

* Area Efficiency = main reflector area/total area of all reflectors

Table 1.2-3

Summary of Mechanical Error Sensitivity Analysis at 18 GHz - Offset Cassegrain Reflector (Type 1)

	On Axis				At Scan Limit (θ = 0.5°, ϕ = 0°)			
Motion Parameter	Beam Peak Shift	Gain Change	Beam Efficiency Change	Sidelobe Level Change	Beam Peak Shift	Gain Change	Beam Efficiency Change	Sidelobe Level Change
<u>Subreflector</u>								
$\Delta x_2 = 0.5\lambda$	0.02°	0.01 dB	0.03%	0.37 dB	0.02°	0.04 dB	0.07%	0.11 dB
$\Delta y_2 = 0.5\lambda$	0.02°	0.00 dB	0.01%	0.37 dB	0.02°	0.01 dB	0.06%	0.03 dB
$\Delta z_2 = 0.5\lambda$	0.02°	0.02 dB	0.04%	0.01 dB	0.02°	0.01 dB	0.10%	0.05 dB
$\Delta\alpha_2 = 0.1°$	0.03°	0.02 dB	0.02%	0.21 dB	0.02°	0.02 dB	0.23%	0.10 dB
$\Delta\beta_2 = 0.1°$	0.02°	0.01 dB	0.01%	0.15 dB	0.02°	0.00 dB	0.02%	0.04 dB
<u>Feed Position</u>								
$\Delta x_s = 0.5\lambda$	0.01°	0.00 dB	0.01%	0.04 dB	0.01°	0.01 dB	0.05%	0.03 dB
$\Delta y_s = 0.5\lambda$	0.01°	0.00 dB	0.01%	0.07 dB	0.01°	0.00 dB	0.02%	0.06 dB
$\Delta z_s = 0.5\lambda$	0.00°	0.01 dB	0.03%	0.03 dB	0.01°	0.00 dB	0.07%	0.04 dB

Table 1.2-4

Summary of Mechanical Error Sensitivity Analysis at 15 GHz - Spherical Reflector System with Flat Mirror

	On Axis				At Scan Limit: $\theta = 5°$, $\phi = 90°$ ($\theta_s = 10°$, $\phi_s = 26°$)			
Motion Parameter	Beam Peak Shift	Gain Change	Beam Efficiency Change	Sidelobe Level Change (dB)	Beam Peak Shift	Gain Change (dB)	Beam Efficiency Change	Sidelobe Level Change (dB)
Subreflector								
$\Delta x_2 = 0.5\lambda$	0.04°	-0.1 dB		+1.7				
$\Delta z_2 = 0.5\lambda$	-0.04°	-0.14 dB	-0.5%	+ 2				
$\Delta y_2 = 0.5\lambda$	-0.05°	+0.01 dB	-0.1%	+0.03				
Tertiary								
$\Delta x = 0.5\lambda$	-0.02°	-0.01 dB	0%	+0.3				
$\Delta z = 0.5\lambda$	0.00°	-0.01 dB		+0.8				
$\Delta\theta = 0.1°$	-0.09°	-0.2 dB	-0.5%	+0.9	0.07°	-0.3	-0.5%	+0.5
Feed Position								
$\Delta x_s = 0.5\lambda$	0.02°	+0.07 dB	-1.2%	+3				
$\Delta z_s = 0.5\lambda$	0.04°	-0.04 dB		+0.5				

Chapter 2

PERFORMANCE ANALYSIS OF THE CASSEGRAIN TRI-REFLECTOR

Performance results for a tri-reflector antenna configuration (Type 2) designed to be compatible with the primary reflector dimensions of the NASA Langley test article are presented in this chapter. The tri-reflector antenna is synthesized and analyzed using the geometrical optics code TRAS (Tri-Reflector Antenna Synthesis code). Physical optics performance results obtained from GRASP7 are also included.

2.1. Introduction

The reflector configuration shown in Fig. 2-1 is derived from the configuration originally proposed by Peter Foldes. This configuration provides beam scanning with a minimum of subreflector motion and no feed motion. The configuration shown has a 25-m primary aperture diameter. The dimensions of the configuration proposed for use with the NASA test article are related to the dimensions shown in Fig. 2-1 by a scale factor of 8/25.

The configuration shown in Fig. 2-1 is designed for an elliptical scan range subtending $\pm 2.5^\circ$ in the yz-plane and $\pm 5^\circ$ in the xz-plane. Scan angle definitions are defined in Fig. 2-2. Corresponding to the specified scan range and a primary aperture diameter of 8 m, the secondary reflector rim is an ellipse with major axis 2a = 3.16 m and minor axis 2b = 2.1 m. The surface area of the secondary reflector is approximately 10.3% of the area of the primary aperture. The tertiary reflector rim is an ellipse with major axis 2a = 1.45 m and minor axis 2b = 1.38 m. The surface area of the tertiary reflector is approximately 3.1% of the area of the primary reflector. The overall length of the reflector configuration (as measured along the z-axis) is approximately 13.6 m and the overall height (as measured along the x-axis) is approximately 13.0 m.

For beam steering in the unscanned direction (along the z-axis) the average half angle subtended by the tertiary reflector as viewed from the feed position is $\theta_{ave} = 12.94^\circ$. If it is assumed that the feed is a pyramidal horn, an aperture diameter of $d_f \simeq 9.84\ \lambda$ would be required to achieve a -15 dB tertiary reflector edge illumination. While this aperture diameter is very large for a single feed, it is a good size for a small array feed and facilitates efficient feed elements with reasonable aperture diameters.

2.2. Performance Parameters

The tertiary reflector is shaped to produce zero aperture plane phase errors for beam steering along the z-axis. Scanning is accomplished by two degrees of tertiary rotation about point P_r shown in Fig. 2-1. The required motion of the tertiary reflector

for a given scan direction is calculated by TRAS which uses Powell's optimization method. The error function used in the optimization is

$$E = \sum_{i=0}^{M} \sum_{j=0}^{N} w(i,j)\, |\hat{t}_{ij} \times \hat{s}| \tag{2-1}$$

where $\hat{t}_{ij}$ is the unit vector in the direction of the i,j^{th} transmitted ray, $\hat{s}$ is the unit vector in the desired scan direction and $w(i,j)$ is the weighting of the i,j^{th} transmitted ray at the aperture plane as result of a cos^q feed distribution. This error function minimizes the divergence of the transmitted ray from the desired scan direction and therefore minimizes the aperture plane phase errors. Once the optimum tertiary reflector position corresponding to a desired scan direction is obtained, two useful performance parameters are calculated by TRAS.

Primary Aperture Efficiency

If phase errors are ignored, the primary aperture efficiency is affected by spillover at the surfaces of the primary, secondary and tertiary reflectors and the aperture taper efficiency (which is the gain loss relative to a uniformly illuminated aperture due to the design aperture distribution). The primary aperture efficiency is calculated by the following expression [1]:

$$\epsilon_{ap} = \frac{\left(\int\int_{-\infty}^{\infty} fg \; dx \; dy \right)^2}{\int\int_{-\infty}^{\infty} f^2 \; dx \; dy \int\int_{-\infty}^{\infty} g^2 \; dx \; dy} \tag{2-2}$$

where the integrals are evaluated over the aperture of the primary reflector, f is the field amplitude across the aperture due to an incident plane wave and g is the field amplitude across the aperture due to the feed excitation. As formulated, (2-2) includes both aperture taper and spillover effects.

Maximum Aperture Diameter

For a given *rms* phase error across the primary aperture, Φ_{rms}, the Ruze approximation can be used to derive the following useful equation which relates the main reflector diameter in wavelengths, d_M/λ, to the maximum allowed gain loss, G/G_0 [2]:

$$\frac{d_M}{\lambda} = \left\{ \frac{1 - G/G_0}{(\frac{\pi}{r})^2 \Phi_{\text{rms}}} \right\}^{1/2} \tag{2-3}$$

where r is the radius of the primary aperture. In the following examples the maximum allowed gain loss was chosen to be -1 dB ($G/G_0 = 0.7943$).

2.3. Results

Geometrical optics performance results were calculated for the following scan directions:

$$\begin{array}{ll} \phi = 0.0^\circ & \theta = 0.1^\circ - 2.5^\circ \\ \phi = 45.0^\circ & \theta = 0.1^\circ - 3.1^\circ \\ \phi = 90.0^\circ & \theta = 0.1^\circ - 5.0^\circ \\ \phi = 135.0^\circ & \theta = 0.1^\circ - 3.1^\circ \\ \phi = 180.0^\circ & \theta = 0.1^\circ - 2.5^\circ \end{array} \tag{2-4}$$

where for each value of ϕ ten equal increments of θ were used.

The results of the maximum aperture diameter for 1 dB gain loss calculations are shown in Fig. 2-3. The maximum electrical dimension of the primary reflector for the specified scan range and 1 dB of gain loss is $d_M/\lambda = 640$. This corresponds to an operating frequency of 24 GHz for the 8 m diameter aperture. The results of the aperture efficiency calculations are shown in Fig. 2-4. The geometrical optics boundary of illumination at the primary aperture plane is found from the locus of rays which when traced from the feed to the aperture plane intercept the edge of the tertiary. A plot of the illuminated region of the primary aperture for the limiting scan directions in (2-4) are shown in Fig. 2-5. Figure 2-5 demonstrates the high aperture efficiencies possible with the tri-reflector configuration.

Physical optics analysis was performed using GRASP7. Two frequencies were considered 18 GHz and 24 GHz. The results for the 18 GHz calculations are summarized in Table 2-1 and the results for the 24 GHz calculations are summarized in Table 2-2. Principal plane patterns are shown in Figs. 2-6 to 2-11.

For comparison purposes performance results were also calculated for the prime focus parabolic reflector shown in Fig. 2-12. Scanning is accomplished by feed translation. Geometrical optics results are shown in Fig. 2-13. The maximum aperture diameter for 1 dB of gain loss is approximately $d_M/\lambda = 120$ corresponding to an operating frequency of 4.5 GHz for the 8-m diameter aperture. Physical optics analysis was performed using GRASP7 at 3.75 GHz. These results are summarized in Table 2-3. Principal plane patterns are shown in Figs. 2-14 and 2-15.

2.4. Conclusions

- The tri-reflector configuration demonstrates a scan capability of $\pm 2.5^{\circ}$ in the xz-plane and $\pm 5^{\circ}$ in the yz-plane with an elliptical subreflector rim with major axis 2a = 3.16 m and minor axis 2b = 2.1m. A wider scan range would require a larger subreflector.
- The tri-reflector configuration provides both a simple scan mechanism (tertiary reflector motion reduced to two degrees of angular rotation about the point P_r) and a high aperture efficiency.
- For the scan range and tertiary reflector motions considered the maximum diameter of the primary reflector is limited to $d_M \simeq 640\ \lambda$. Preliminary data indicates that if the tertiary reflector is allowed three degrees of motion the maximum electrical diameter could be increased to $d_M \simeq 800\ \lambda$.
- Physical optics results indicate scanning of 80 HPBW[8] in the yz-plane and 40 HPBW[8] in the xz-plane with a gain loss of 1.36 dB.

2.5 Recommendations for Future Work

Specific areas of future concentration are:

- A detailed investigation into possible flight profiles for the remote sensing platform to further specify the necessary scan range.
- A detailed investigation of mechanical tolerances to determine if the feed array size is determined by mechanical considerations or scan induced phase errors.
- A detailed trade-off study between tertiary reflector motion complexity and scan performance.
- Efforts to reduce the dimensions of the tertiary reflector as compared to the dimensions of the primary and secondary reflectors.
- Efforts to increase scan performance using reflector surface optimization.
- Efforts to reduce cross-polarization.
- An investigation into the use of array feeds to improve scan performance.

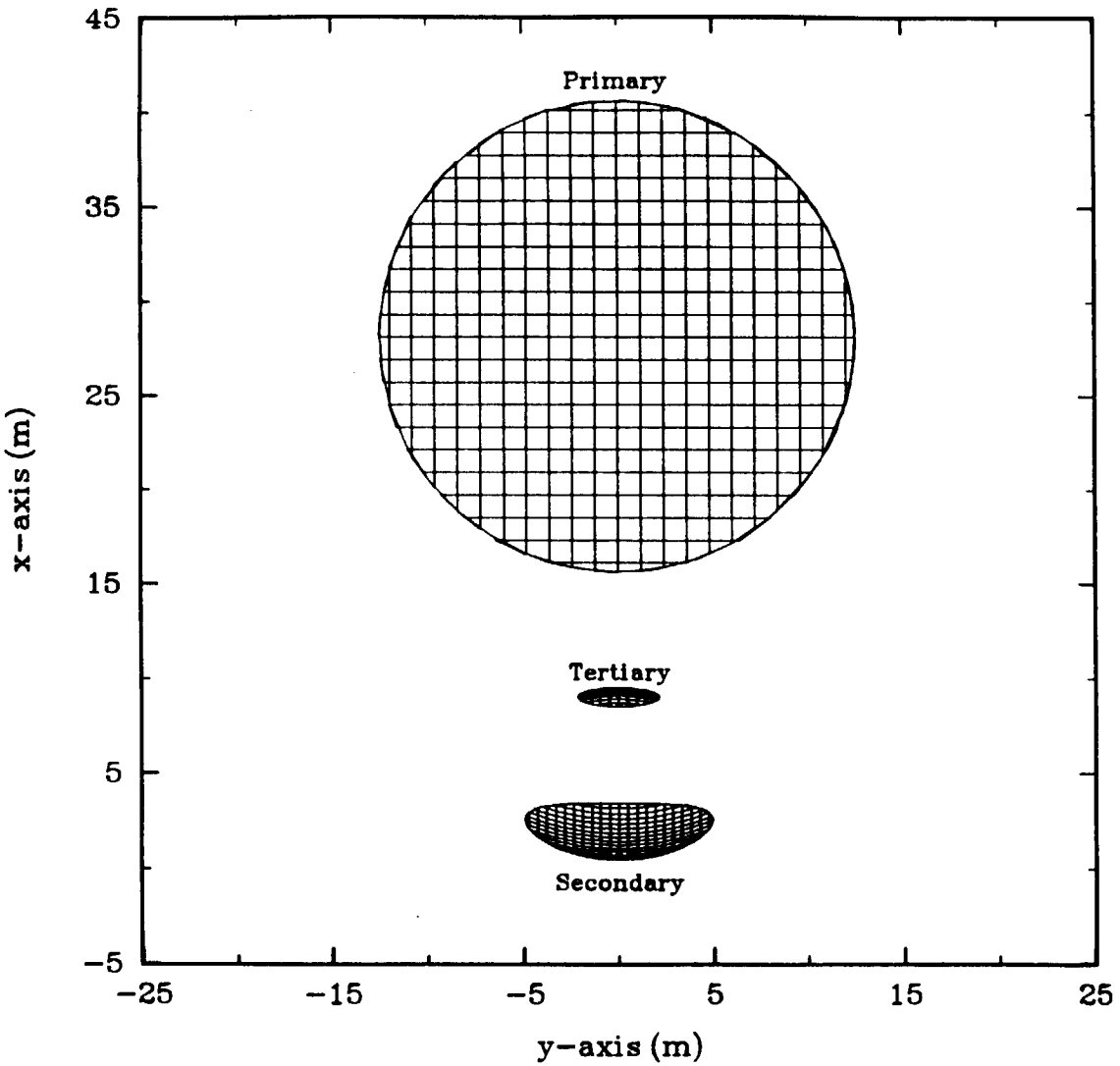

Figure 2-1a. Front view of the Cassegrain tri-reflector (Type 2).

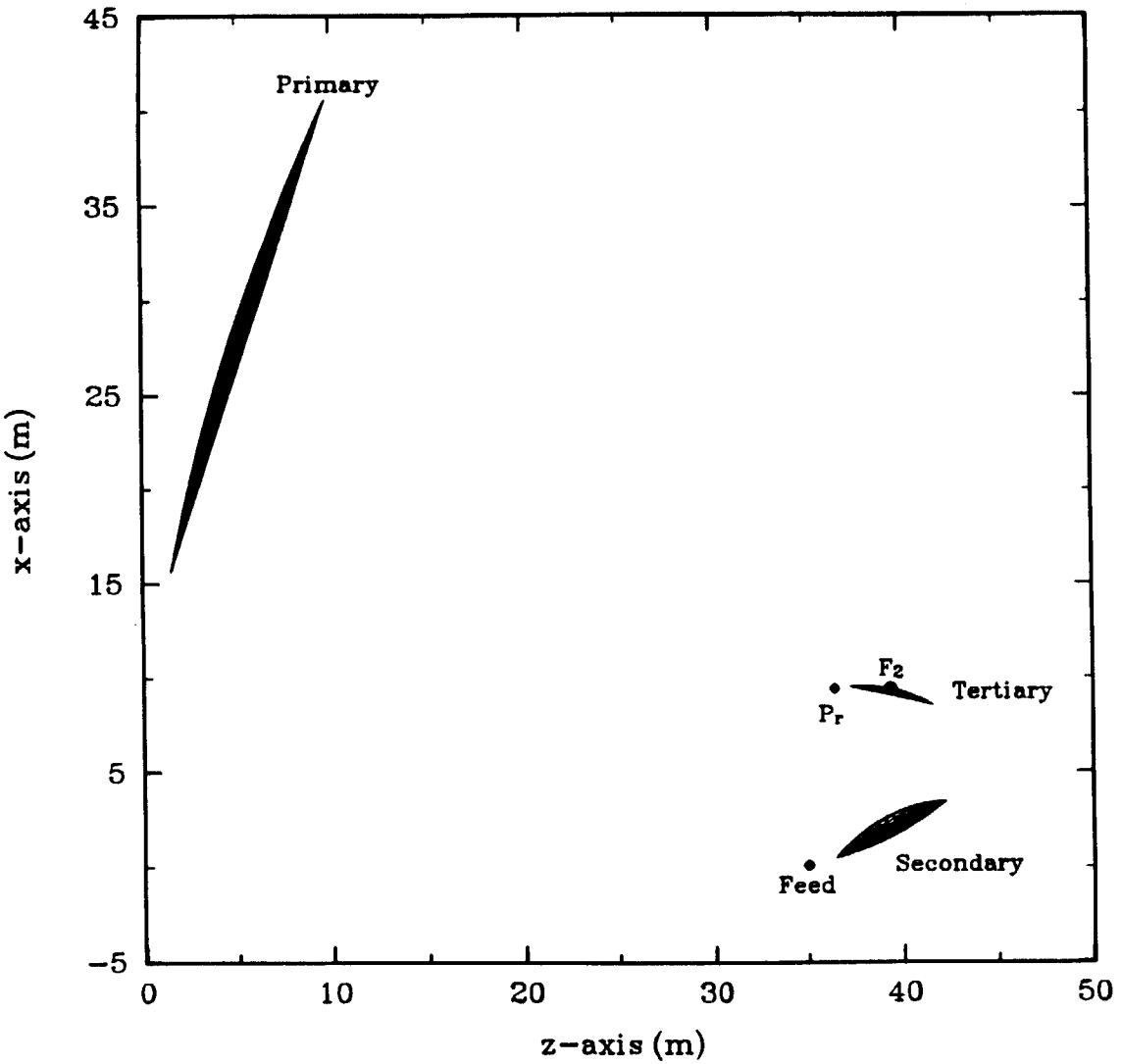

Figure 2-1b. Side view of the Cassegrain tri-reflector (Type 2).

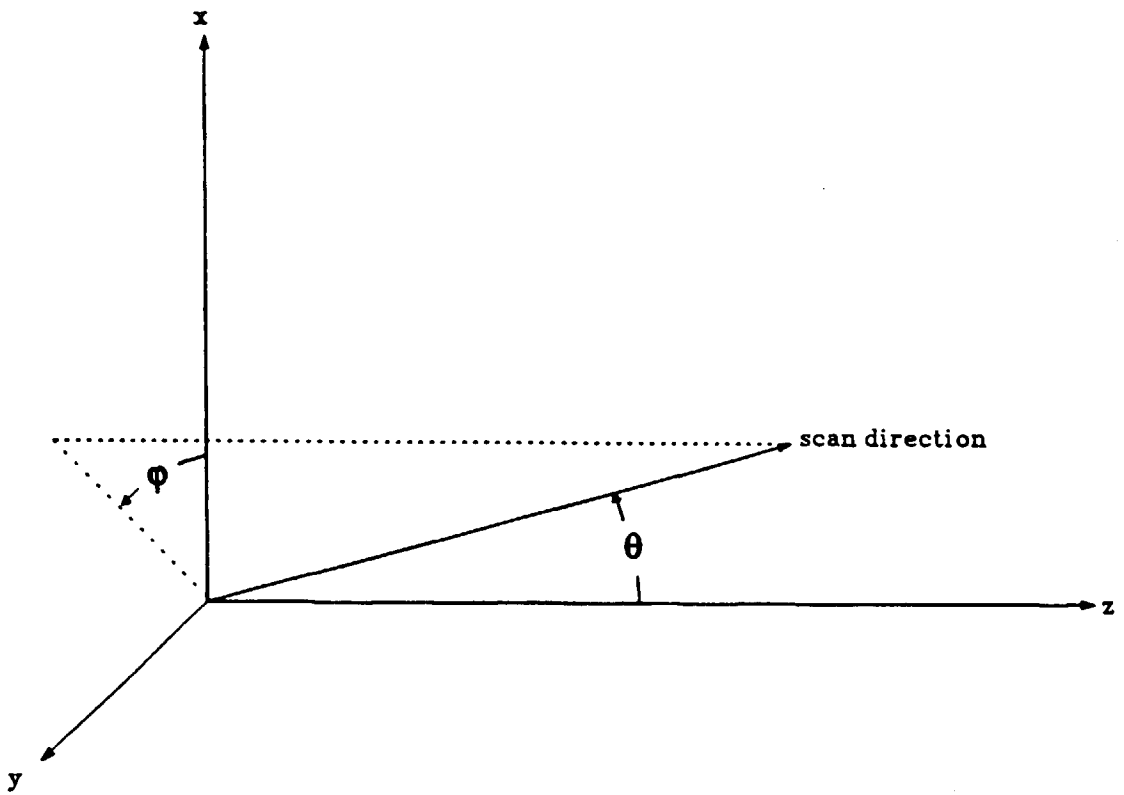

Figure 2-2. Definitions of (θ, ϕ) scan angles.

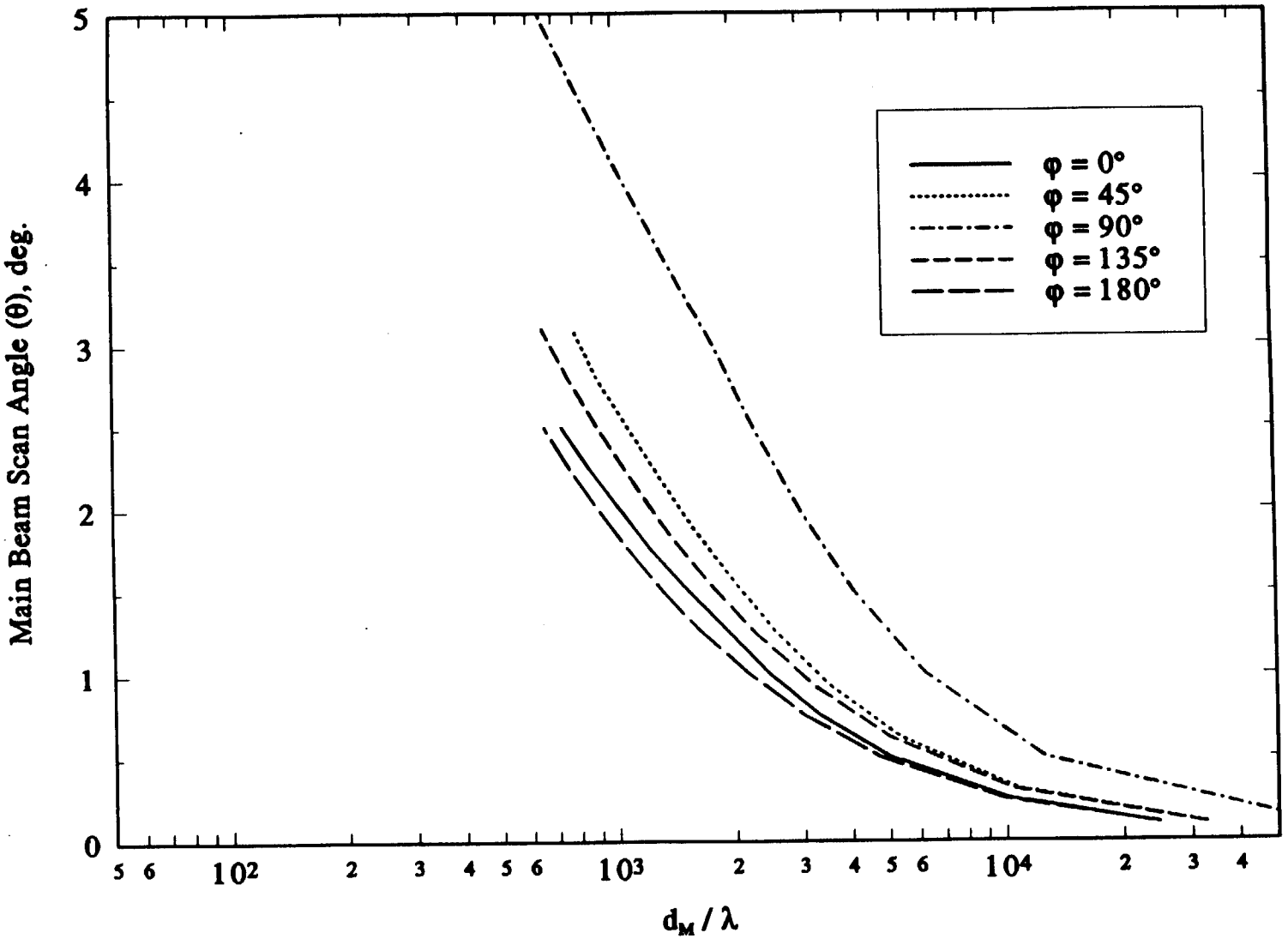

Figure 2-3. Beam scan range for 1-dB gain loss as a function of main reflector diameter of the Type 2 reflector.

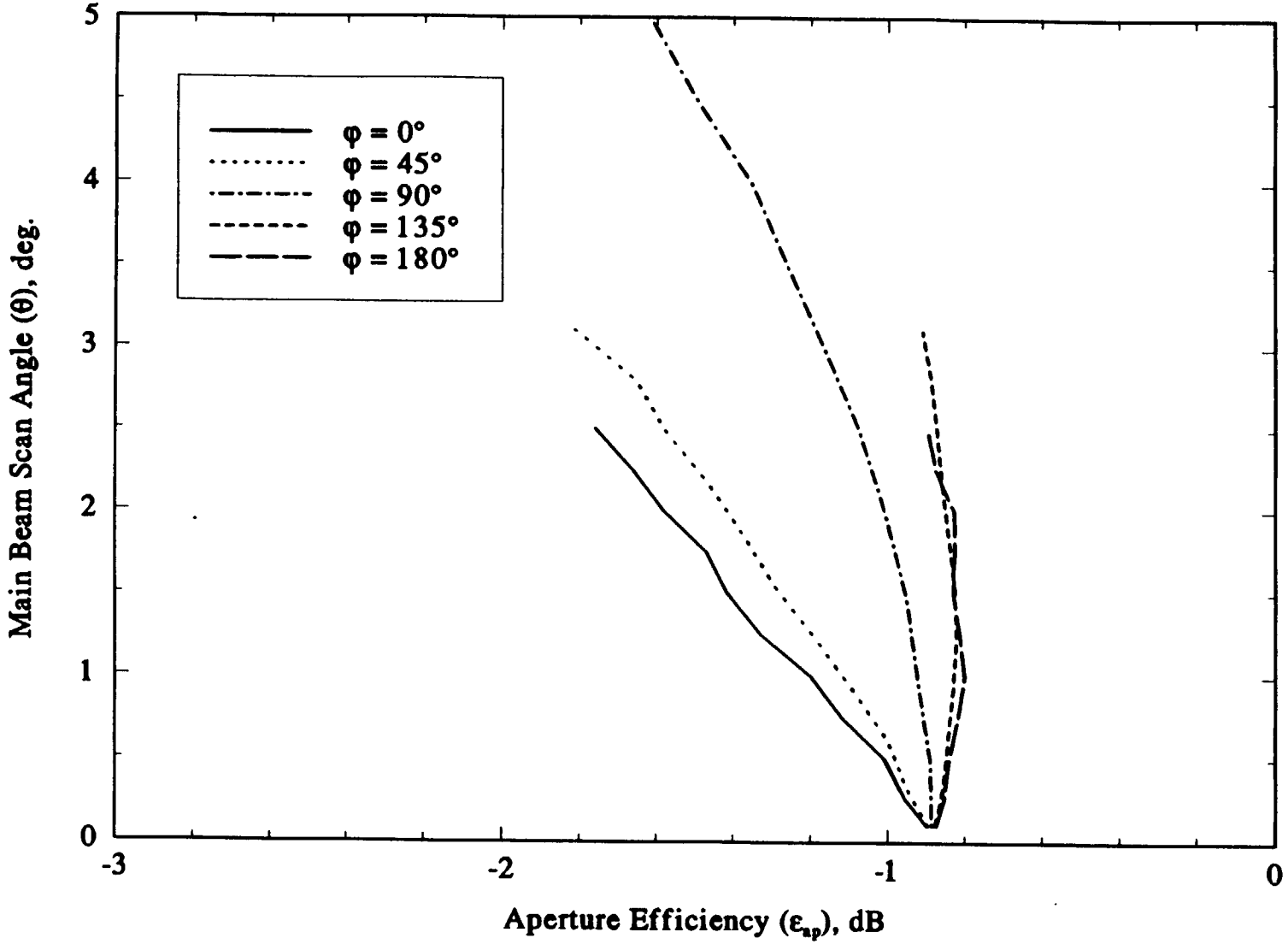

Figure 2-4. Main beam scan angle versus aperture efficiency for the Type 2 reflector.

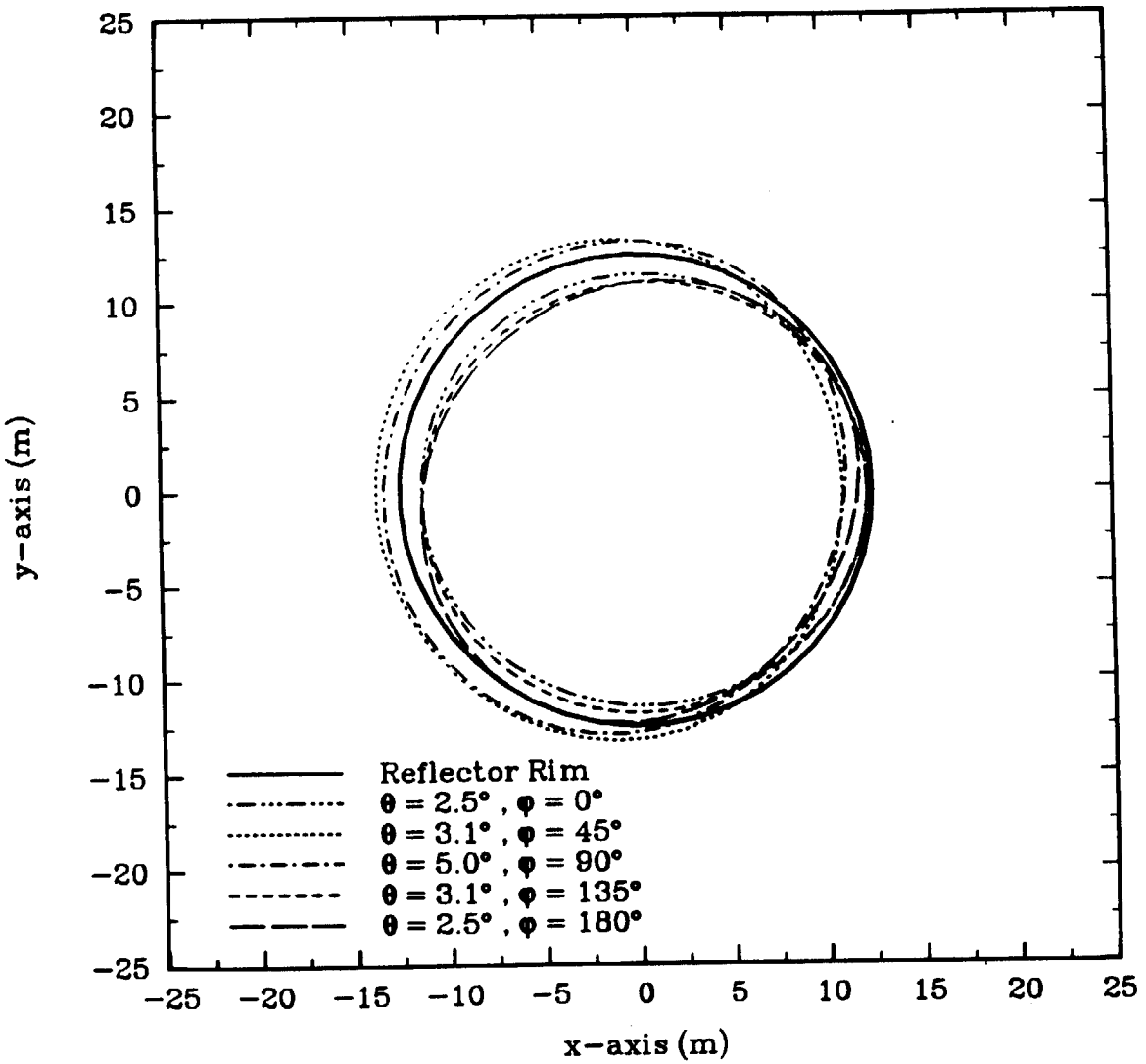

Figure 2-5. Geometrical optics edge ray contours in the aperture plane for various scan directions.

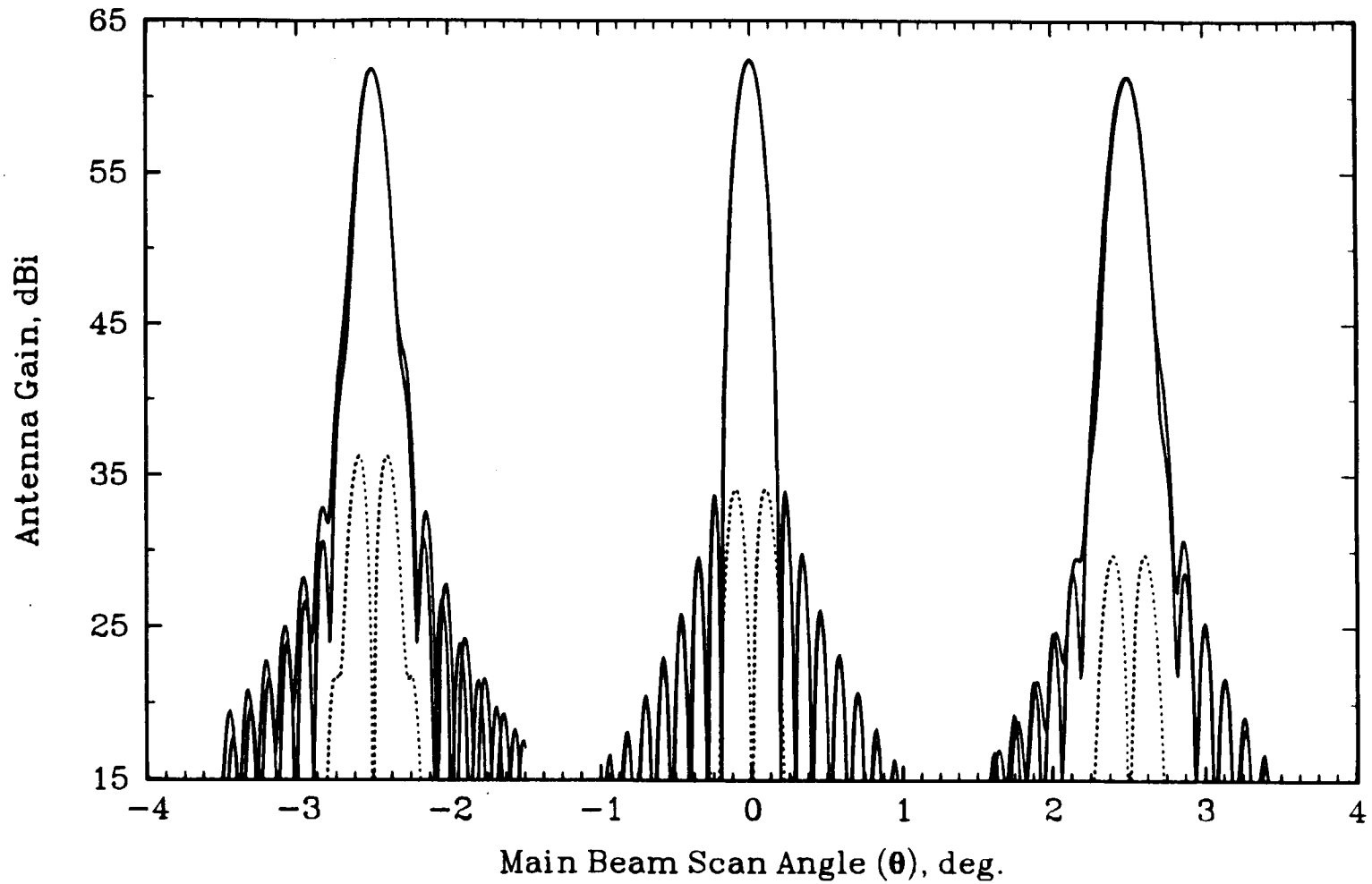

Figure 2-6. Principal plane patterns for θ=-2.5, 0, +2.5° and ϕ=0° scan directions at 18 GHz.

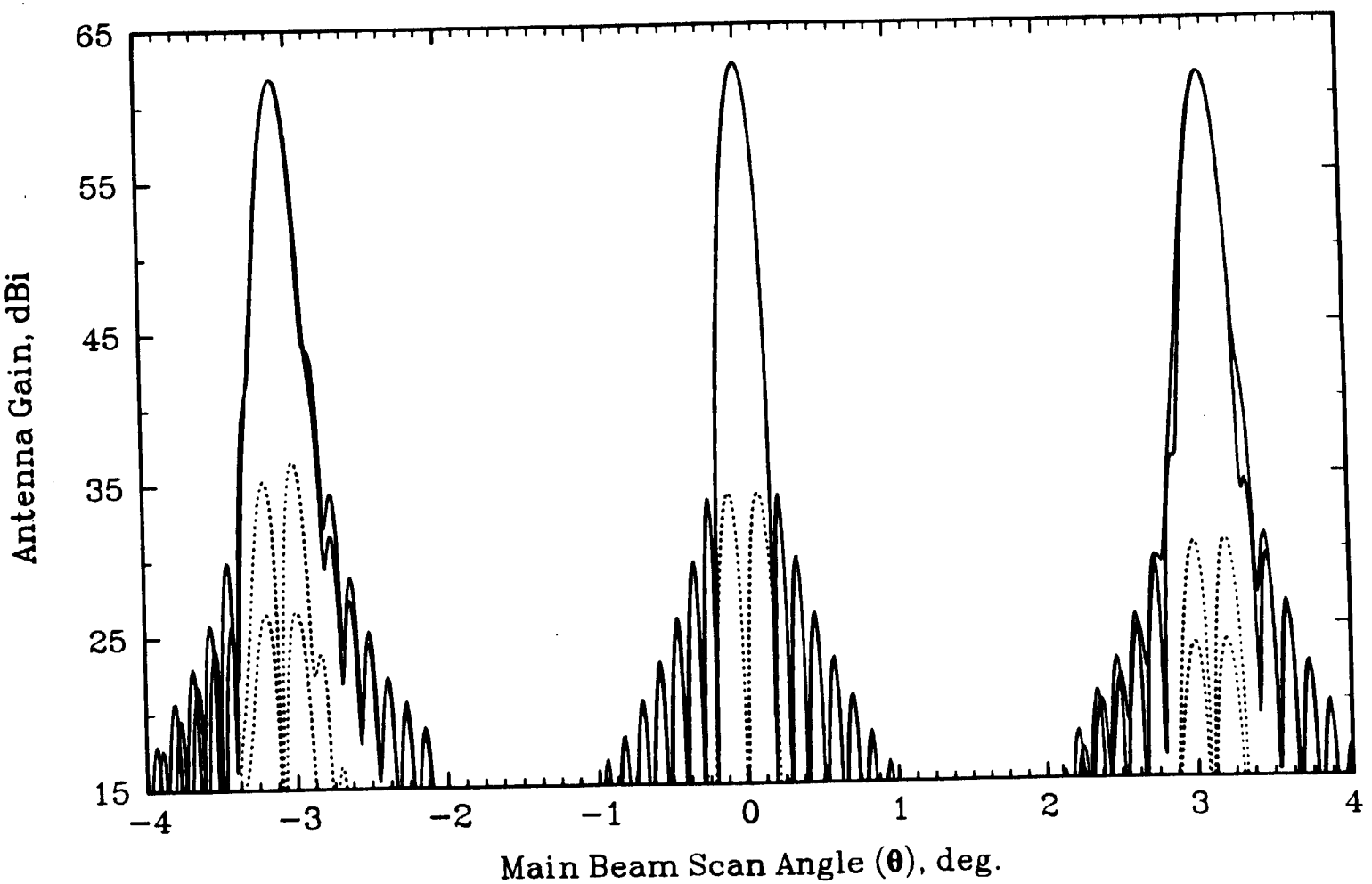

Figure 2-7. Principal plane patterns for θ=-2.5, 0, +2.5° and ϕ=45° scan directions at 18 GHz.

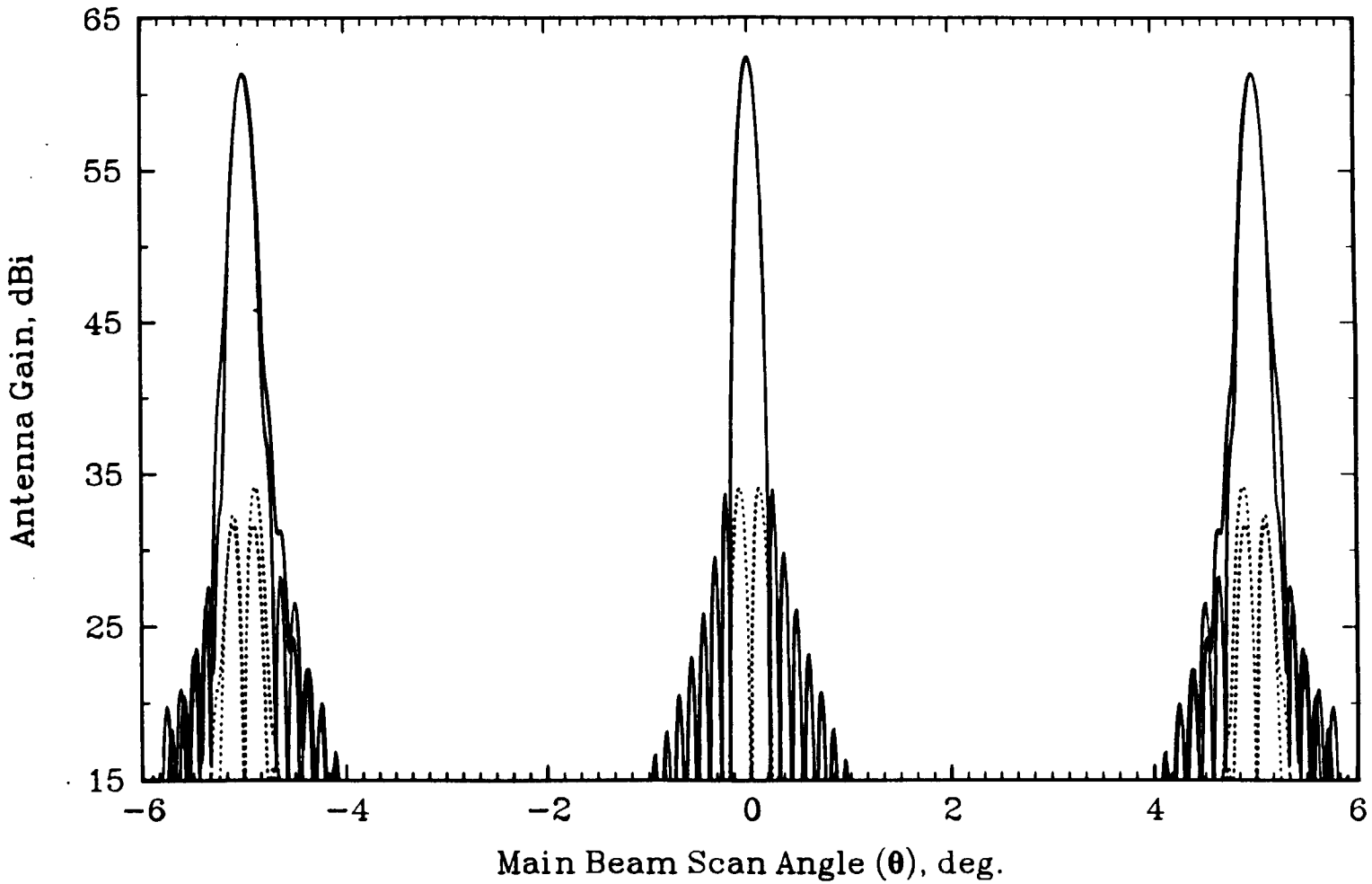

Figure 2-8. Principal plane patterns for θ=-2.5, 0, +2.5° and ϕ=90° scan directions at 18 GHz.

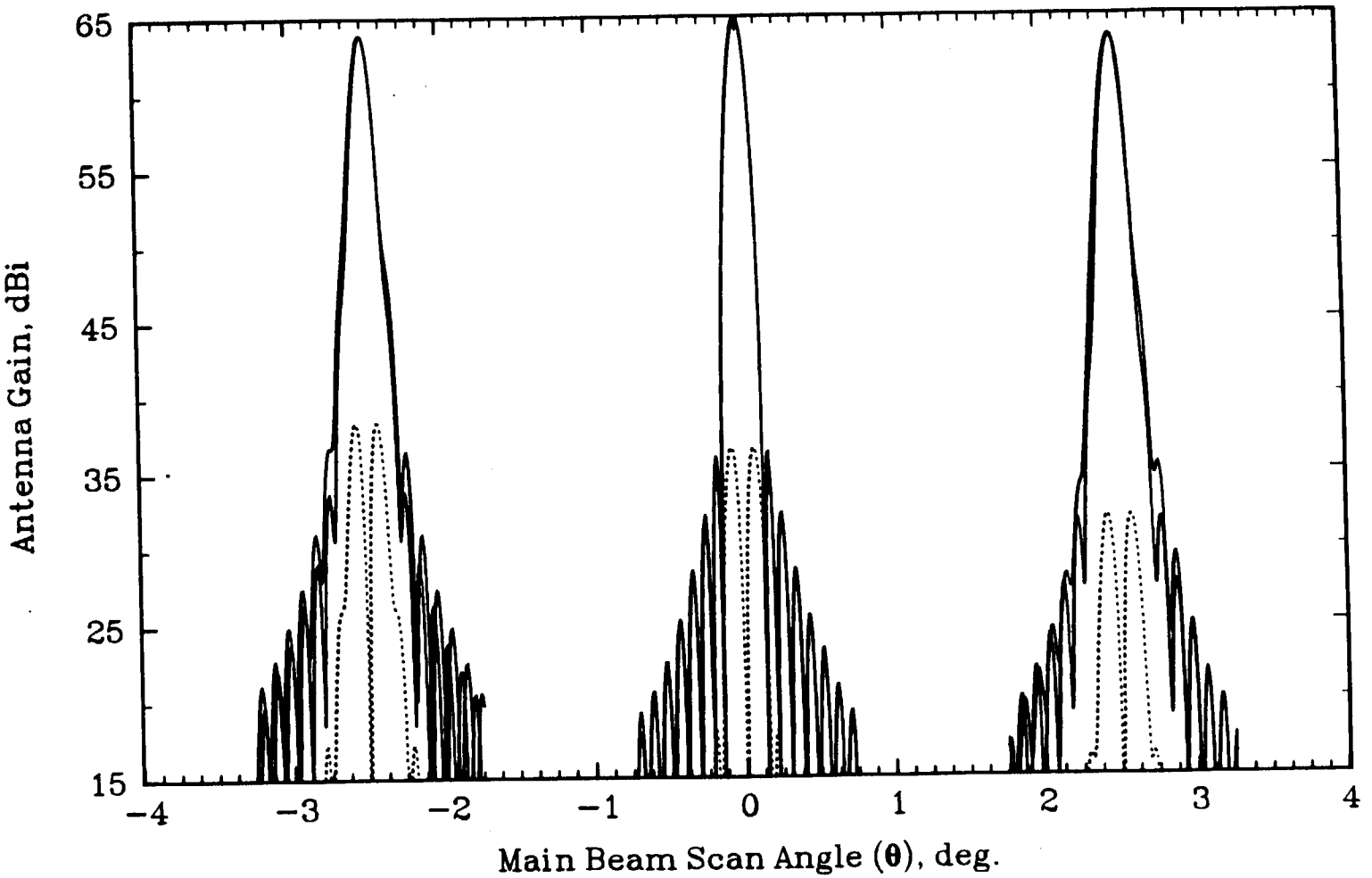

Figure 2-9. Principal plane patterns for θ=-2.5, 0, +2.5° and ϕ=0° scan directions at 24 GHz.

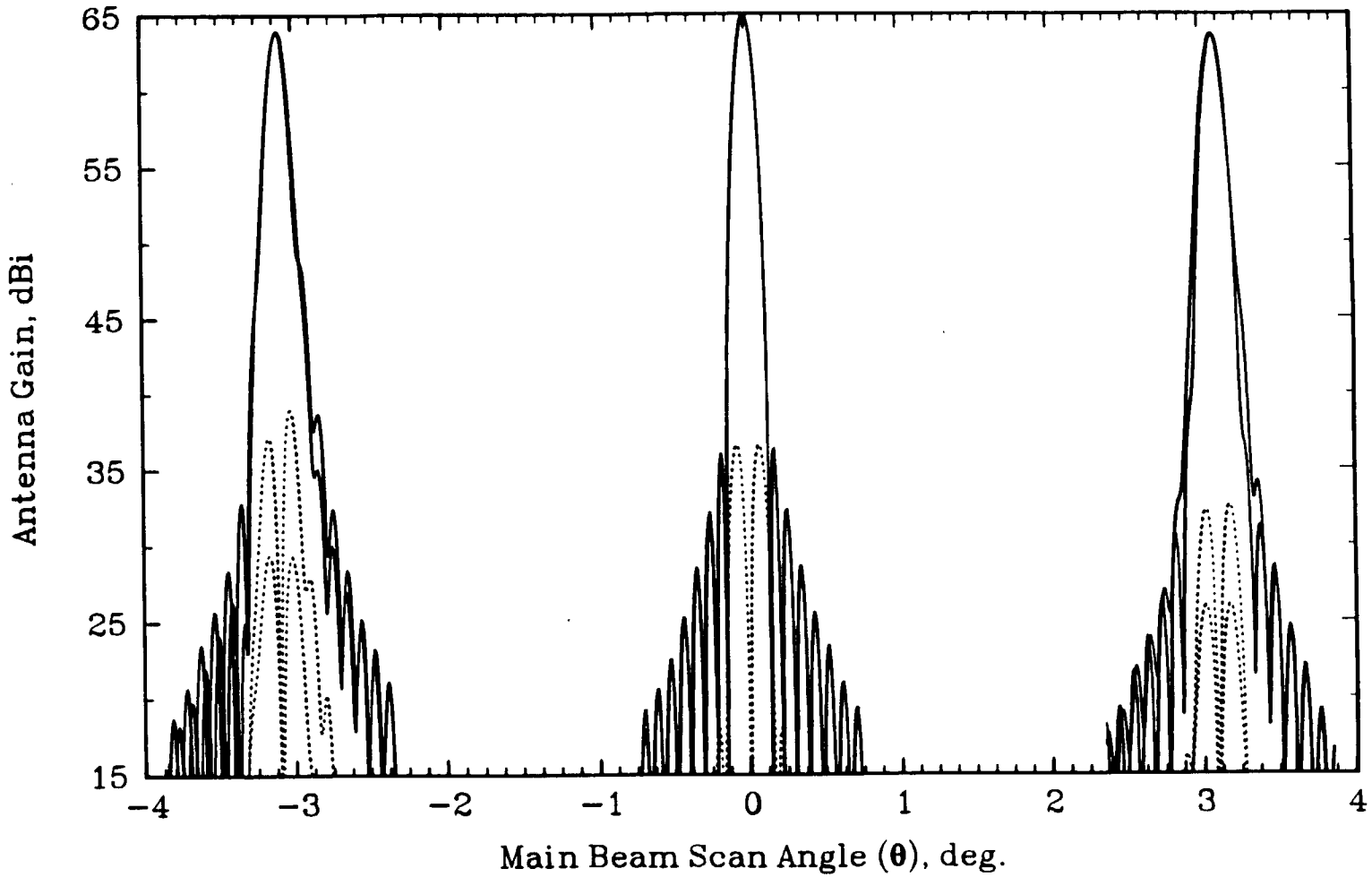

Figure 2-10. Principal plane patterns for θ=-2.5, 0, +2.5° and ϕ=45° scan directions at 24 GHz.

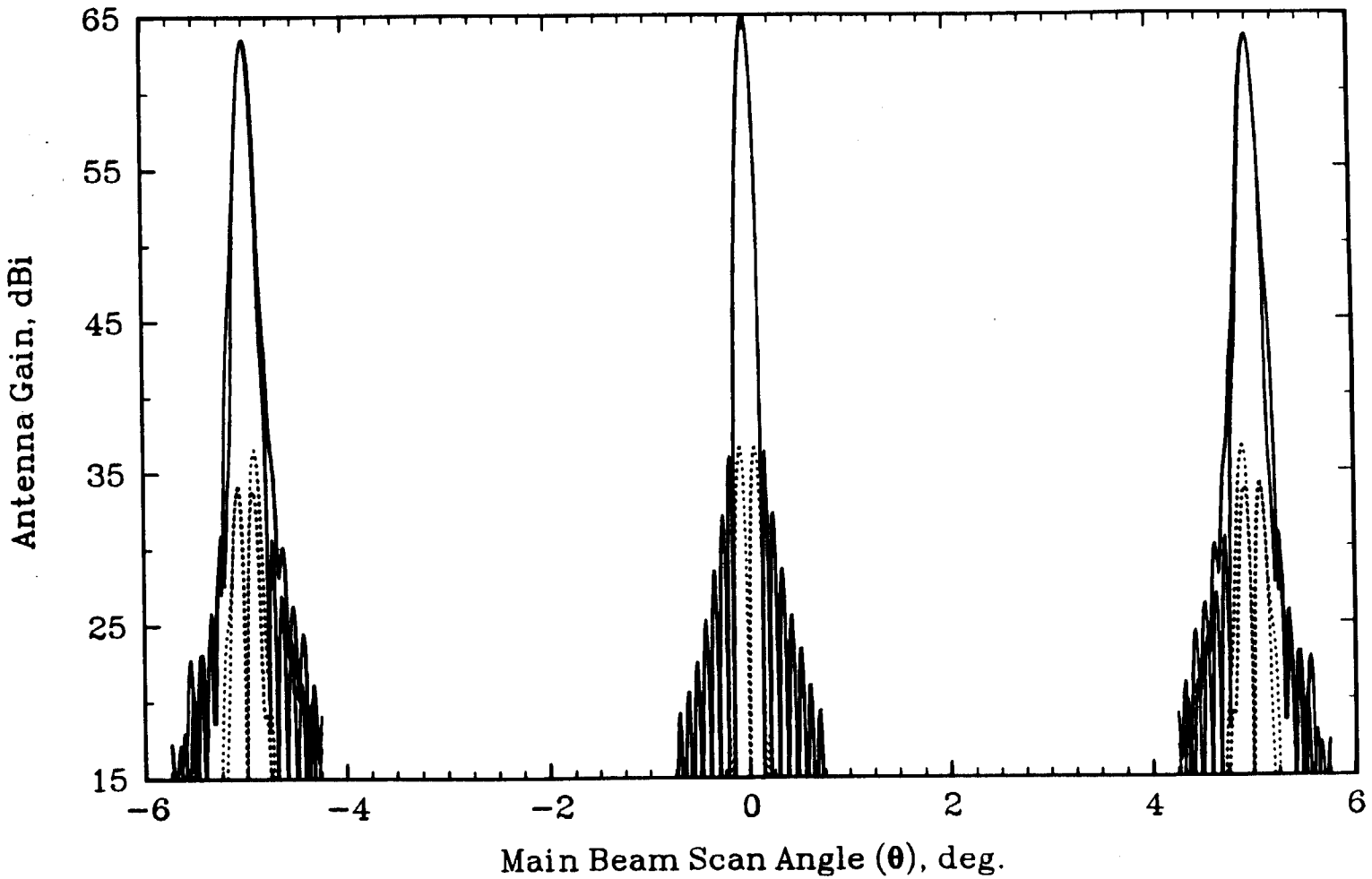

Figure 2-11. Principal plane patterns for θ=-2.5, 0, +2.5° and ϕ=90° scan directions at 24 GHz.

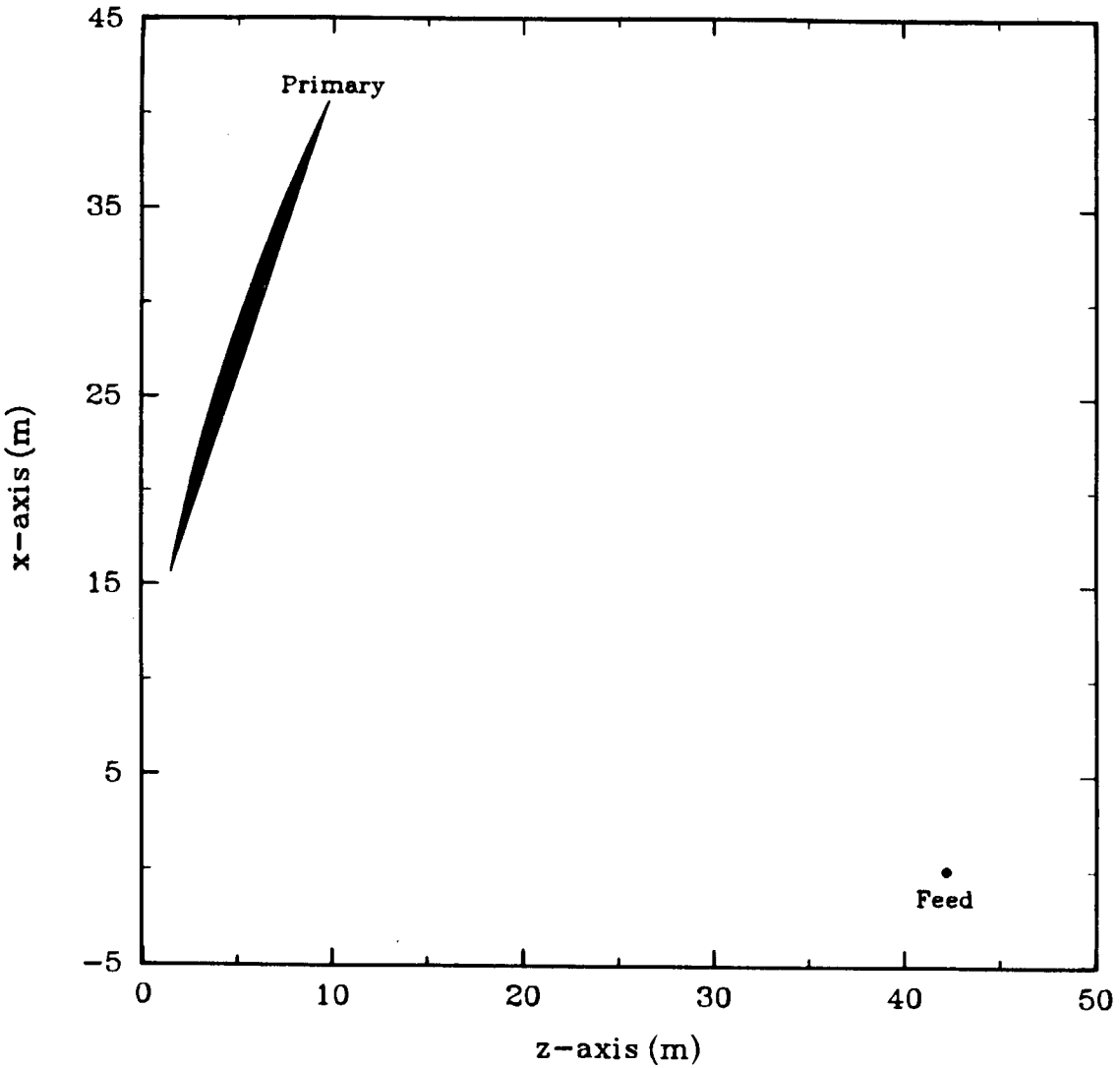

Figure 2-12. Geometry of the conventional offset prime-focus reflector used in comparisons; $F/D_p = 1.04$.

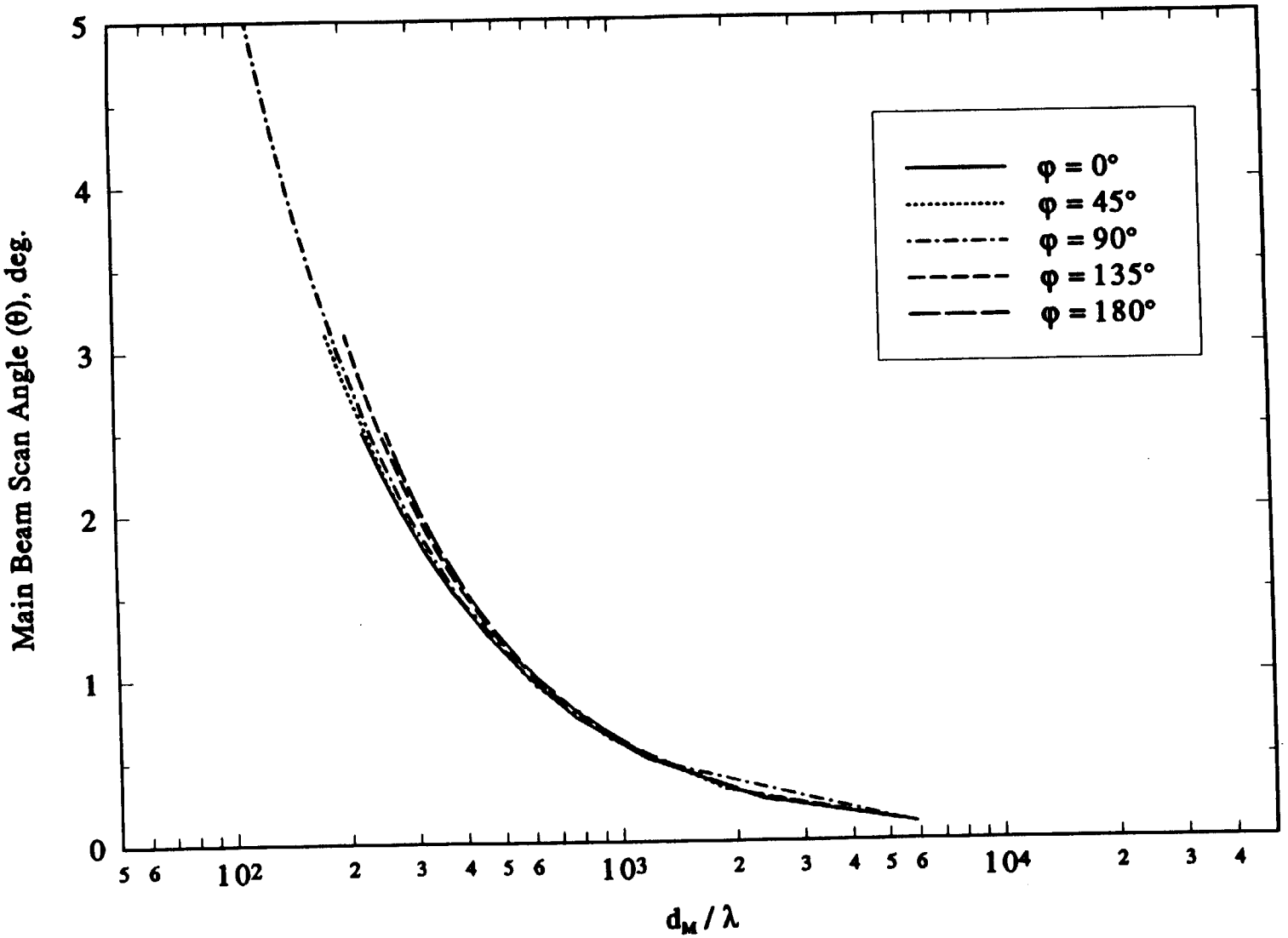

Figure 2-13. Beam scan range for 1-dB gain loss as a function of main reflector diameter of the conventional offset reflector of Fig. 2-12.

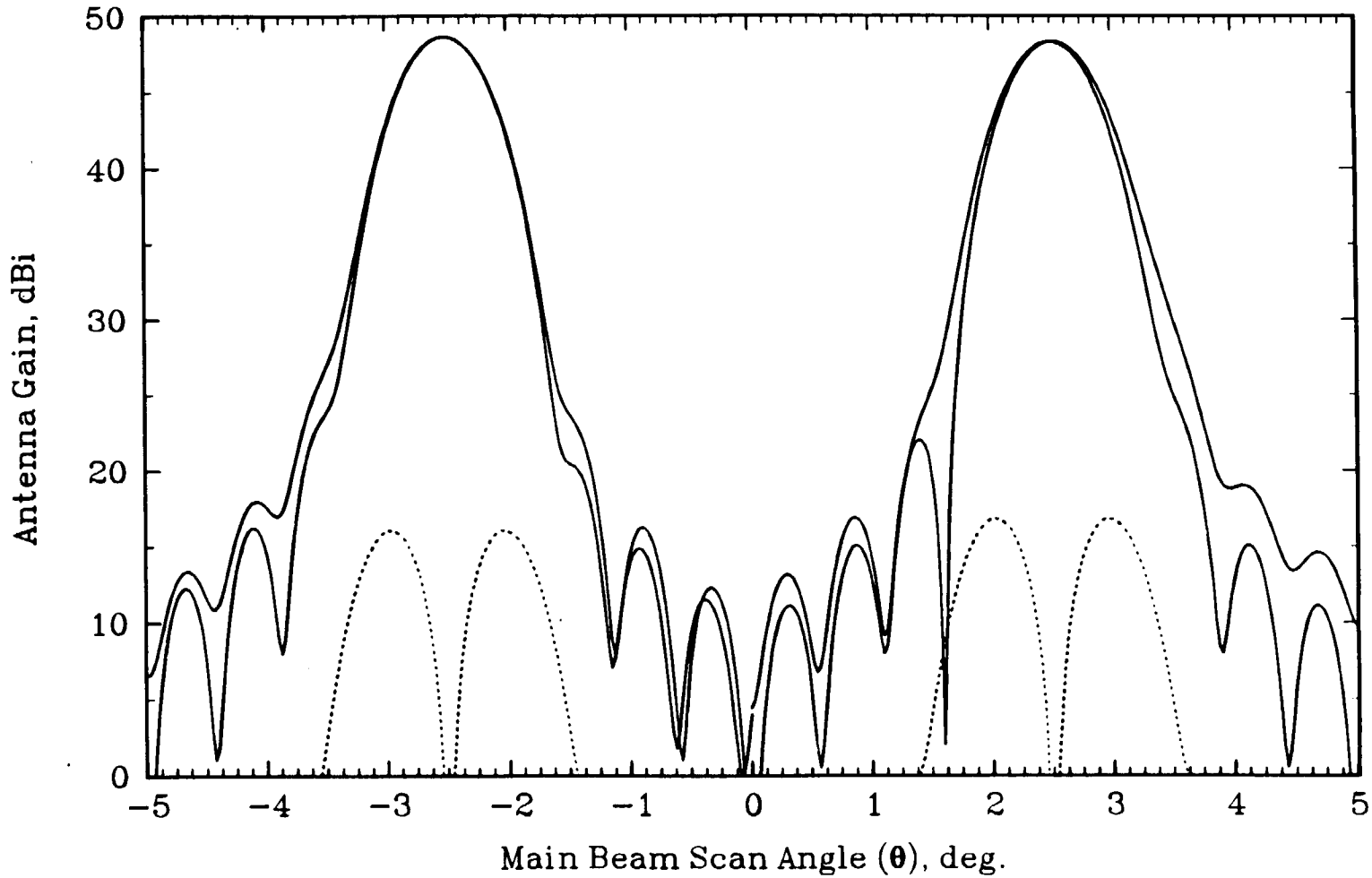

Figure 2-14. Principal plane and cross polarized (dashed) patterns for θ=-2.5 and +2.5°, ϕ=0° for the conventional offset reflector of Fig. 2-12.

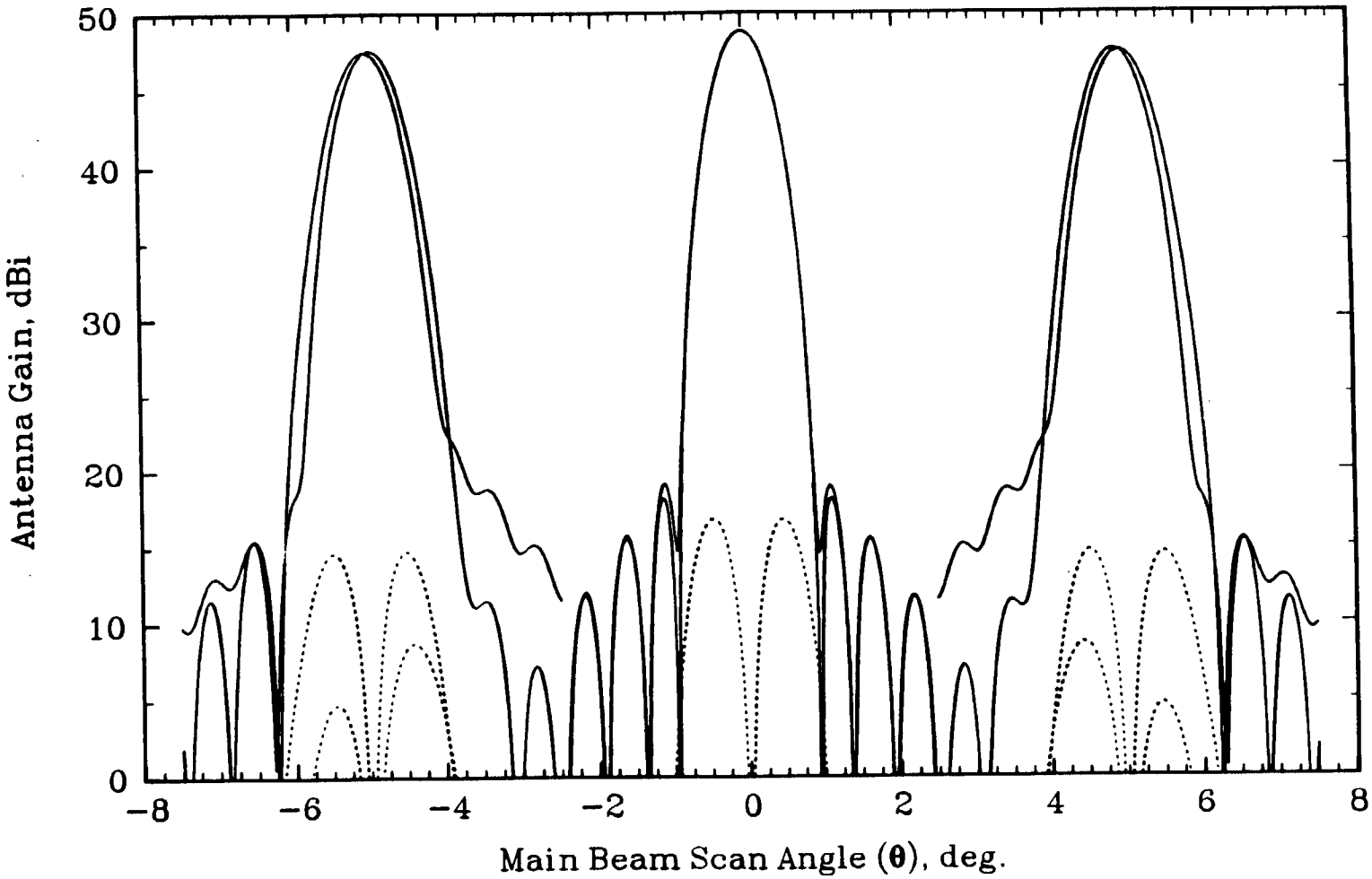

Figure 2-15. Principal plane and cross polarized (dashed) patterns for θ=-2.5, 0, +2.5°, ϕ=90° for the conventional offset reflector of Fig. 2-12.

Table 2-1

Summary of Scan Performance Computed Using Physical Optics at 18 GHz for the Type 2 Offset Cassegrain Tri-Reflector

Scan Direction		Mechanical Motions (deg)	Electromagnetic Performance						
θ	ϕ		Gain (dB)	Aperture Efficiency (%)	HPBW (deg)	$BW_{10\ dB}$ (deg)	Beam Efficiency (%)	Sidelobe Level (dB)	XPOL (dB)
0°	0°	α=0.0, β=0.0	62.44	77.13	0.15477	0.27051	95.86	-27.44	-28.37
2.5°	0°	α=7.32, β=0.0	61.39	60.06	0.17061	0.2957	96.78	-18.39	-31.61
3.1°	45°	α=6.97, β=-6.48	61.41	60.84	0.170	0.29531	96.756	-21.41	-30.10
5.0°	90°	α=3.14, β=-15.92	61.392	60.60	0.17164	0.29899	95.422	-19.39	-25.24
3.1°	135°	α=-6.08, β=-7.76	61.91	68.27	0.154	0.26124	93.052	-25.23	-24.906
2.5°	180°	α=-7.73, β=0.0	61.897	68.06	0.155	0.2687	91.95	-19.89	-25.383

Table 2-2

Summary of Scan Performance Computed Using Physical Optics at 24 GHz for the Type 2 Offset Cassegrain Tri-Reflector

Scan Direction		Mechanical Motions (deg)	Electromagnetic Performance						
θ	φ		Gain (dB)	Aperture Efficiency (%)	HPBW (deg)	$BW_{10\ dB}$ (deg)	Beam Efficiency (%)	Sidelobe Level (dB)	XPOL (dB)
0°	0°	α=0.0, β=0.0	64.963	77.56	0.12326	0.19676	96.00	-28.96	-28.35
2.5°	0°	α=7.32, β=0.0	63.675	57.655	0.128	0.232	96.90	-16.67	-31.67
3.1°	45°	α=6.97, β=-6.48	63.716	58.202	0.128	0.232	96.85	-13.716	-30.21
5.0°	90°	α=3.14, β=-15.92	63.594	56.59	0.129	0.235	95.65	-16.554	-25.01
3.1°	135°	α=-6.08, β=-7.76	63.99	61.99	0.122	0.219	94.73	-16.99	-24.88
2.5°	180°	α=-7.73, β=0.0	63.960	61.56	0.123	0.216	94.04	-16.96	-25.54

Table 2-3

Summary of Scan Performance Computed Using Physical Optics for a Conventional Offset Reflector with a 100 Wavelength Diameter Main Reflector

Scan Direction					Electromagnetic Performance						
		Mechanical Motions (m)									
θ	φ	Δx	Δy	Δz	Gain (dB)	Aperture Efficiency (%)	HPBW (deg)	$BW_{10\ dB}$ (deg)	Beam Efficiency (%)	Sidelobe Level (dB)	XPOL (dB)
0°	0°	0	0	0	48.844	77.64	0.70087	1.28653	96.406	-29.14	-32.057
2.5°	0°	-1.62	3.21×10^{-4}	-1.28	48.38	69.77	0.79337	1.3449	95.06	-23.38	-31.57
5.0°	90°	0.12	-4.13	-0.164	47.627	58.66	0.814	1.343	91.79	-24.63	-32.74
2.5°	180°	1.68	1.56×10^{-3}	1.20	48.681	74.78	0.807	1.269	95.59	-18.68	-32.65

Chapter 3

DESIGN AND PERFORMANCE OF THE TYPE 1 REFLECTOR ANTENNA

The Type 1 reflector antenna system concept was first proposed by Peter Foldes as his Type 6 antenna [1] and was based on geometrical optics principles. Foldes speculated that one half-degree of scan in any direction could be obtained by rotation of the subreflector of the Type 1 dual reflector system. In this section we describe this configuration and its performance with a parabolic main reflector and a hyperbolic subreflector. The three-dimensional antenna synthesis and subreflector positioning procedure is described. Electromagnetics analysis results including gain, sidelobe level, cross-polarization level, and beam efficiency are presented for the antenna system over the scan range. Finally, the results of a preliminary study of the effects of subreflector and feed positioning errors are given.

3.1. The Type 1 Concept

The Type 1 antenna system is an offset Cassegrain dual reflector antenna. Scanning is achieved by only subreflector motion to minimize the moving mass of the system. The combination of a dual-offset design and the small subreflector also reduces aperture blockage and significantly increases the electrical focal length for a given mechanical size. The Type 1 antenna system is designed for scanning in a $\theta \leq 0.5^{\circ}$ cone at any ϕ angle from 0° to 360°. The scan angle θ is defined to be the declination angle from the +z-axis and the scan angle ϕ is defined to be the azimuth angle in the xy-plane from the +x-axis towards the +y-axis.

Feed point and subreflector locations for the Type 1 antenna system were chosen in accordance with the Mizugutch condition for an axi-symmetric equivalent paraboloid. This condition allows the illumination of the main reflector to be tapered to illuminate the main reflector with a power distribution which is corrected for spherical spreading loss; also, the feed-to-aperture mapping closely approximates the aperture distribution of an axi-symmetric reflector. This allows offset dual reflector antenna systems synthesized with the Mizugutch condition to have nearly the same (low) degree of cross-polarization as an axisymmetric reflector. Three dimensional views of the antenna system are shown in Figure 3.1-1 (a-d). The system discussed here was chosen to fit the proposed, which is a 42.52% scale model of the 25-m goal antenna NASA Langley Antenna and Microwave Research Branch/Space Structures test article.

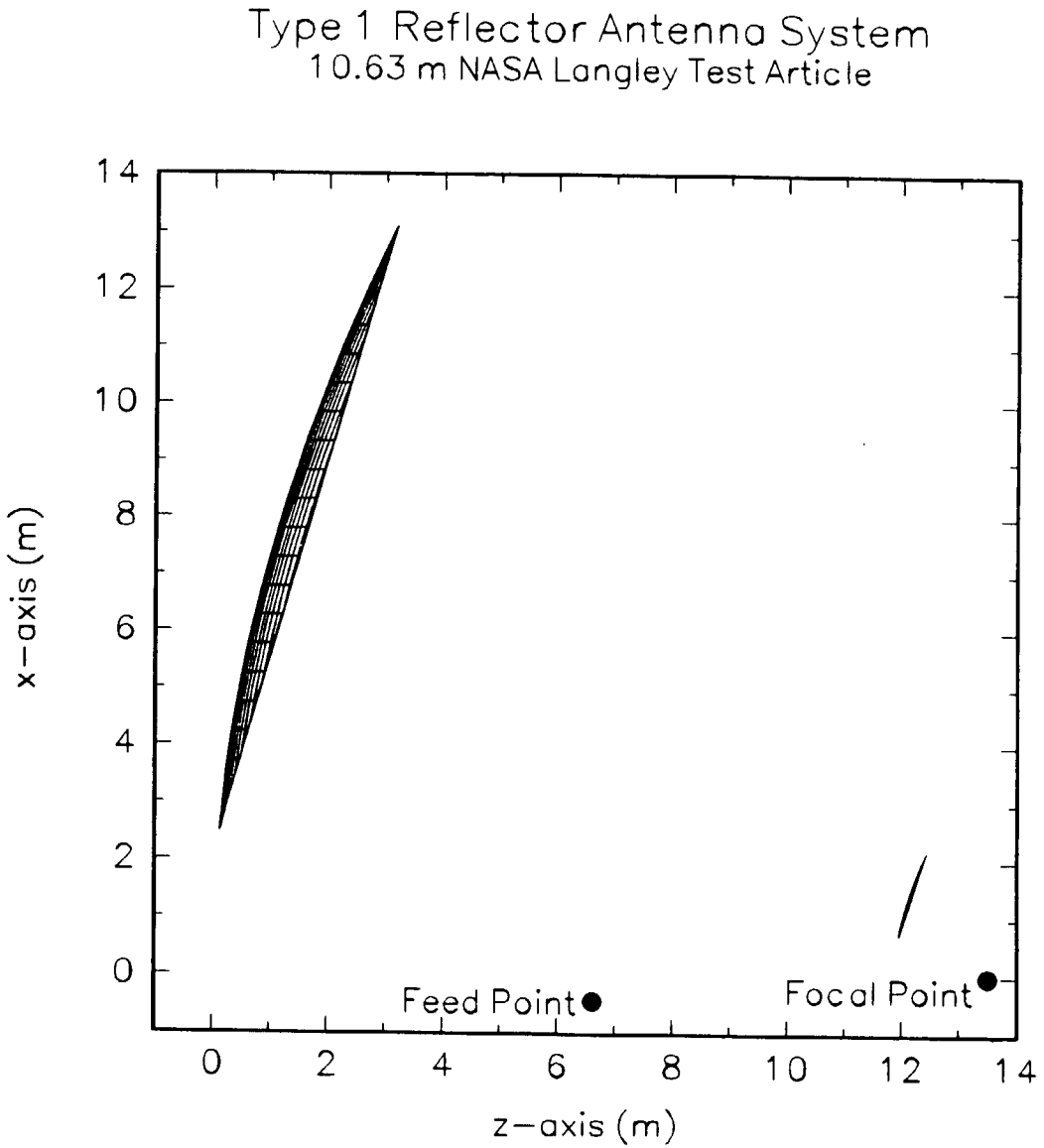

Figure 3.1-1 (a). Type 1 reflector antenna system (side view).

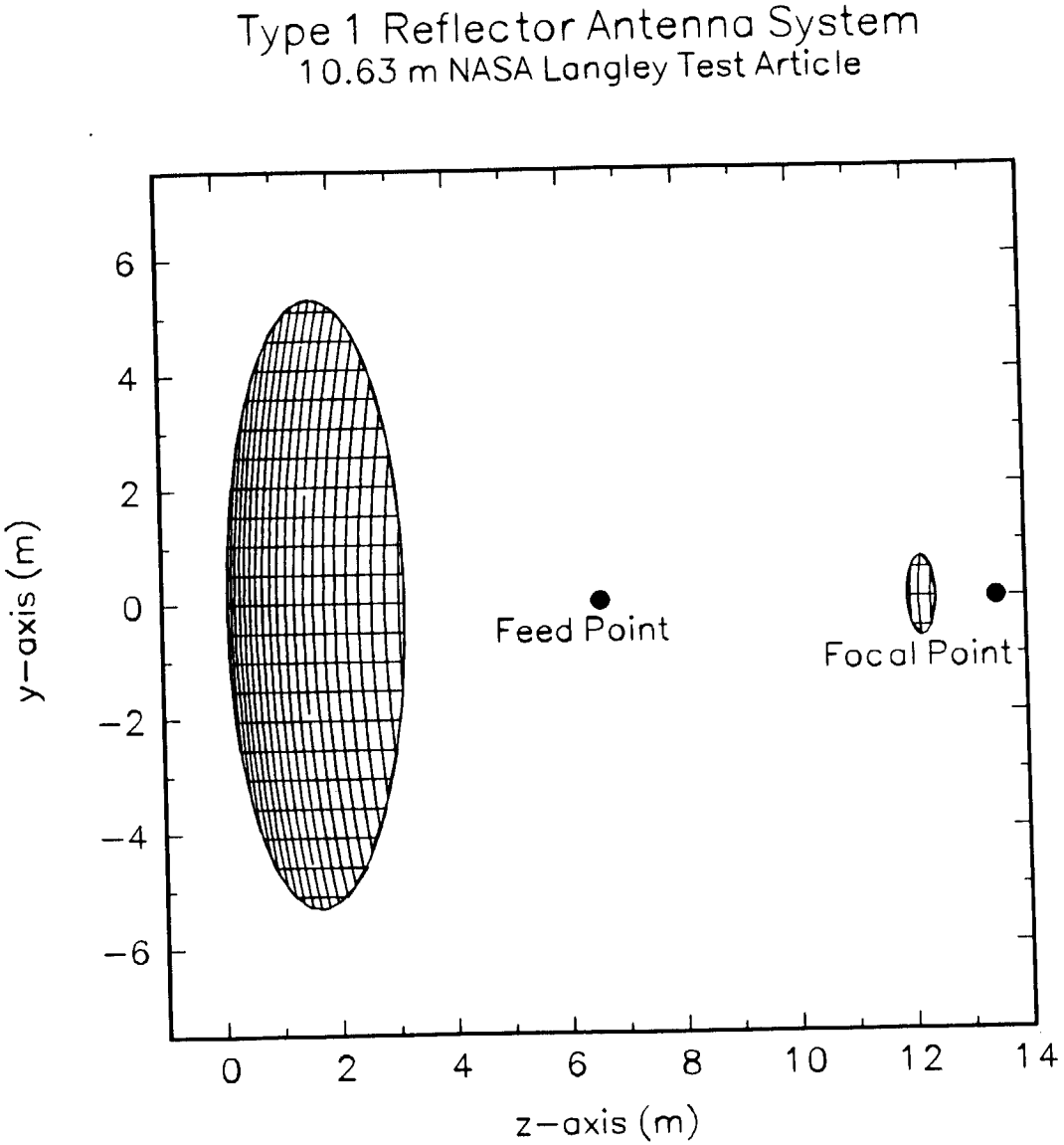

Figure 3.1-1 (b). Type 1 reflector antenna system (top view).

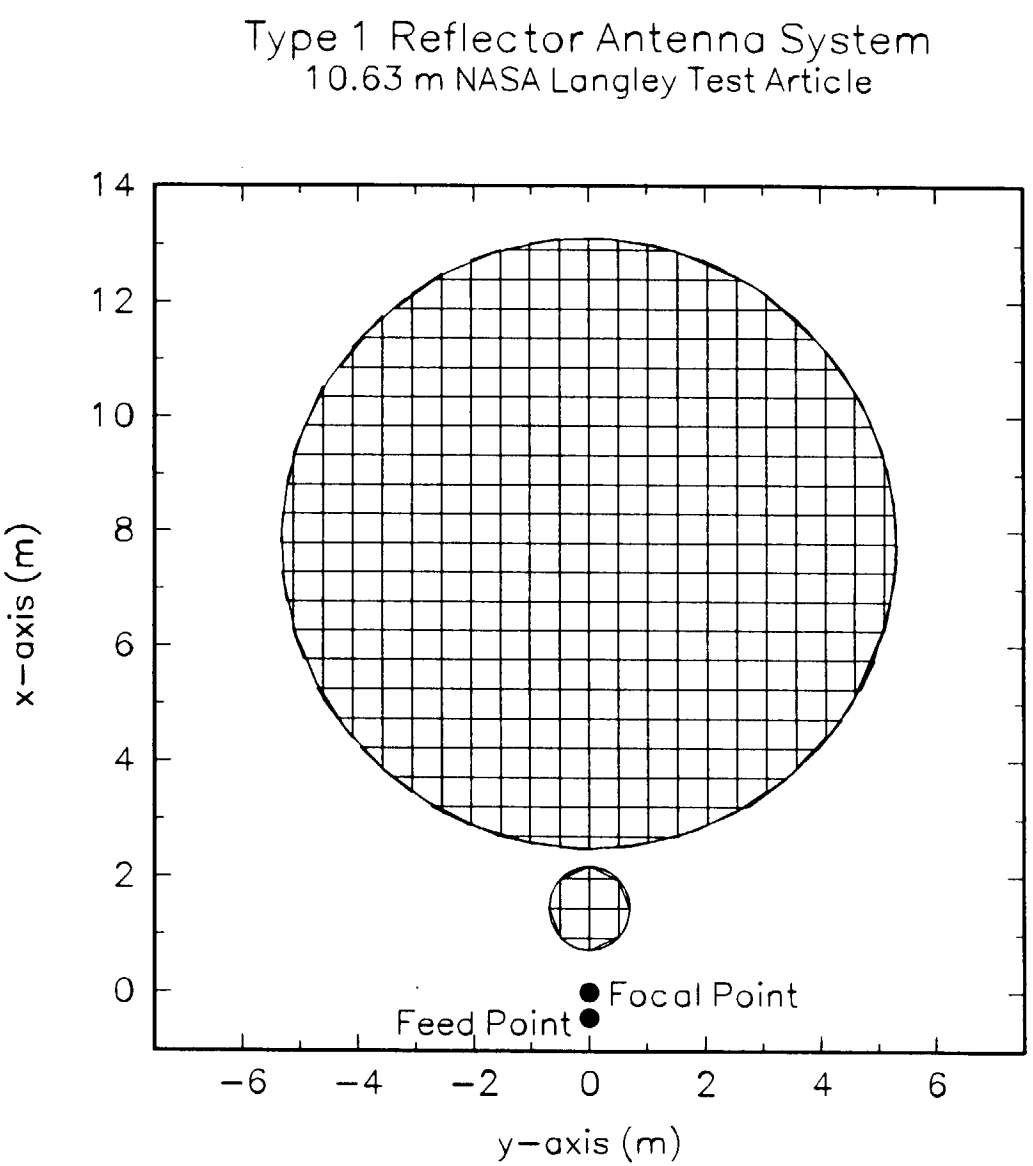

Figure 3.1-1 (c). Type 1 reflector antenna system (front view).

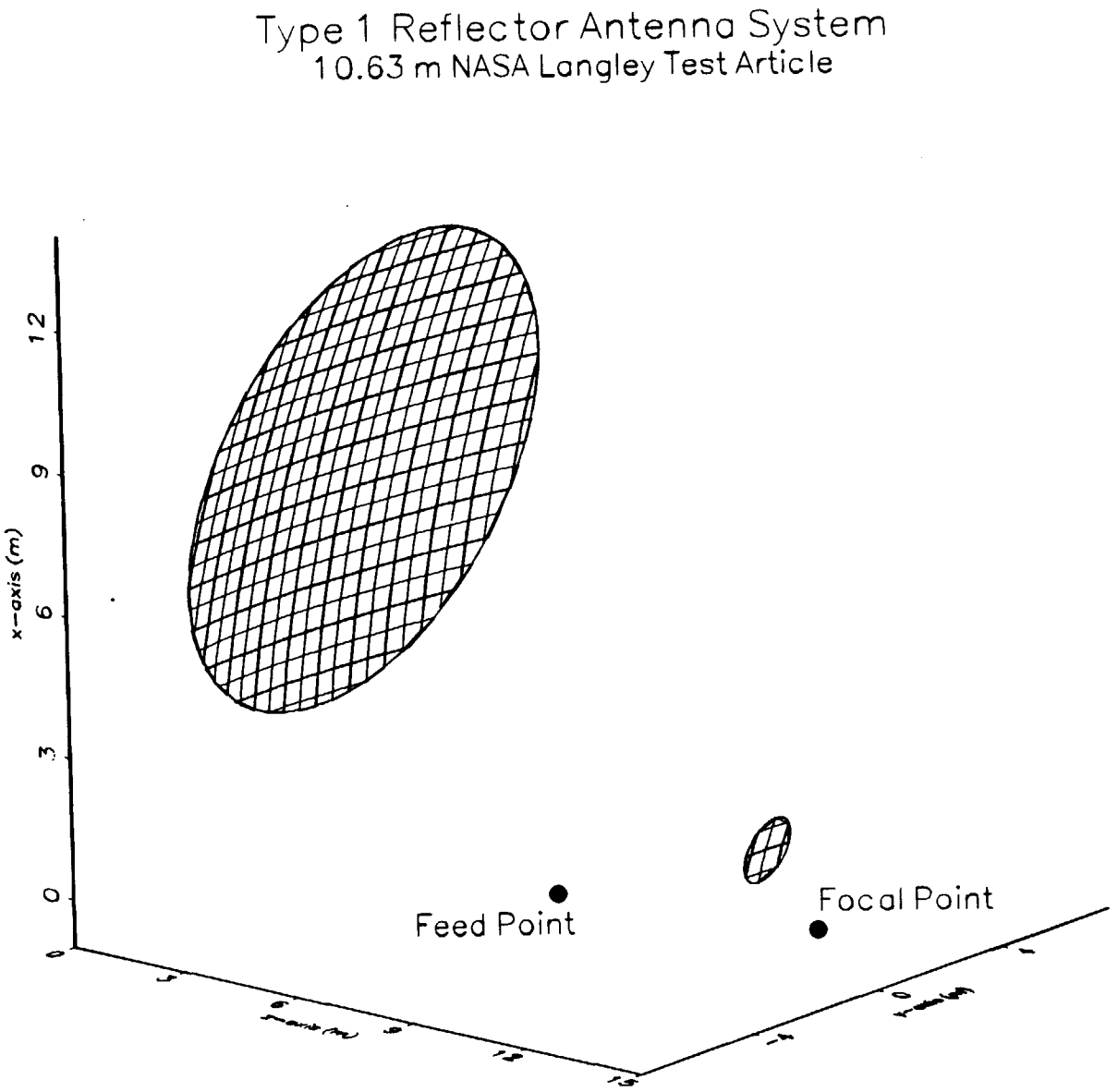

Figure 3.1-1 (d). Type 1 reflector antenna system.

3.2. Dual Reflector Antenna Synthesis - 3 Dimensional (DRAS-3D)

The three dimensional synthesis of the Type 1 reflector antenna system is performed using the code DRAS-3D. This program uses geometric optics raytracing to determine the optimal position for an unscanned subreflector in the scanned system. The unscanned subreflector is defined as an m by n grid of points on the hyperboloidal surface and the normals at those points. Although the subreflector is known to be hyperboloidal, the unscanned subreflector surface is determined by receive mode raytracing in order to develop a uniform grid in the antenna aperture plane.

In DRAS-3D, the subreflector is allowed to translate in three dimensions and rotate about P_r in two directions: α, a tilt from the +z-axis towards the +x-axis, and β, a tilt from the +z-axis towards the +y-axis. The point P_r is located on the subreflector surface and moves with the surface when the subreflector is translated. For the unscanned subreflector P_r is the point where a ray from the feed that ultimately traces to the center of the projected aperture reflects from the subreflector. This allows the program to select the optimal location and orientation for the subreflector using the transmitted ray deviation error function described by

$$\varepsilon = \sum_{i=1}^{m} \sum_{j=1}^{n} \left| \hat{t}_{ij} \times \hat{s} \right|^2 \qquad (3.1\text{-}1)$$

Where $\hat{t}_{ij}$ is a unit vector in the direction of the i,jth transmitted ray and $\hat{s}$ is a unit vector in the desired direction of scan. This error function gives the squared divergence of the transmitted rays from the desired scan direction. Although this error function is proportional to the root mean square path length error in the system, this error definition approaches zero more steeply and so is more suitable for use in optimization routines.

This error function was found to perform much better than the previously used Kitsuregawa error method [2], which attempts to fit the unscanned subreflector to a correcting subreflector for each direction of scan. While the Kitsuregawa fitting method provides a more even aperture illumination, the aperture phase error optimization method offers superior scanned antenna performance by reducing phase errors at the expense of illumination efficiency. Over a small scan region, such as that expected of the Type 1 system, the loss in efficiency due to uneven illumination is smaller than the loss due to the phase errors created by the Kitsuregawa method. After the optimal

position of the subreflector in the scanned system is determined, the GRASP7 input file is automatically written by DRAS-3D.

The predicted translations and rotations for the subreflector are shown as functions of scan angle in Figures 3.2-1 through 3.2-5. These figures show subreflector positioning information for scanning over ϕ angles from 0° to 180°. Since the system is symmetric about the x-axis, the required positioning for ϕ angles from 180° to 360° is the same in for x and z translation and α rotation but the negative of the y translation and β rotation. As shown, the required translation ranges for the subreflector are all ~ 0.5 meters or less. The required rotational capability is $< 15°$ for both the α and the β rotation angles.

3.3. Electromagnetic Analysis Results

Electromagnetic analysis of the Type 1 reflector antenna system was performed at 18 GHz using the TICRA GRASP7 reflector numerical analysis package. Due to time constraints, GO/GTD analysis was used at the subreflector with PO analysis on the main reflector. Subsequent trials performed using PO analysis at both reflecting surfaces show the loss of accuracy due to subreflector GO/GTD analysis to be slight for both co- and cross-polarized far-field antenna pattern calculations. The antenna system used for these analyses consisted of the 10.63 meter projected aperture diameter NASA Langley AMRB/Space Structures test article main reflector surface with a hyperbolic subreflector which was chosen to create an axisymmetric equivalent paraboloid. This system was fed by a feed fixed at the unscanned feed point and pointed correctly for the unscanned case. The feed taper was chosen to be -15 dB at the edge of the subreflector when the subreflector was in its unscanned position. The output of the analyses was in the form of co- and cross-polarized field components taken in an equally spaced u-v grid. The beam efficiency was then calculated using the TICRA UVPROC package with the main beam solid angle taken to be 2.5 times the unscanned half-power beamwidth for all beam efficiency calculations.

Figure 3.3-1 shows the main beam peak gain of the antenna system as a function of scan angle for the Type 1 system. The scan range of $\sim 0.625°$, calculated using a 1 dB gain loss criteria, is slightly greater than the designed 0.5° scan region. The gain loss of the system as scan angle increases is largely attributable to spillover losses as shown in Figure 3.3-2. The dominate loss of gain due to spillover effects allows the use of the Type 1 antenna system design synthesized for the 10.63 meter test article to be used at frequencies of >36 GHz without reducing the scan range below the designed 0.5° cone.

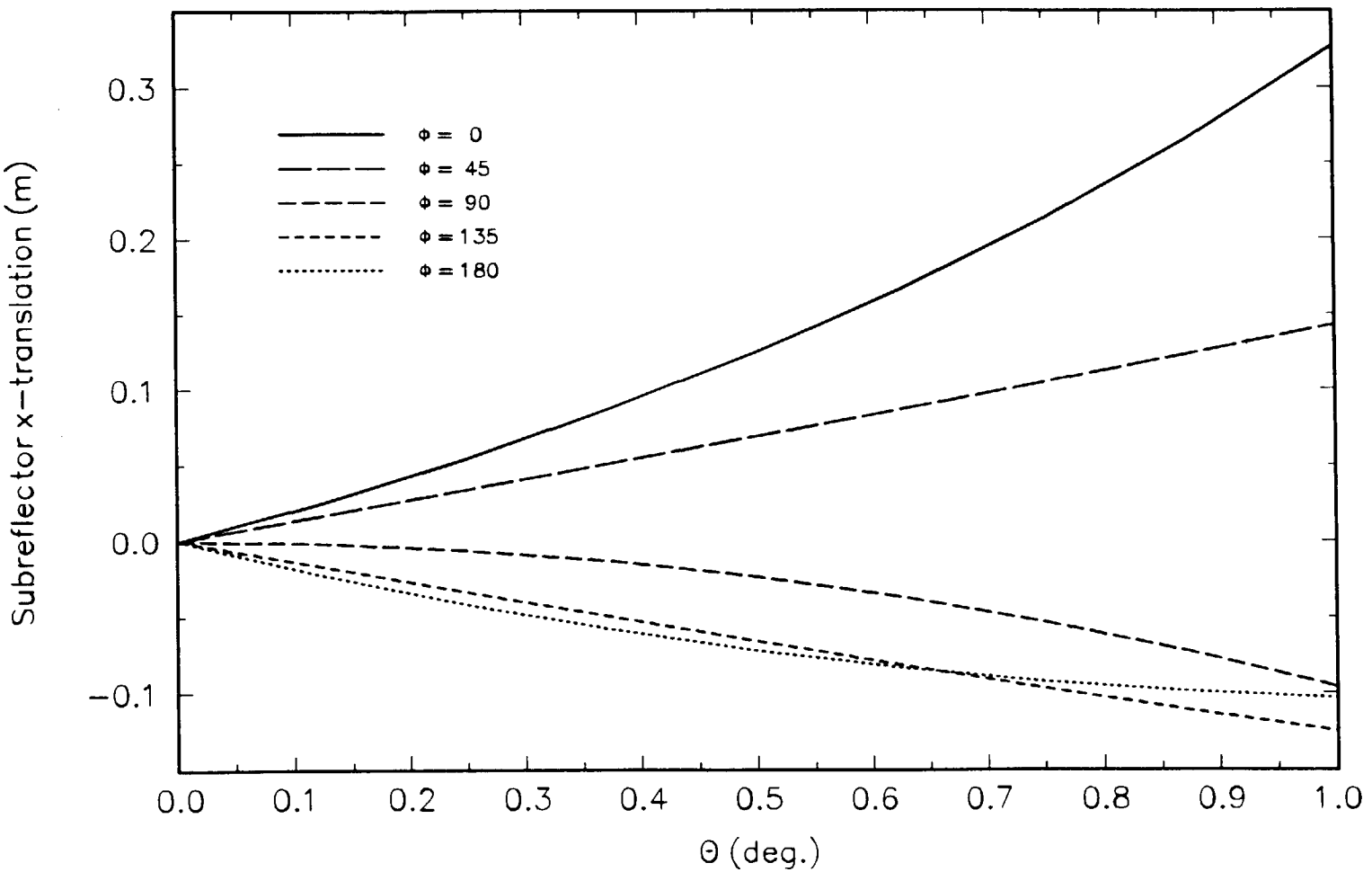

Figure 3.2-1. Type 1 reflector antenna system. Subreflector translation in the x-direction versus elevation scan angle.

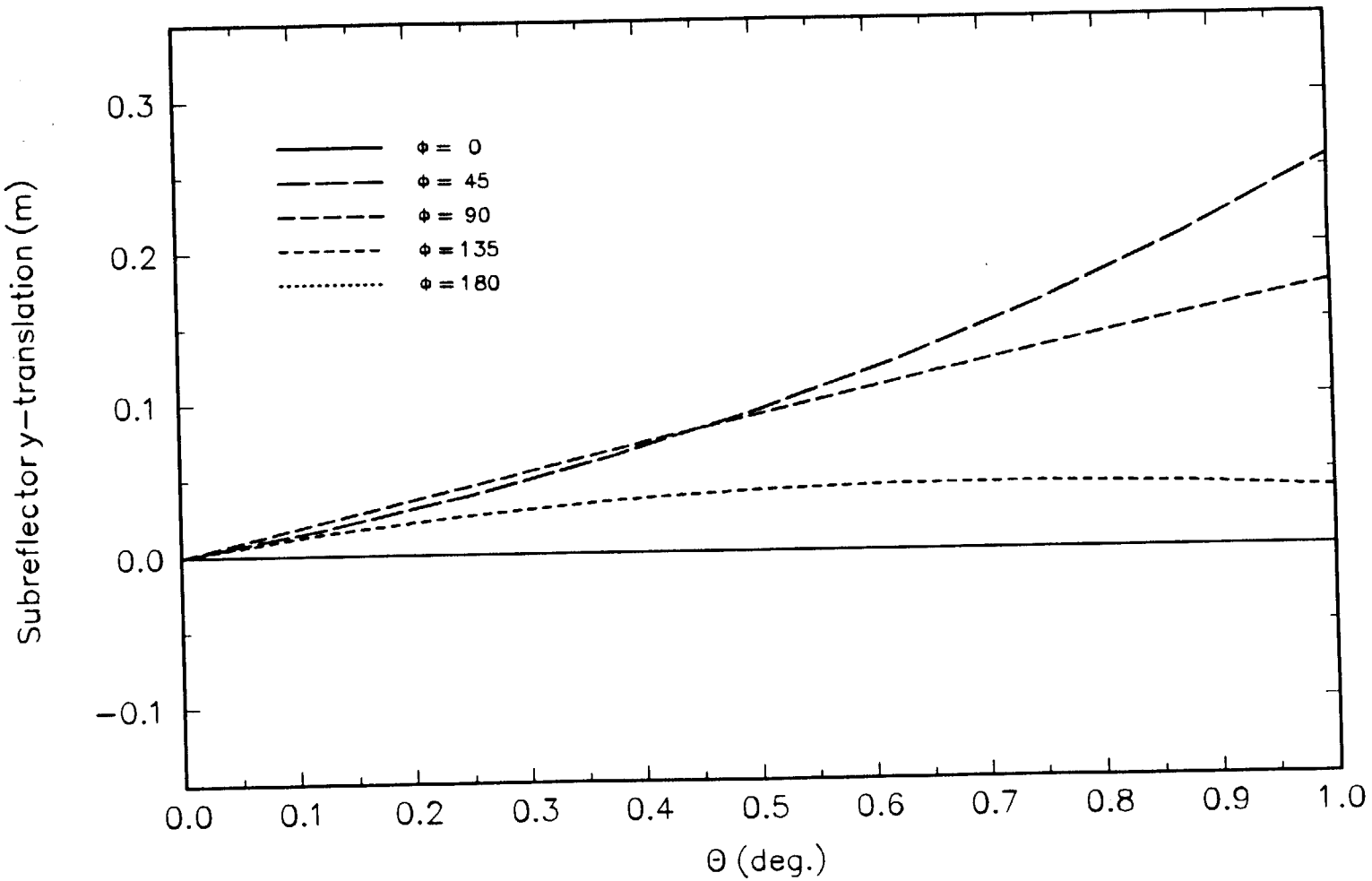

Figure 3.2-2. Type 1 reflector antenna system. Subreflector translation in the y-direction versus elevation scan angle.

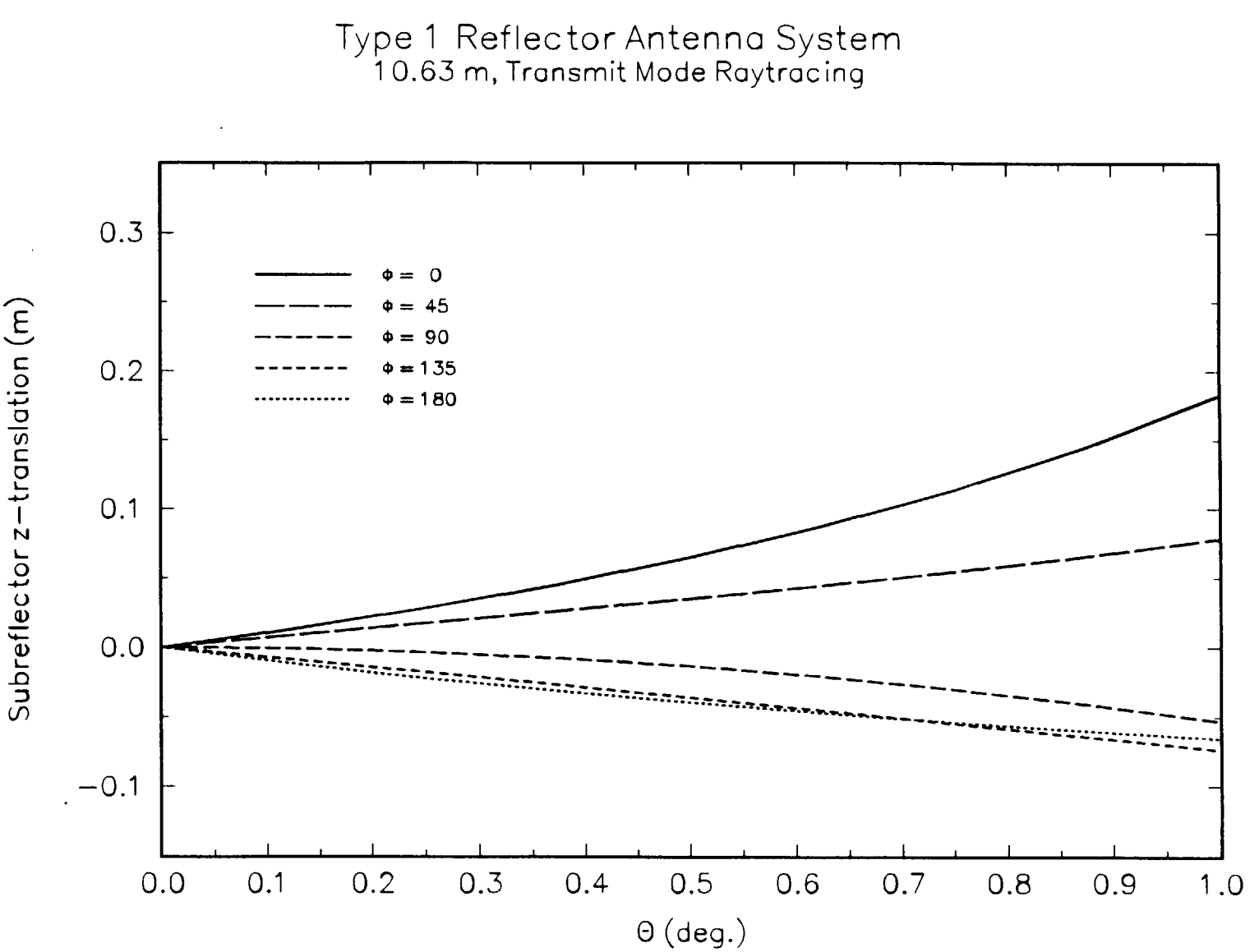

Figure 3.2-3. Type 1 reflector antenna system. Subreflector translation in the z-direction versus elevation scan angle.

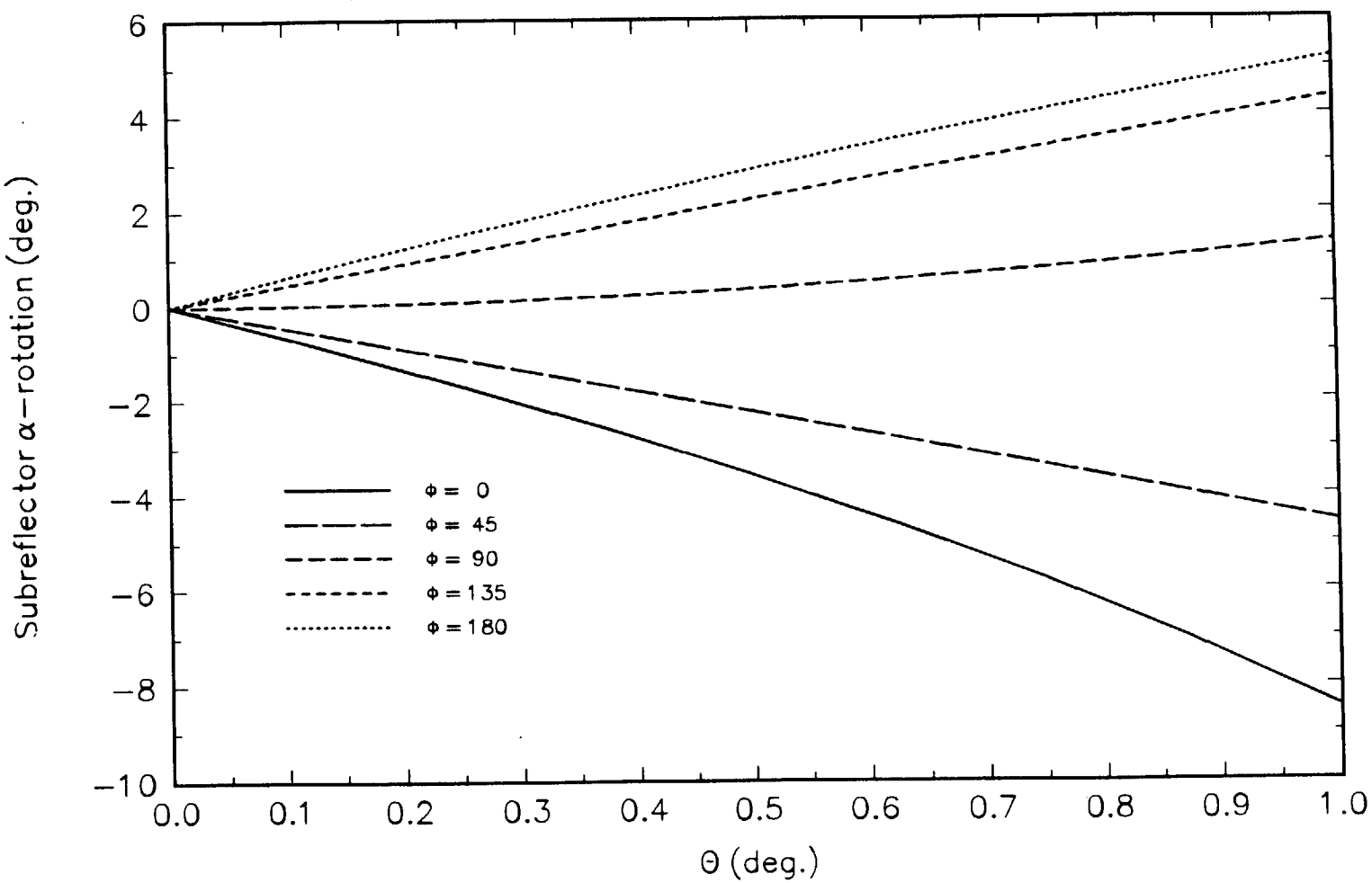

Figure 3.2-4. Type 1 reflector antenna system. Subreflector α rotation versus elevation scan angle.

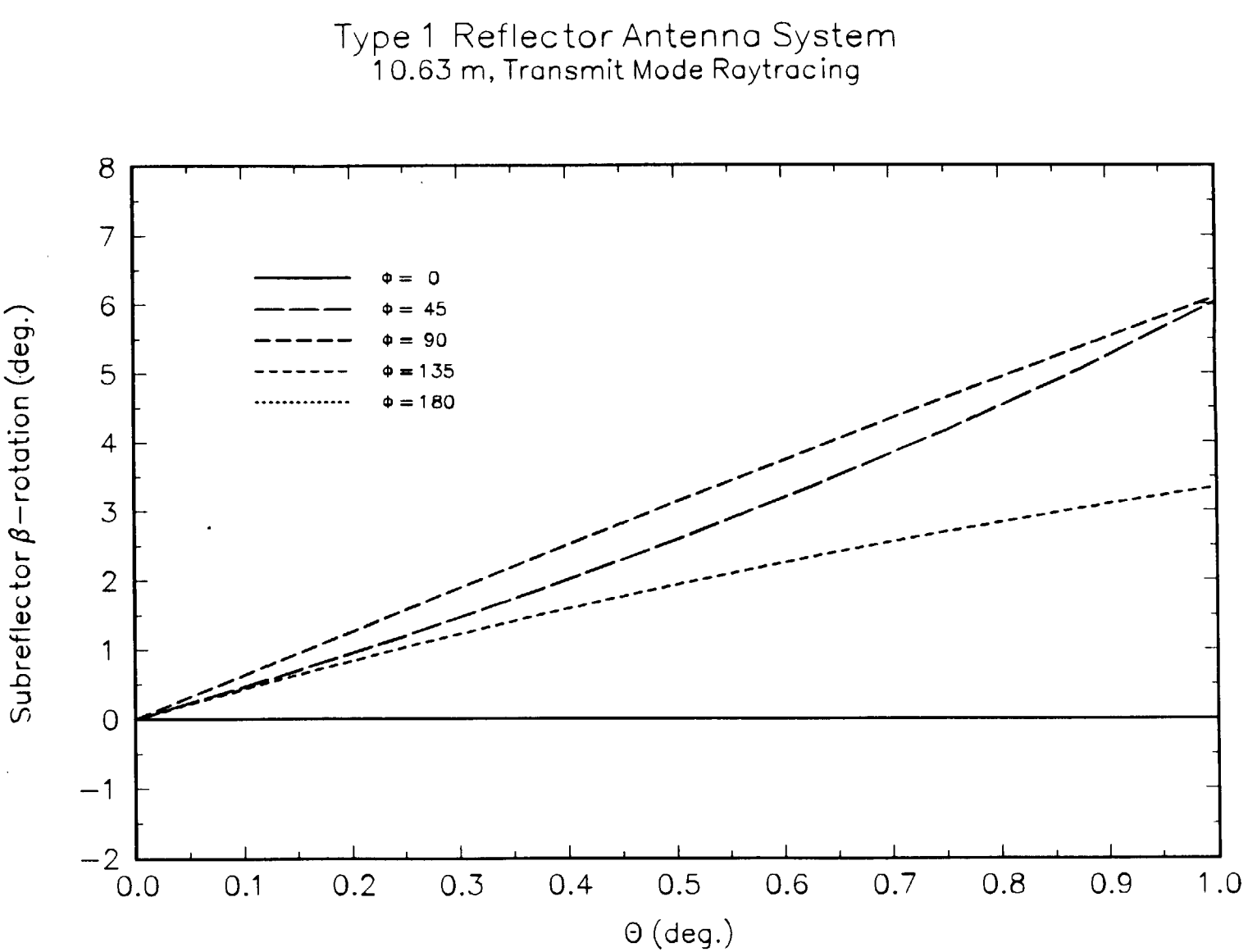

Figure 3.2-5. Type 1 reflector antenna system. Subreflector β rotation versus elevation scan angle.

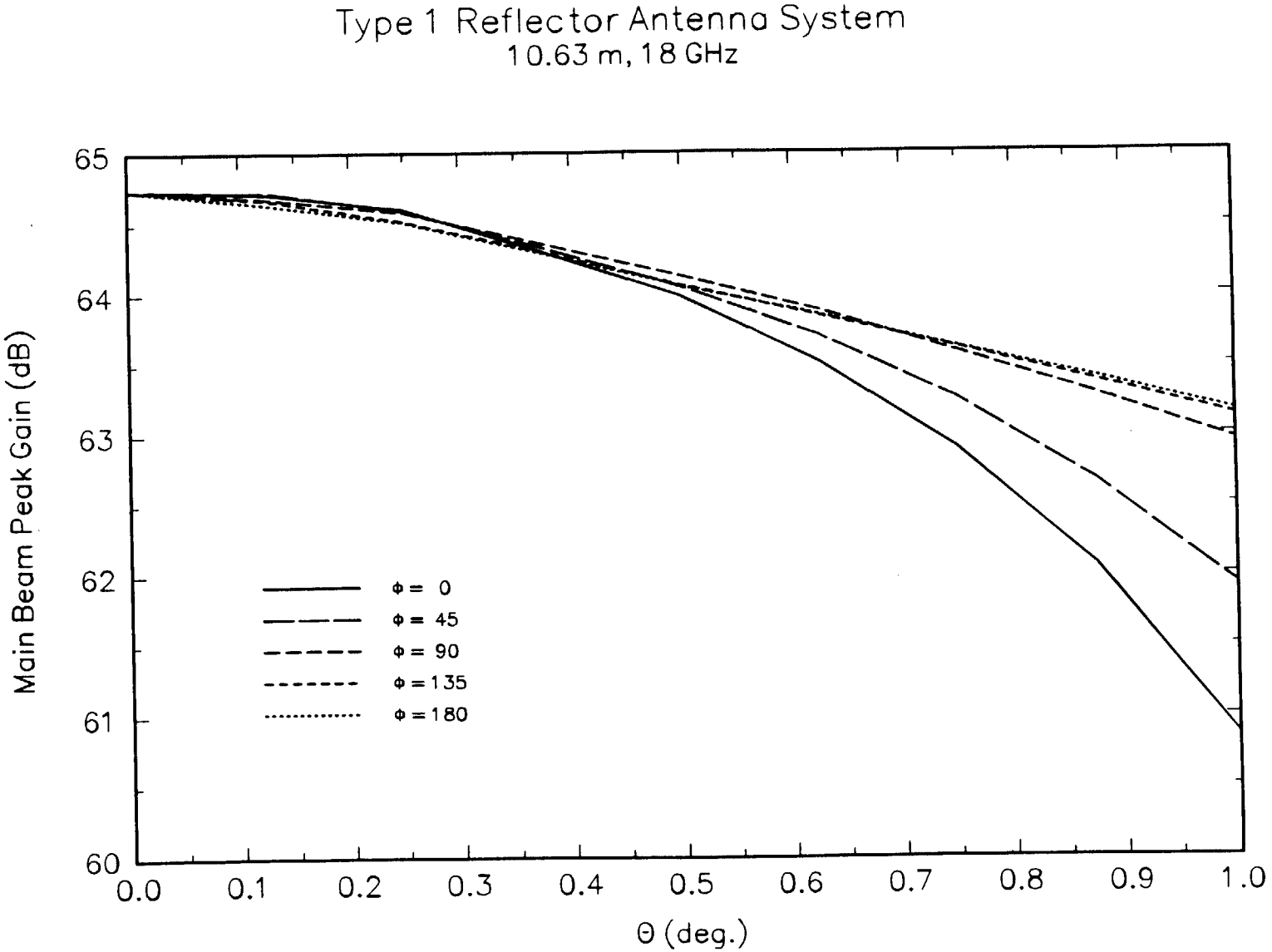

Figure 3.3-1. Type 1 reflector antenna system. Main beam gain versus scan angle.

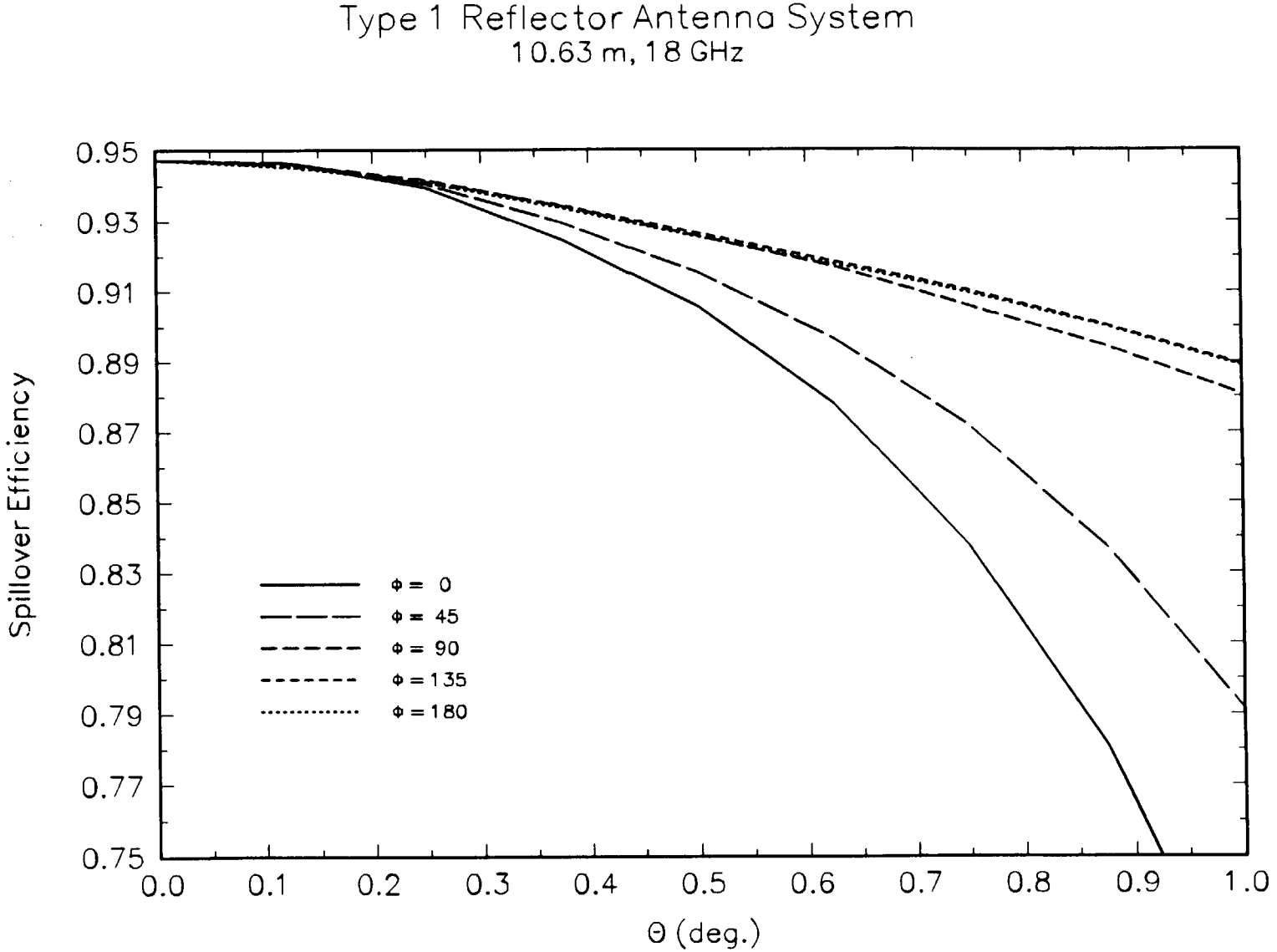

Figure 3.3-2. Type 1 reflector antenna system. Spillover efficiency versus scan angle.

The relatively low sidelobe level of the system at small scan angles, shown in Figure 3.3-3, is also a result of the secondary effects of phase error in gain loss in an antenna system synthesized with this method. The system sidelobe level will increase at higher operating frequencies as phase effects increase. The cross-polarization level of the antenna system is shown in Figure 3.3-4. The use of the Mizugutch condition in the antenna synthesis procedure reduced the cross-polarization level in trial cases by over 30 dB. Although cross-polarization level to increases over the scan range, the cross-polarization level at the scan limit is less than -22 dB. A slight amount of polarization rotation at scan angles out of the plane of symmetry degrades cross-polarization performance at θ=1.0° to approximately -37 dB. Beamwidths at the -3 and -10 dB levels are shown for the Type 1 antenna system in Figures 3.3-5 and 3.3-6. The Type 1 antenna system beam efficiency is shown as a function of scan angle in Figure 3.3-7. Beam efficiency remains above $\sim 90\%$ over the designed 0.5° scan region. These results are tabulated in Table 3.3-1.

Figures 3.3-8 through 3.3-14 show uv-plane contour plot patterns for the Type 1 antenna system at 18 GHz. The plots are centered at the indicated scan directions and show a rectangular area approximately 1° square. Both the co- and cross-polarization plots are normalized by the co-polarization antenna gain at that scan angle.

3.4. Error Sensitivity

The sensitivity of the Type 1 antenna system to positioning error has been estimated by performing electromagnetics analyses of the system at boresight and a limiting scan position with $\pm 0.5^{\circ}\lambda$ translational errors and $\pm 0.1^{\circ}$ rotational errors imposed independently on the subreflector and $\pm 0.5\lambda$ translational errors imposed on the feed. This analysis was performed in the same manner as the system characteriztion shown in the previous section. As shown in Table 1.2-4, the Type 1 antenna system is essentially unaffected by translational errors of 0.5λ at either the feed or subreflector. Rotational errors in the positioning of the subreflector cause a main beam pointing error of 25% of the subreflector error.

3.5. References

[1] P. Foldes, "Some Characteristics of Six Alternative Multireflector Radiometers for 6-31 GHz GEO Operation," Foldes, Inc., May 9, 1990.

[2] T. Kitsuregawa, Advanced Technology in Satellite Communication Antennas, Artech House: Boston, MA, 1990, "Section 2.6, Steerable Beam Antennas," pp. 177-188.

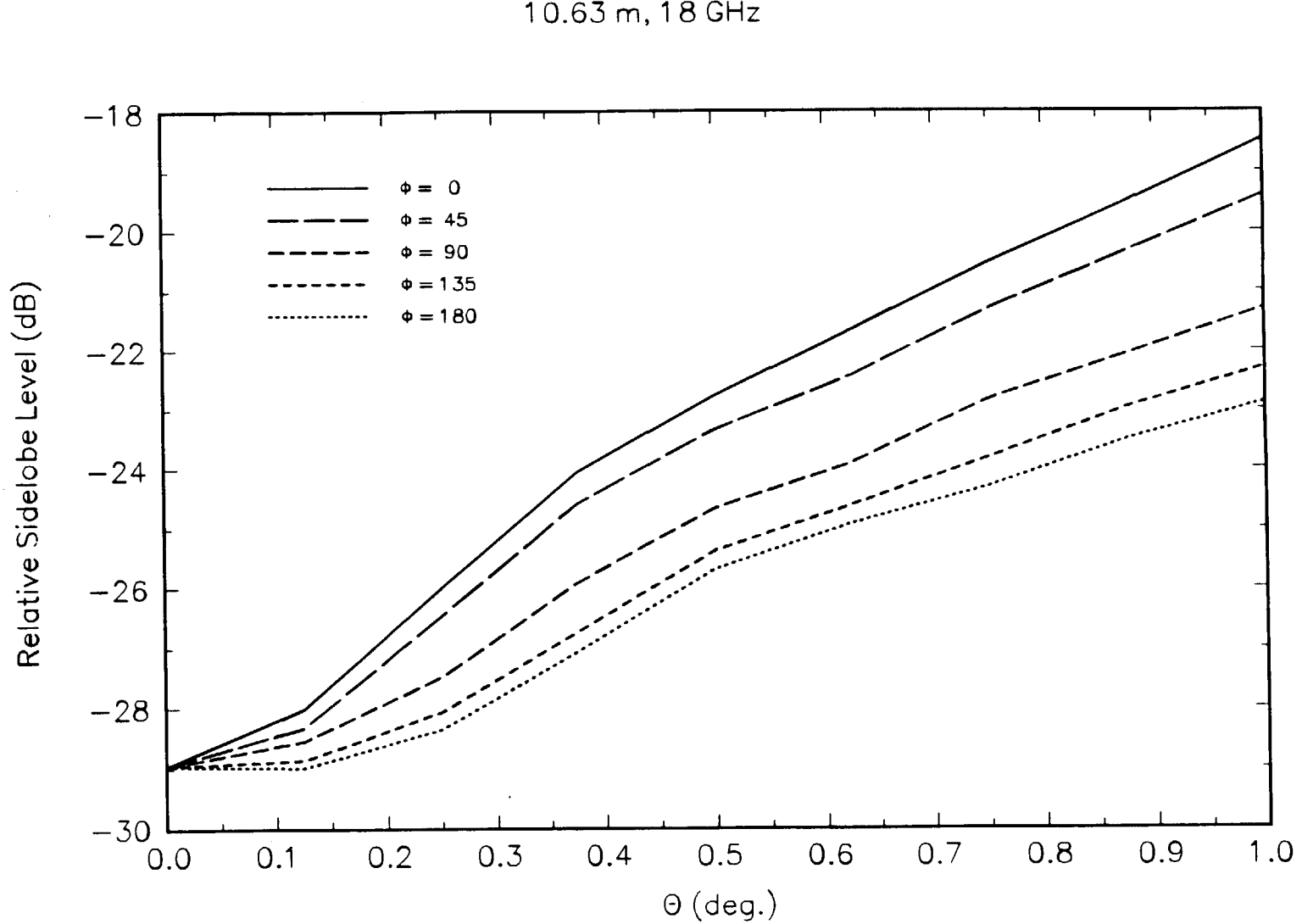

Figure 3.3-3. Type 1 reflector antenna system. Relative sidelobe level versus scan angle.

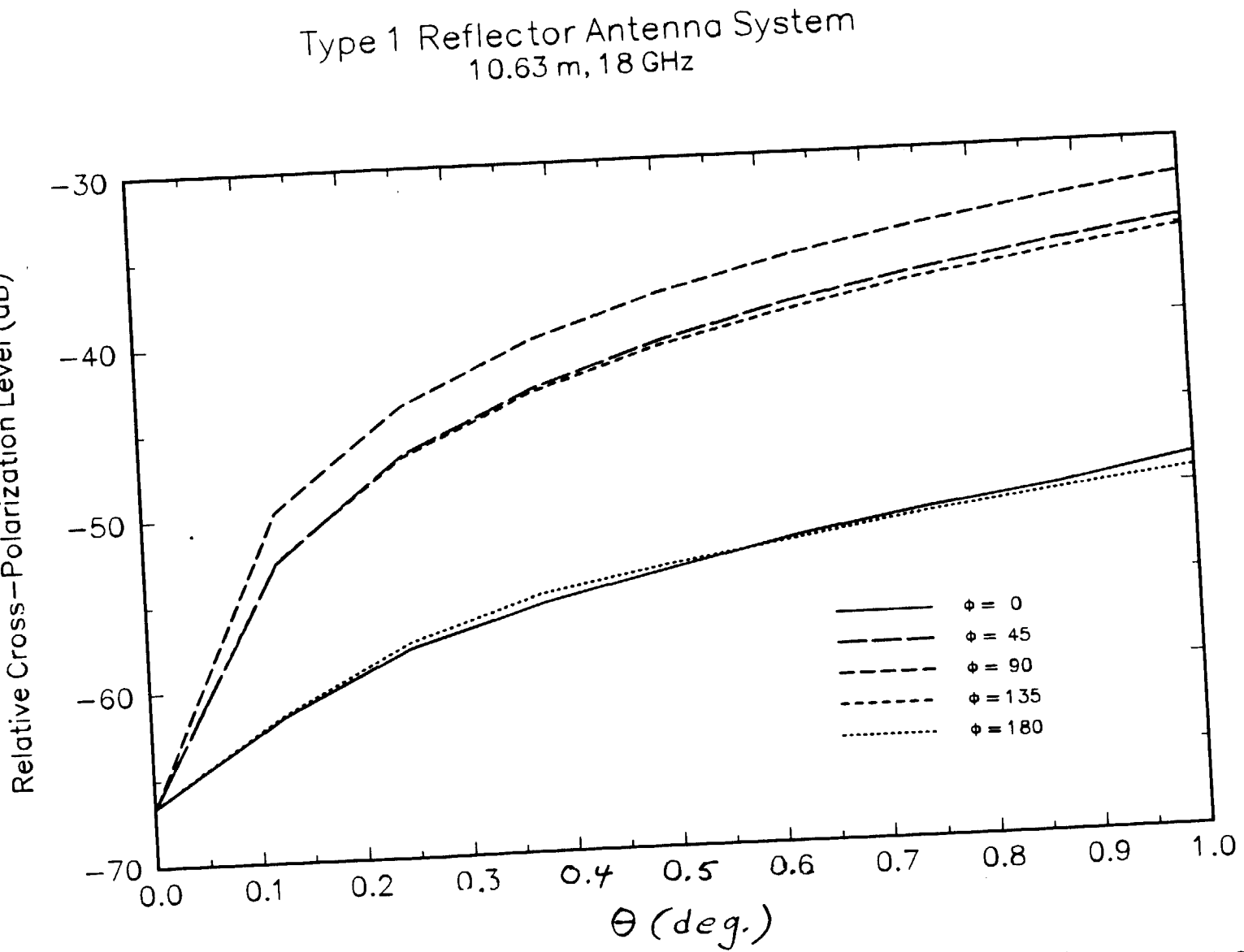

Figure 3.3-4. Type 1 reflector antenna system. Relative cross polarization versus scan angle.

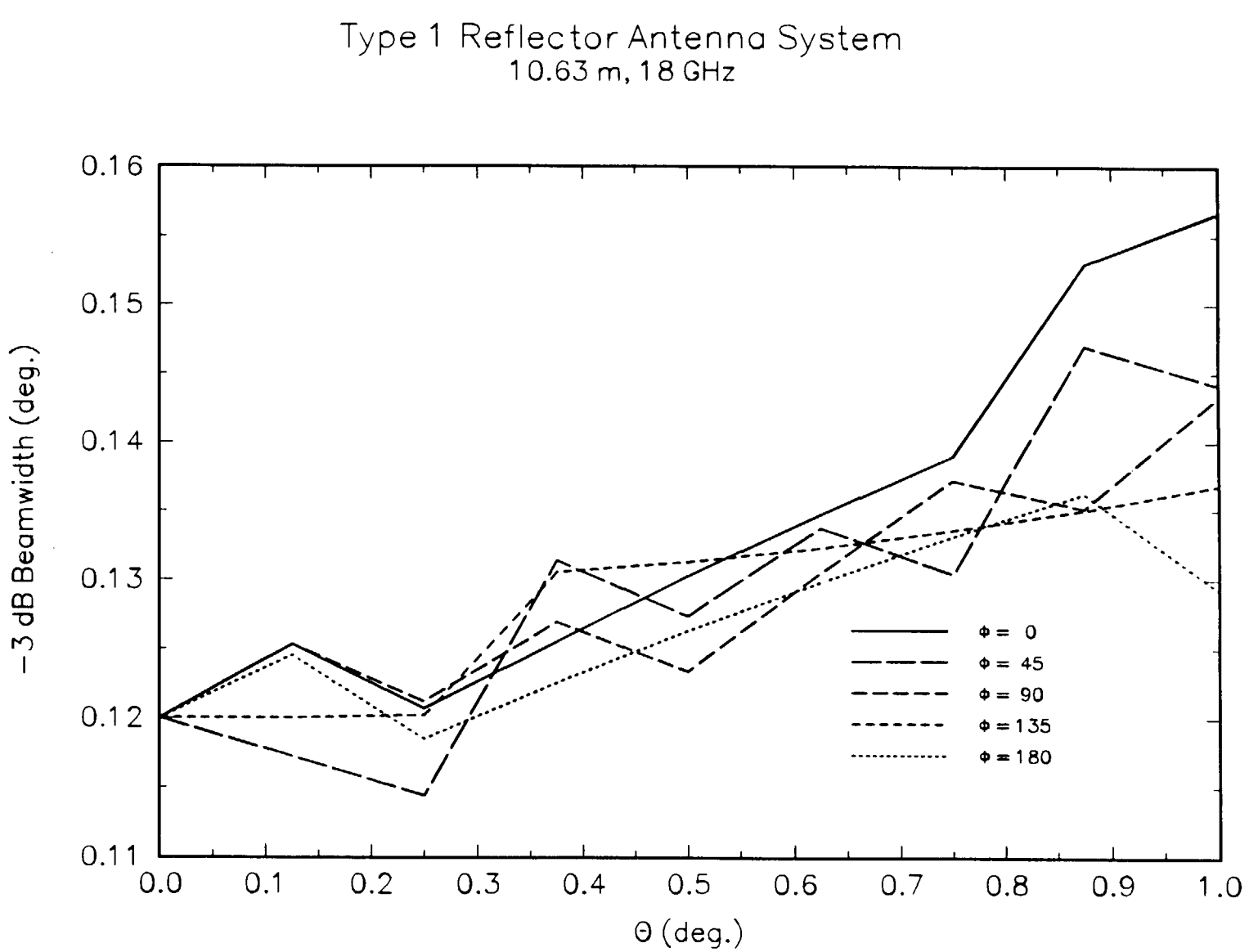

Figure 3.3-5. Half-power beamwidth versus main beam scan angle for the Type 1 reflector antenna system.

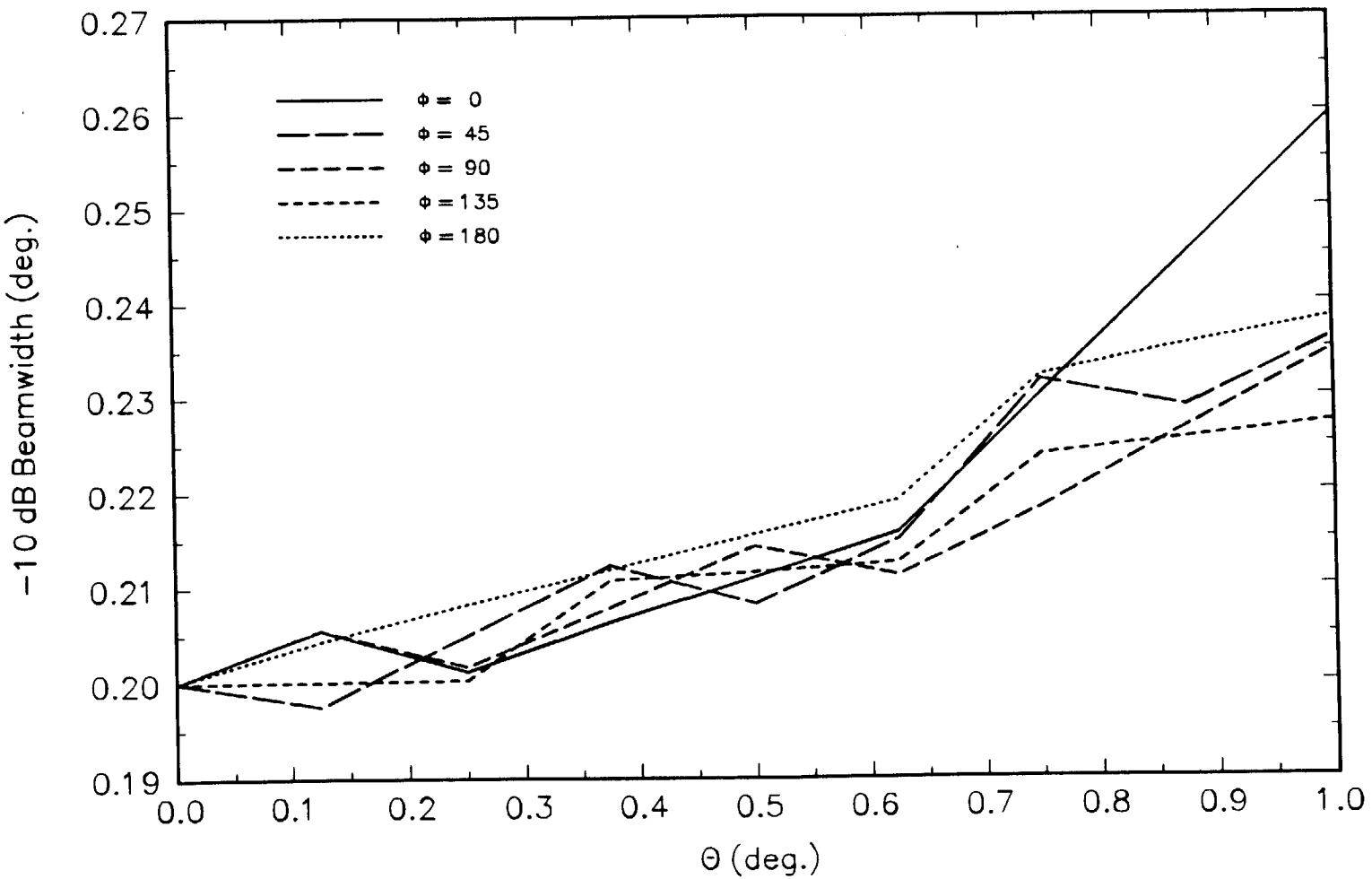

Figure 3.3-6. 10 dB-beamwidth versus main beam scan angle for the Type 1 reflector antenna system.

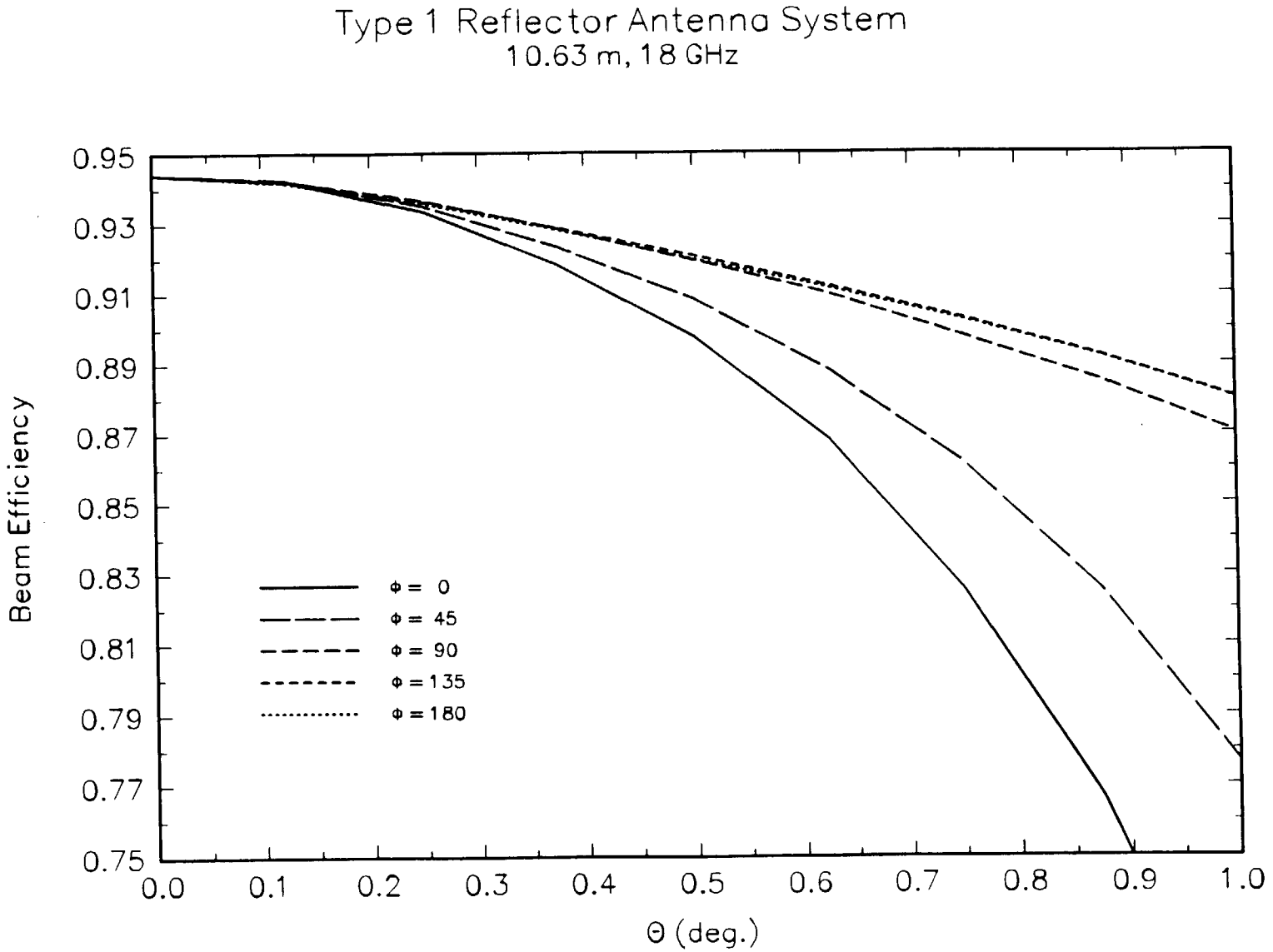

Figure 3.3-7. Type 1 reflector antenna system. Beam efficiency versus scan angle.

Table 3.3-1. Summary of Scan Performance for the Type 1 Reflector Antenna System.

Scan Direction		Electromagnetic Performance						
θ	φ	Gain (dB)	Efficiency (%)	HPBW (deg)	$BW_{10\ dB}$ (deg)	Beam Efficiency (%)	SLL (dB)	XPOL (dB)
0.00°	0°	64.74	74.19	0.12	0.20	94.43	-28.97	-66.59
0.25°	0°	64.61	72.00	0.12	0.20	93.38	-26.00	-57.91
0.25°	45°	64.60	71.83	0.11	0.20	93.57	-26.46	-46.59
0.25°	90°	64.59	71.67	0.12	0.20	93.68	-27.49	-43.79
0.25°	135°	64.52	70.52	0.12	0.20	93.65	-28.07	-46.73
0.25°	180°	64.51	70.36	0.12	0.21	93.60	-28.35	-57.54
0.50°	0°	63.98	62.28	0.13	0.21	89.77	-22.78	-53.90
0.50°	45°	64.05	63.29	0.13	0.21	90.85	-23.35	-40.59
0.50°	90°	64.13	64.47	0.12	0.21	91.96	-24.67	-37.80
0.50°	135°	64.06	63.44	0.13	0.21	92.09	-25.30	-40.86
0.50°	180°	64.06	63.44	0.13	0.22	91.99	-25.68	-53.64
0.75°	0°	62.90	48.57	0.14	0.23	82.50	-20.55	-50.89
0.75°	45°	63.25	52.64	0.13	0.23	86.16	-21.32	-37.05
0.75°	90°	63.58	56.80	0.14	0.22	89.79	-22.84	-34.40
0.75°	135°	63.62	57.32	0.13	0.22	90.30	-23.82	-37.50
0.75°	180°	63.62	57.32	0.13	0.23	90.26	-24.31	-51.15
1.00°	0°	60.86	30.36	0.16	0.26	68.31	-18.47	-48.38
1.00°	45°	61.93	38.84	0.14	0.24	78.68	-19.40	-34.58
1.00°	90°	62.95	49.13	0.14	0.23	87.01	-21.31	-32.02
1.00°	135°	63.13	51.21	0.14	0.23	88.02	-23.82	-37.50
1.00°	180°	63.16	51.56	0.13	0.24	88.00	-22.89	-49.18

table.331
10/21/92

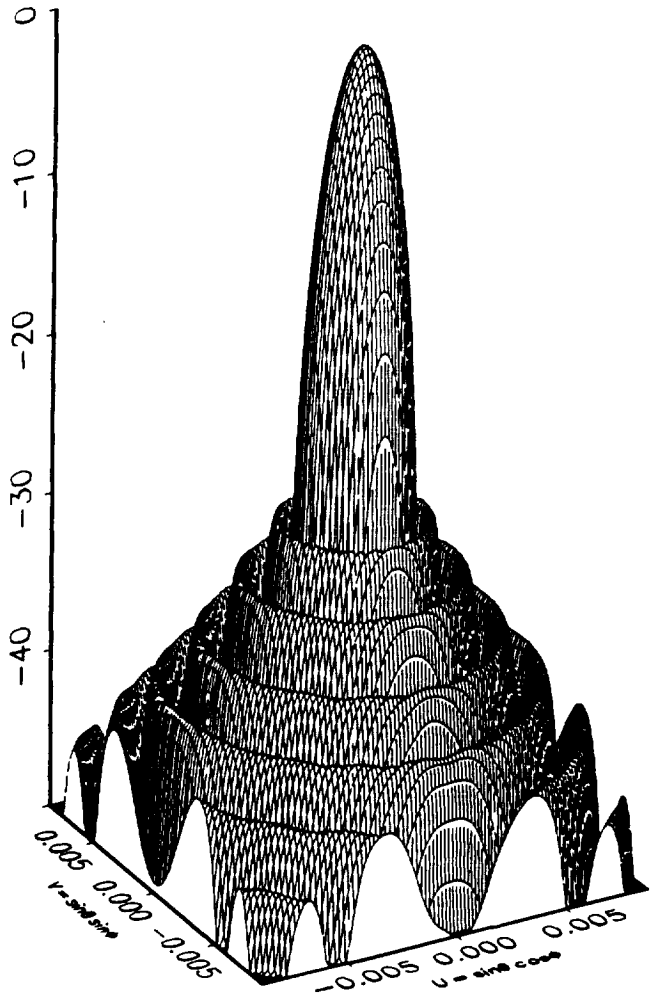

Figure 3.3-8. Boresight co-polarized antenna pattern for the Type 1 reflector antenna system. (a) Surface grid plot.

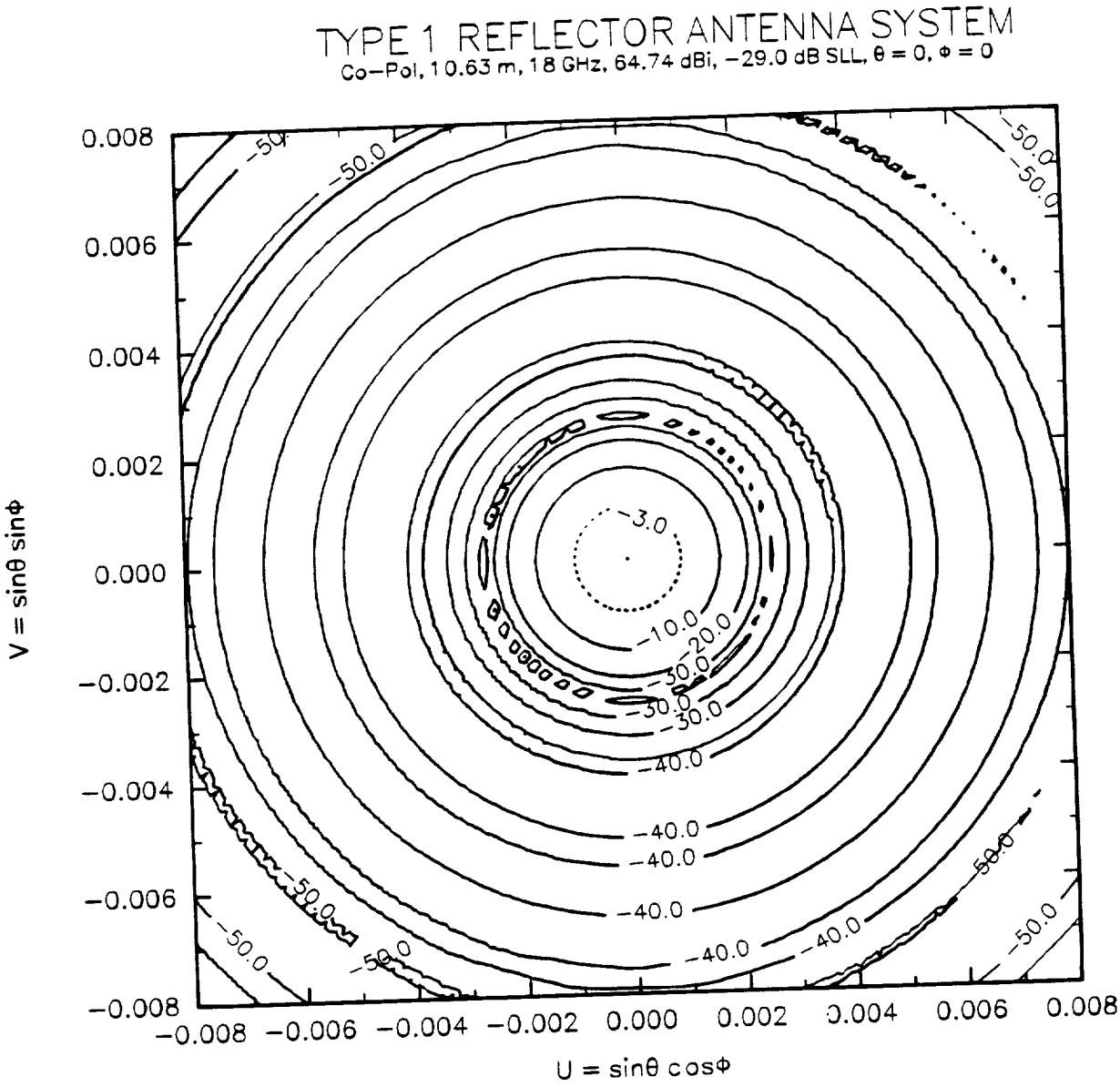

Figure 3.3-8. Boresight co-polarized antenna pattern for the Type 1 reflector antenna system. (b) Contour plot.

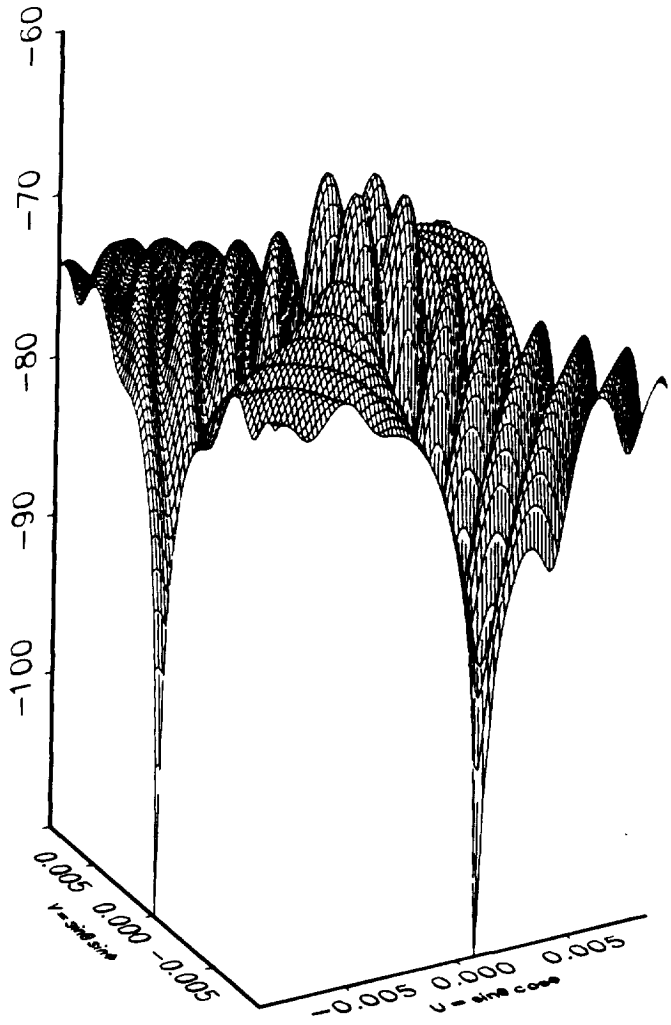

Figure 3.3-9. Boresight cross-polarized antenna pattern for the Type 1 reflector antenna system. (a) Surface grid plot.

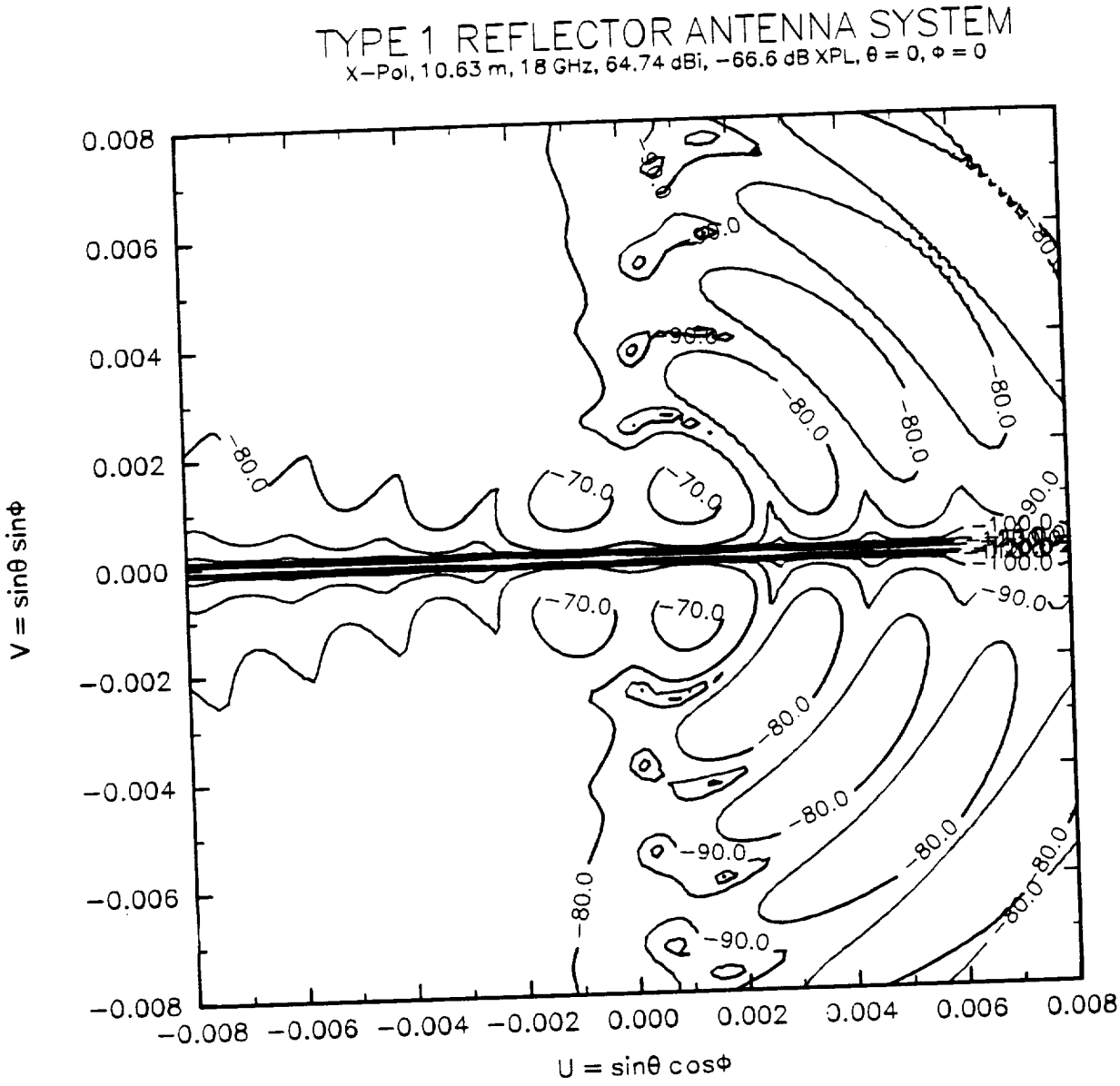

Figure 3.3-9. Boresight cross-polarized antenna pattern for the Type 1 reflector antenna system. (b) Contour plot.

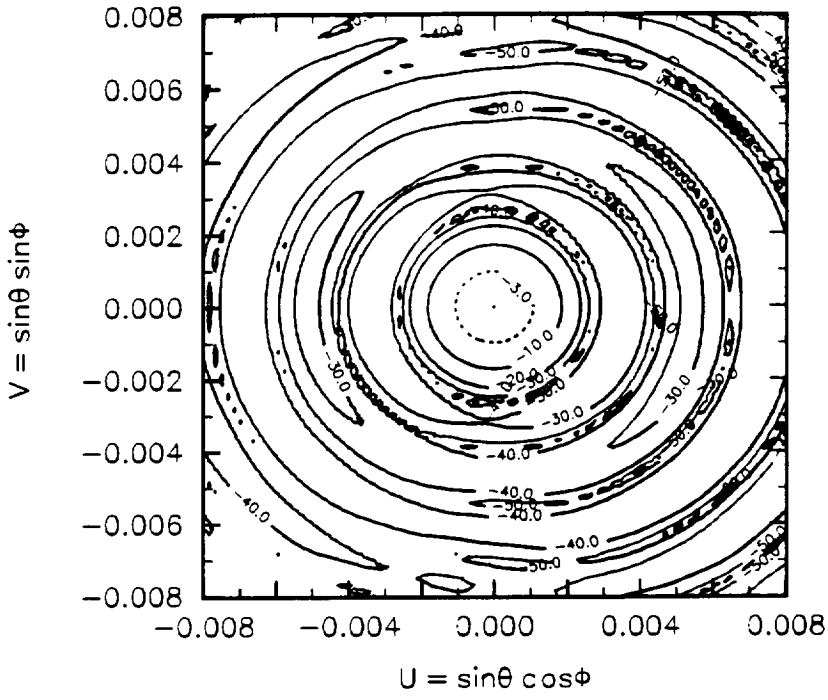

(a) Co-polarized pattern contour plot.

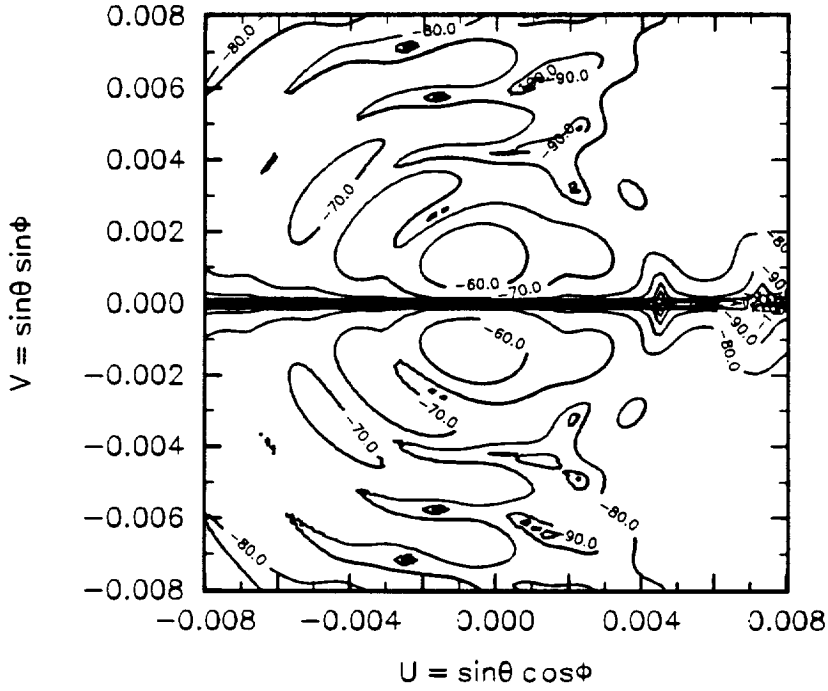

(b) Cross-polarized pattern contour plot.

Figure 3.3-10. Antenna pattern of the Type 1 reflector antenna system scanned to θ=0.5°, ϕ=0°.

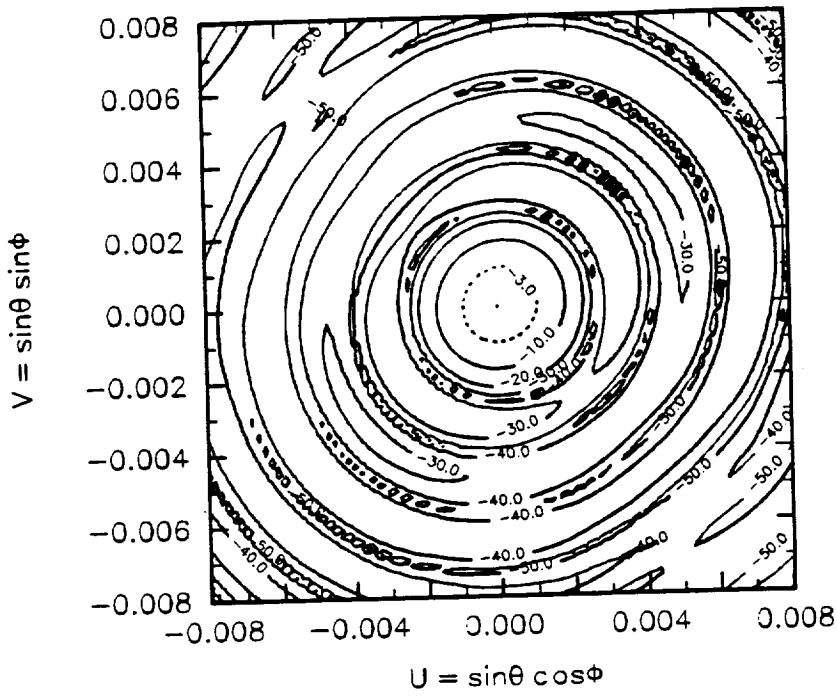

(a) Co-polarized pattern contour plot.

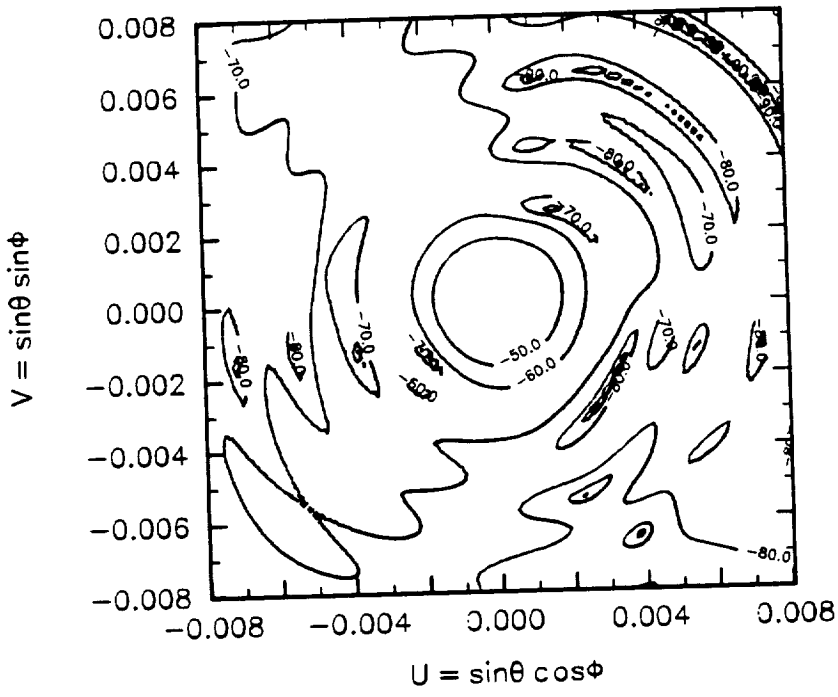

(b) Cross-polarized pattern contour plot.

Figure 3.3-11. Antenna pattern of the Type 1 reflector antenna system scanned to θ=0.5°, ϕ=45°.

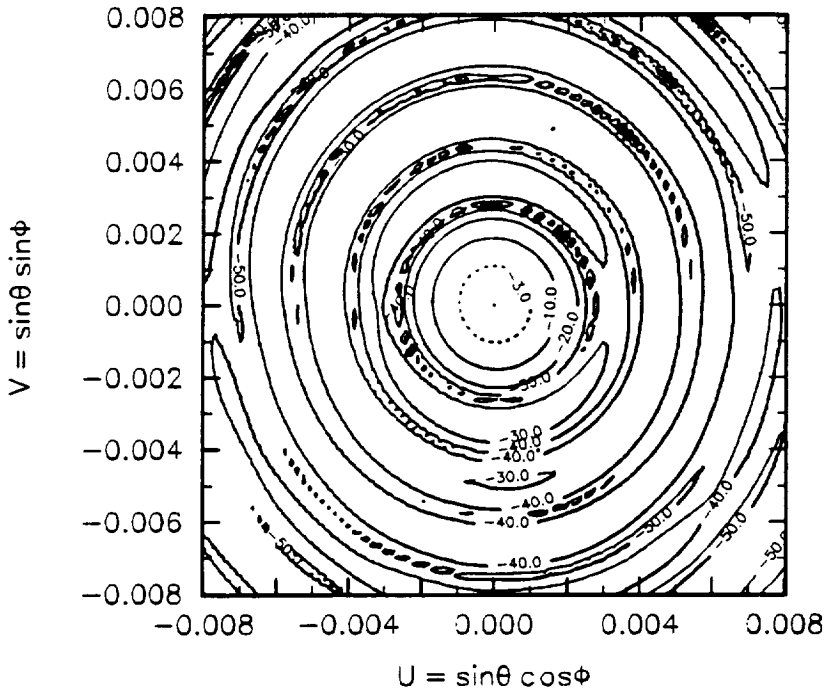

(a) Co-polarized pattern contour plot.

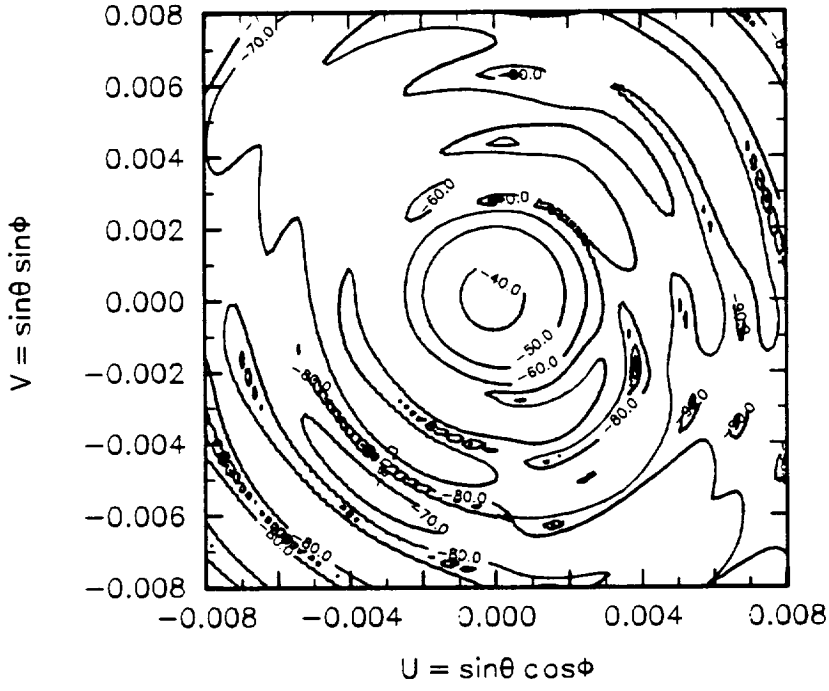

(b) Cross-polarized pattern contour plot.

Figure 3.3-12. Antenna pattern of the Type 1 reflector antenna system scanned to θ=0.5°, ϕ=90°.

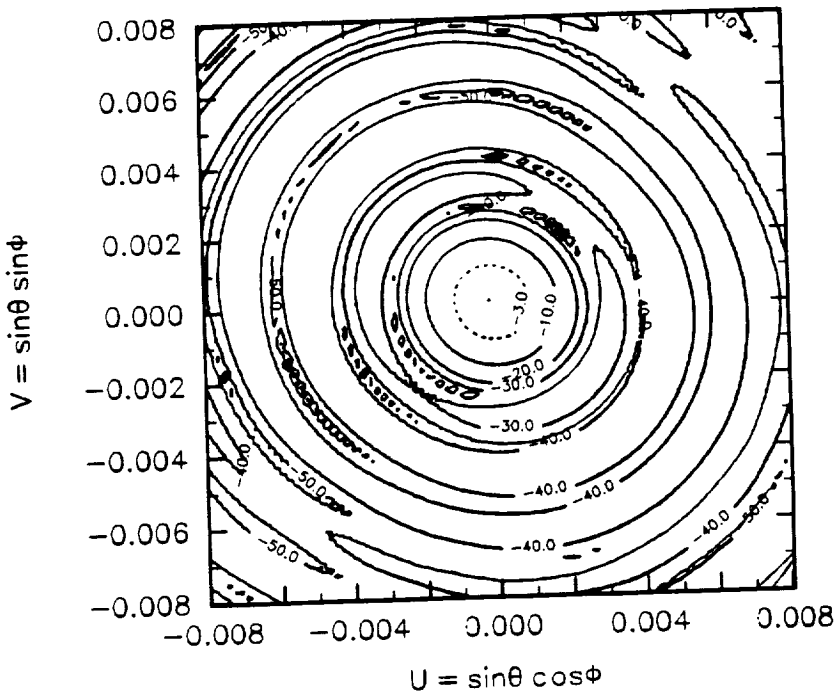

(a) Co-polarized pattern contour plot.

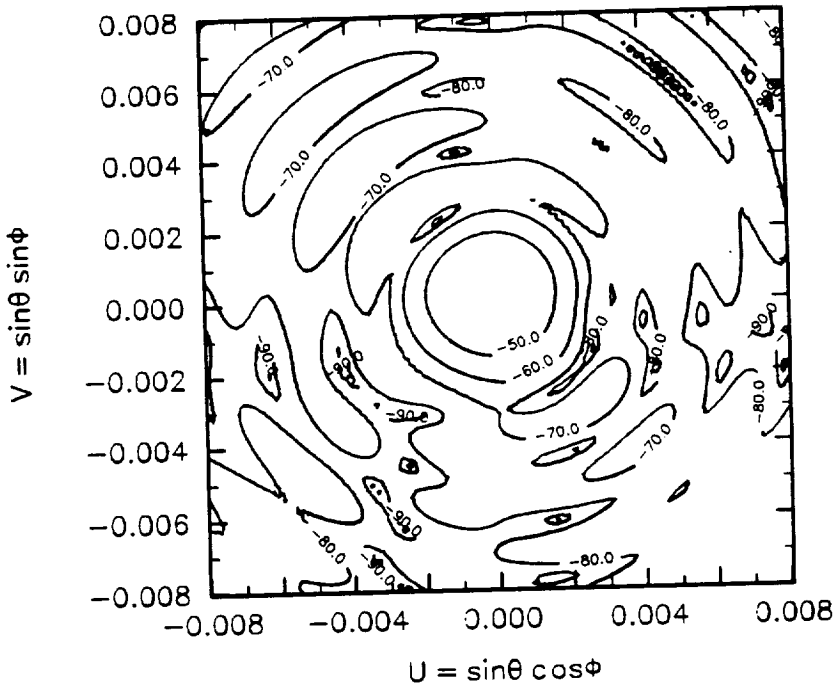

(b) Cross-polarized pattern contour plot.

Figure 3.3-13. Antenna pattern of the Type 1 reflector antenna system scanned to θ=0.5°, ϕ=135°.

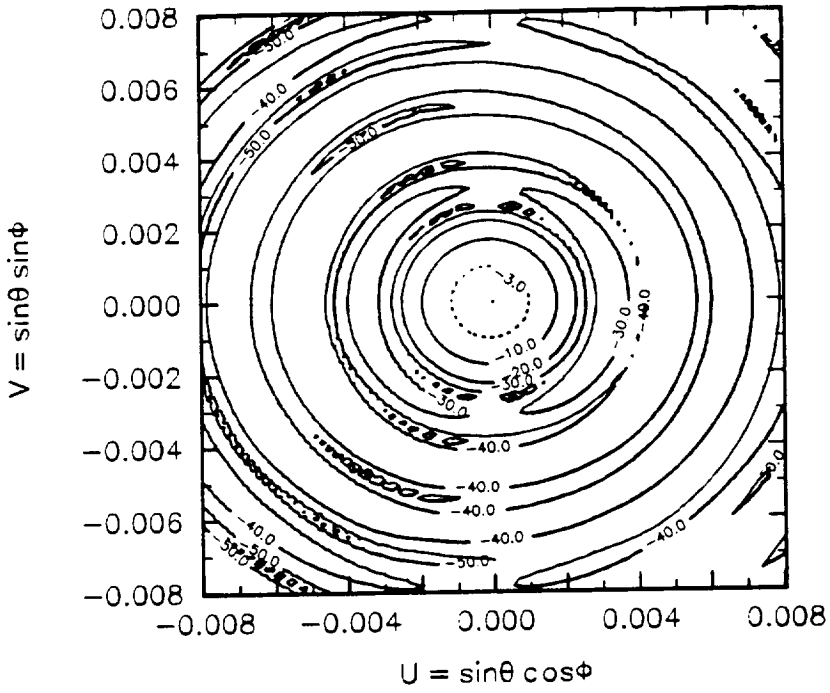

(a) Co-polarized pattern contour plot.

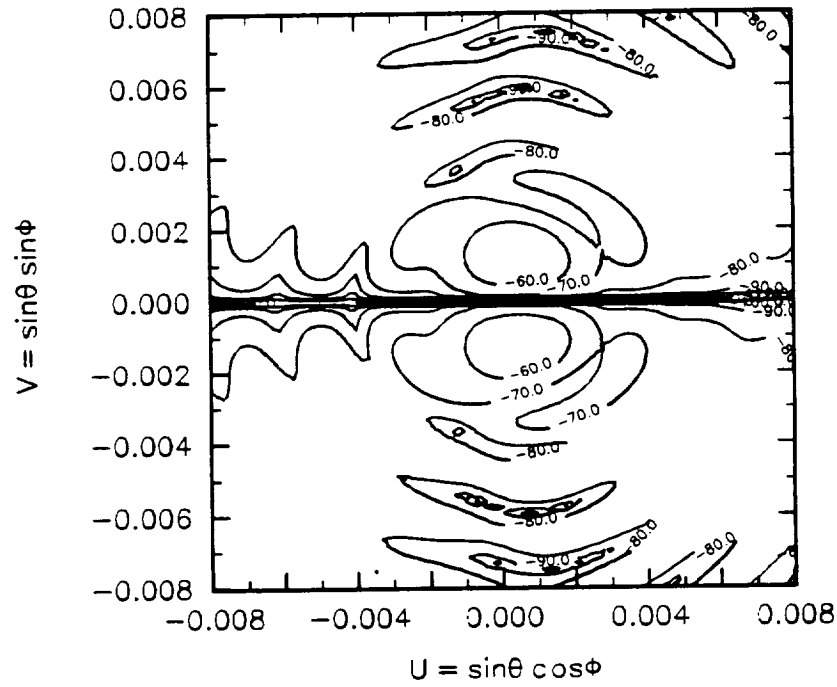

(b) Cross-polarized pattern contour plot.

Figure 3.3-14. Antenna pattern of the Type 1 reflector antenna system scanned to θ=0.5°, ϕ=180°.

Chapter 4

METHODS TO IMPROVE THE APERTURE EFFICIENCY AND SIMPLIFY THE MECHANICAL MOTION OF SPHERICAL MAIN REFLECTOR SCANNING ANTENNAS

Large reflector antenna systems with spherical main reflectors can be used in high gain, wide angle scanning applications. The performance of a spherical main reflector antenna system can be improved by using two subreflectors to correct for spherical aberration and to control the feed-to-aperture intensity mapping. However, due to the motion of the illuminated aperture area during scan, the aperture efficiency of a spherical main reflector system is limited. Moreover, the suboptics assembly, which consists of two subreflectors and the feed, must be translated and rotated during scan; therefore, the mechanical construction and operation of such systems is difficult. In the last semiannual report we introduced a method that maintains the illuminated aperture area constant during scan using two subreflectors which move as a unit and that correct for phase errors and produce an isotropic-to-uniform amplitude distribution mapping. The feed antenna must be tilted during scan. In this report we demonstrate a new design built on the previous spherical tri-reflector by adding a flat mirror to create the image of the suboptics assembly and to simplify the mechanical motion for scan by fixing the suboptics assembly and rotating the mirror. Practical designs and physical optics analysis results are also presented.

The principles of spherical main reflector system scan by mirror imaging is shown in Fig. 4-1. The basic system in Fig. 4-1a corrects the spherical aberration and provides isotropic-to-uniform mapping. A flat mirror is added to create the virtual image of the suboptics assembly as shown in Fig. 4-1c. Scan is achieved by rotating the mirror plane about the spherical center O, and therefore, rotating the virtual image of the suboptics assembly. The rotation of the virtual image of the suboptics assembly has the same effect as rotating a real one, so the main beam is scanned accordingly.

Based on this general theory for scanning spherical main reflector systems, we derived a system which fits the Bush model frame and is practical for GEO radiometer applications. This configuration has a spherical main reflector, two shaped subreflectors and a flat mirror. The geometric parameters of the configuration are given in Tables 1.2-1 and 1.2-2.

Physical optics analysis with GRASP7 code produced the performance values shown in Table 1.2-1. It shows that the spherical main reflector system can scan the

full $\pm 5^{\circ}$ region with little performance degradation. The mechanical size of the configuration is shown in Table 1.2-3. It was designed according to the requirements for the Bush model. The *area efficiency* (the main reflector area over the total area of all reflectors) of the spherical main reflector system of 70% is somewhat low but is a trade-off for the high scanning performance.

The most important feature of the proposed configuration is its simplicity in mechanical motion. Although there are two types motion possible in theory, the proposed spherical main reflector system has a scanning motion with the flat mirror rotating about two axes and translating along one line. The geometry for the motion can be seen in Fig. 4-1a. One axis is the z′ and the other axis is y′ which is perpendicular to the plane of the paper. The line of translation is the center ray between the subreflector and the virtual main reflector in Fig. 4-1a. In addition to motion of the mirror, the proposed configuration has an azimuth feed tilt motion, which maintains a constant illuminated area of the main reflector when scanning in the ϕ direction. This feed tilt motion makes it possible to achieve a 50% aperture efficiency as indicated in Table 1.2-1.

We are currently studying another possible motion of the mirror which can reduce the size of the mirror by half. The mirror motion under study involves a rotation of the flat mirror about one axis and a translation along one arc and one line. The rotational axis is the y′ axis perpendicular to the plane of Fig. 4-1a. The translational arc is the plane of x′ and y′ of Fig. 4-1a; the details of this translational arc is still under study and being optimized. The translational line is the same translational line discussed in the last paragraph. The advantage of this motion set is that it allows the mirror to move such that the mirror illumination is constant, and therefore, the size of the mirror can be reduced significantly. The details of these mirror motions will be reported in the future.

It is worthwhile to point out the trade-offs in the design of the proposed configuration. A one-dimensional azimuth feed tilt is used to improve the aperture efficiency in the proposed model. Aperture efficiency of 50% can be achieved with this scheme. However, higher aperture efficiency is possible if the feed can be tilted in both azimuth and elevation. According to our calculation, 70% aperture efficiency is possible. Of course, full tilting of the feed causes mechanical difficulties. In situations where there are mechanical difficulties associated with feed tilt that outweigh the high

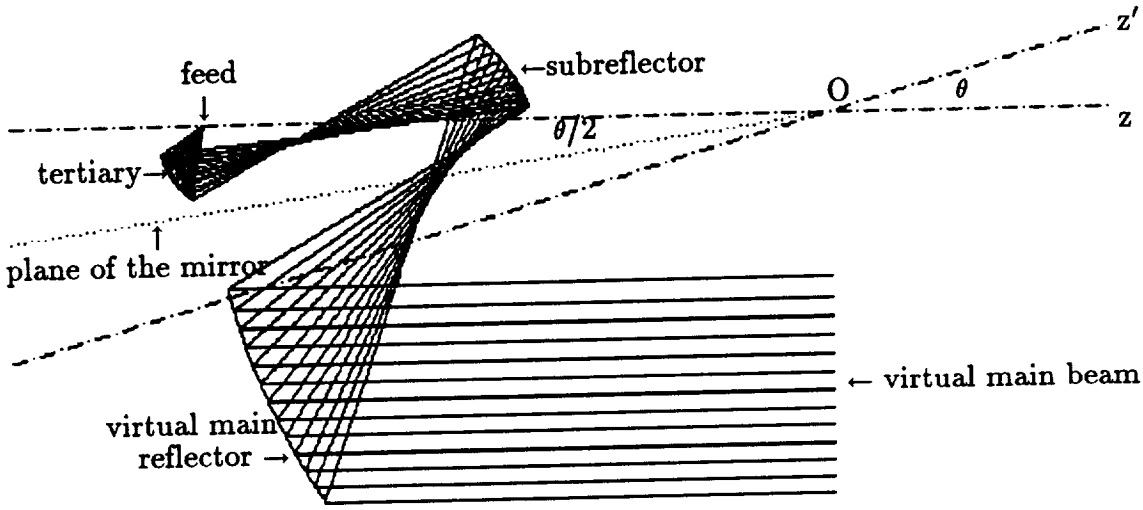

a. Basic spherical tri-reflector system.

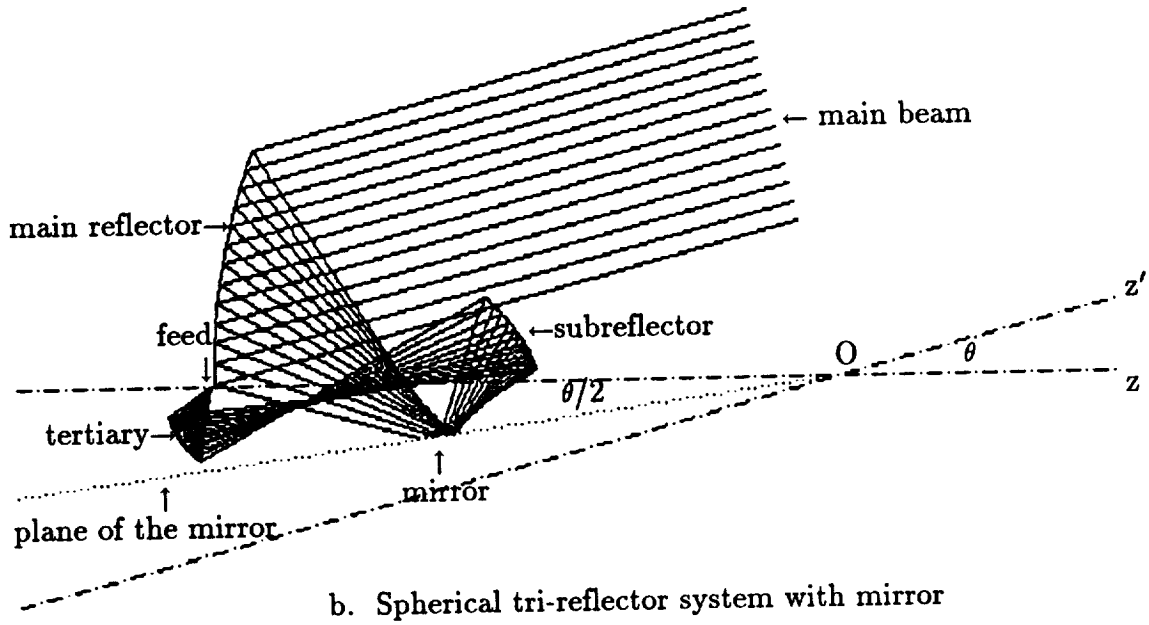

b. Spherical tri-reflector system with mirror

Figure 4-1. The scanning function of the mirror in a spherical tri-reflector system

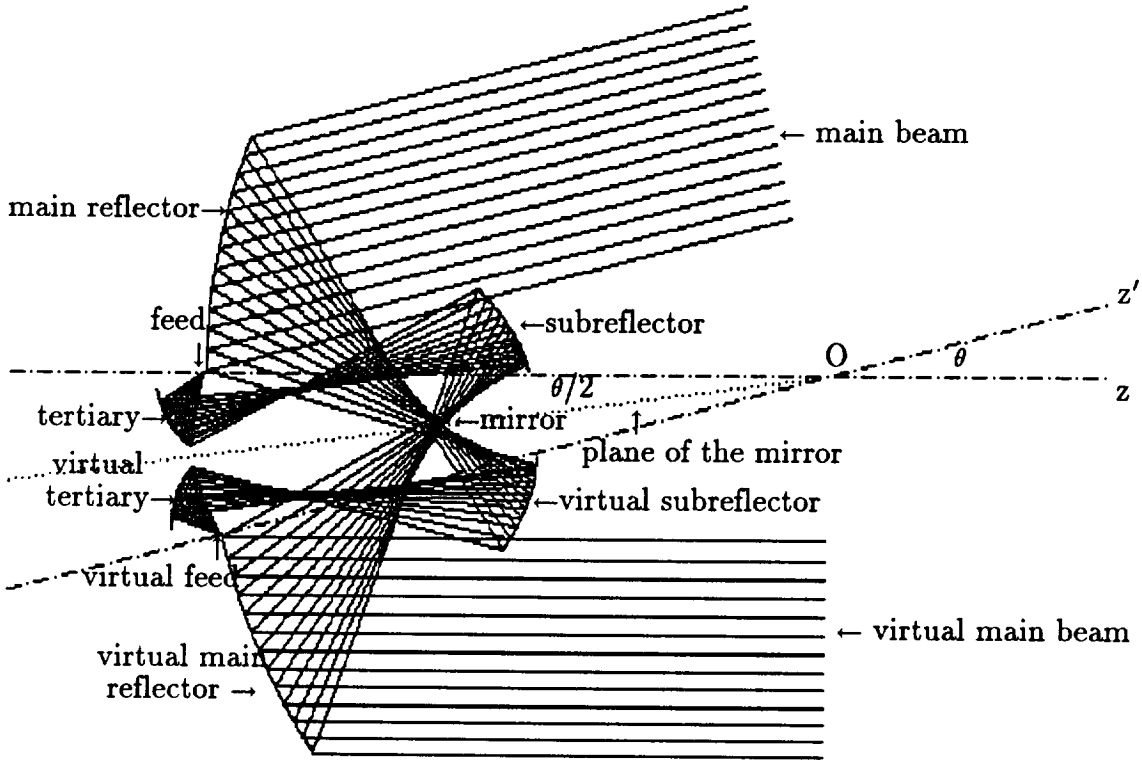

c. Illustration for mirror imaging scanning process

Figure 4-1. (continued)

aperture efficiency, the feed must be totally fixed. This, however, reduces the aperture efficiency to below 30%.

Another trade-off involved in designing the proposed model is the balance between main reflector spillover and main reflector size. With feed tilt permitted only in azimuth, the illuminated area on the main reflector can only be fixed when ϕ scan is performed; it moves when θ scan is performed. This leads to a need for oversizing the main reflector in order to reduce spillover. We managed to limit the size of the main reflector to 10×12m, as indicated in Table 1.2-1, but without significant spillover; in the proposed model the spillover causes as much as 0.4 dB gain loss at the scan limits. The PO analysis results at scan limits are listed in Table 4-1.

Error sensitivity analysis was performed at 15 GHz using GRASP7 and the results are listed in Table 1.2-4. It shows that for 0.5λ translational error and/or 0.1° rotational

Table 4-1

Scan Performance of the Spherical Tri-Reflector with a Flat Mirror at 18 GHz (Extrapolated from computations at 15 GHz)

Scan Direction		Electromagnetic Performance						
θ	φ	Gain (dB)	Aperture Efficiency (%)	HPBW (deg)	$BW_{10\ dB}$ (deg)	Beam Efficiency (%)	Sidelobe Level (dB)	XPOL (dB)
0°	0°	62.6	51%	0.12°	0.2°	93%	-28	-25
5°	0°	62.2	50%	0.15°	0.27°	92%	-28	-25
5°	90°	62.6	51%	0.12°	0.2°	93%	-28	-25
5°	180°	62.3	50%	0.12°	0.25°	92%	-27	-25

error for the reflectors and feed, the degradation of the performance is negligible. This, of course, does not include the error of the reflector surface distortion.

Our results show that the spherical tri-reflector system with flat mirror is a practical design. It has good electrical scan performance, simple motion, without introducing excessive mechanical tolerances. There are several advantages to the spherical configuration: the spherical main reflector can be constructed of identical facets, the mirror is flat, and the subreflectors are derived from axisymmetric shapes. The trade-off is that it requires more reflectors which results in increased size and weight of the entire structure.

Chapter 5
OPTIMIZATION OF REFLECTOR CONFIGURATIONS

5.1. Introduction

Most of reflector antennas are single focal point devices which are limited in scanning capability. Wide angle scanning of such reflectors are usually accomplished by moving the entire reflector as well as the feed assembly as in the case of radio telescopes. Limited scanning is often accomplished by displacing the feed antenna away from the focal point. Equivalently, the feed displacement is simulated with a phased array feed or by displacement of suboptics such as subreflectors or a beam waveguide. The phase error at the aperture of the reflector increases as the main beam is scanned away from the boresight direction. The limit of scan is determined by the maximum aperture phase error or the maximum beam degradation allowed for a particular design criterion. Both Type 1 and Type 2 systems are single focal point reflector systems.

A number of other configurations have been introduced to increase the scan capability of reflector antennas. These configurations can be grouped to two basic types: N-focal antennas and continuously scanning antennas. The former has exactly N focal points which are implemented with N reflector antennas. Rao [1] and Rappaport [2] have shown design techniques for symmetrical and offset bifocal antennas using two reflectors. The scanning in the bifocal systems are accomplished by moving the feed between the two focal points. The scan performance of bifocal antennas are maximum when the feed is located at one of the two foci, but the performance degrades away from the foci.

Continuous scan reflectors, on the other hand, do not have any exact focal point. They are designed such that the antenna performance remains constant throughout the scan range. This is accomplished by introducing some phase error in the on-axis direction while reducing the error away from the off-axis directions. Examples of continuous scan reflectors are the spherical reflector and the torus. A single spherical reflector fed by a feed antenna has spherical phase aberration at the aperture and thus, the radiation pattern has a slightly higher sidelobe level compared to a single paraboloidal reflector of comparable size. Scanning is accomplished by illuminating different portions of the reflector surface. The phase error, however, remains constant as the beam is scanned. Unfortunately, spherical reflectors have poor aperture efficiency due to oversizing of reflector surface, which is required for the scanning.

Shaped reflector antenna synthesis techniques for wide angle scan have been introduced by Rappaport [3] and Albertsen [4] for single and dual reflector systems,

respectively. These techniques approximate continous scan reflector by shaping the reflector surfaces so that the antenna radiation performance in M directions are maximized. Ideally, M is infinite; however, a reasonable solution can be obtained with sufficiently large M. For example, Albertsen has shown that an offset dual reflector antenna with 300 λ primary aperture diameter can be shaped to scan $\pm 7^{\circ}$ in a plane of asymmetry using M=5 [4].

The synthesis technique of Albertsen can be generalized and extended for N reflector systems. The problem can be most easily solved as minimization of an error functional derives from desired and calculated performance of the reflector antennas. Generalized Reflector Optimization Code (GROC) is a computer program under development at Virginia Tech which implements 3-dimensional multiple reflector synthesis technique for wide angle scan. Physical Optics Optimization Program (POOP) [5], which was written for 2-dimensional cylindrical reflectors, is a subset of GROC. There are several important components in the development of GROC. Two components which have been investigated are discussed in the following sections.

5.2. Error Functional Definition

To optimize reflector configuration for wide angle scanning a functional that represents the performance of the antenna at each of M scan directions must be defined. Similar to POOP, GROC uses field correlation to evaluate the reflector radiation performance. The field correlation η_c is a vector cross correlation of the received electric field $\vec{E}_r$ and the transmitted magnetic field $\vec{H}_t$ over the surface of a reflector. Explicitly, η_c is given by

$$\eta_c = \frac{\left(\int_S \vec{E}_r \times \vec{H}_t^* \, ds \right)^2}{\int_S \vec{E}_r \times \vec{H}_r^* \, ds \int_S \vec{E}_t \times \vec{H}_t^* \, ds} \tag{5-1}$$

where $\vec{E}_t$ and $\vec{H}_t$ are electric and magnetic fields that exist over the reflector surface S when the antenna is illuminated by a feed antenna, and $\vec{E}_r$ and $\vec{H}_r$ are received fields when the primary aperture of the antenna is illuminated by a plane wave from a desired scan direction. When integrals in (5-1) are taken over the aperture of primary reflector η_c becomes aperture illumination efficiency.

In addition to field correlation, GROC uses feed spillover efficiency η_f as another measure of reflector performance. Feed spillover is the ratio of power intercepted by a reflector to the total power transmitted by the feed. It is given by

$$\eta_f = \frac{\int_S \vec{E}_t \times \vec{H}_t^* \, ds}{\int_\Omega \vec{E}_t \times \vec{H}_t^* \, ds} \tag{5-2}$$

where Ω is the surface of a unit sphere. The overall efficiency of the reflector is given by

$$\eta_T = \eta_c \eta_f \tag{5-3}$$

Use of field correlation as the error functional in the synthesis is advantageous to other variables because it can be used directly to estimate the required change in the shape of reflector surfaces. Specifically, using the numerator of the (5-1) the reflector surface S is modified by

$$\Delta = \frac{\lambda}{4\pi}\left(\angle\vec{E}_r + \angle\vec{H}_t^*\right) \tag{5-4}$$

where Δ is the change in the shape of reflector surface in wavelengths and $\angle\vec{E}_r$ and $\angle\vec{H}_t^*$ are phases of the received and the transmitted fields in radians and λ is the wavelength of the fields. The estimation improves convergence of the minimization process.

5.3. Reflector Surface Definition

Many techniques have been considered to represent the reflector surfaces. This is one of the important variables that needs careful selection because it has direct impact on the type of solution that can be obtained from the synthesis. There are two types of surface representations:

1.) Discrete point representation where a surface is fit to a set of known points using a surface fit techniques, and

2.) A series expansion technique in which the surface is represented by sum of orthogonal functions.

The former has capability to represent any type of surface. However, it could result in a surface with non-continuous derivatives over the surface. The latter technique has limit in the type of surfaces that can be represented. On the other hand, a series can be chosen to guarantee a continuous derivative over the surface.

GROC uses a sum of Zernike polynomials to represent the reflector surfaces. Zernike polynomials, which are originally used in the optics to represent the phase aberration, are defined as

$$f(\rho, \phi) = \sum_m \sum_n B_m^n \, R_m^n(\rho) \, e^{jn\phi} \qquad \begin{array}{l} m = 0, 1, \ldots, \infty \\ n = \begin{cases} \pm 1, \pm 3, \ldots, \pm m, & m \text{ odd} \\ 0, \pm 2, \ldots, \pm m, & m \text{ even} \end{cases} \end{array} \tag{5-5}$$

where the radial functions in (5-5) are given by

$$R_m^n(\rho) = \sum_{l=0}^{\frac{m-n}{2}} = \frac{(-1)^l\,(m-l)!}{l![(m+n)/2-l]!\,[(m-n)/2-l]!\rho^{m-2l}} \qquad (5\text{-}6)$$

Zernike polynomials are defined within the unit circle. Most reflectors have somewhat circular rim shapes, and thus the domain of the polynomials matches well with that is the reflectors. In addition, Zernike polynomials have continuous derivatives within the unit circle.

5.4. Future Work

Future work on optimization of reflector configurations for wide scanning include the following:

(1) Completion and verification of GROC program.

(2) Investigation on improving the rate of convergence in the minimization process.

(3) Application of GROC on Type 1 and Type 2 systems.

(4) Application of GROC on LEO ice mapper.

5.5. References

1. B.L.J. Rao, "Bifocal dual reflector antenna," *IEEE Trans. Antennas Propagat.*, pp. 711-714, Sept. 1974.
2. C.M. Rappaport, "An offset bifocal antenna design for wide-angle beam scanning," *IEEE Trans. Antenna Propagat.*, vol. AP-32, pp. 1196-1204, Nov. 1984.
3. C.M. Rappaport, C.P. Craig, "High aperture efficiency symmetric reflector antenna with up to 60 degrees field of view," *IEEE Trans. Antennas Propagat.*, vol. 39, pp. 336-344, March 1991.
4. N.C. Albertsen, K. Pontoppidan, S.B. Sorensen, "Shapping of dual reflector antennas for improvement of scan performance," in *Proc. IEEE Int. Symp. Antennas Propagat.*, pp. 357-360, June 1985.
5. W.L. Stutzman, et al., *Feasibility Study of a Synthesis Procedure for Array Feeds to Improve Radiation Performance of Large Distorted Reflector Antennas,* Semiannual Status Report, March 1992.

Chapter 6
RADIOMETRIC ARRAY DESIGN

This project is reported on in detail in a separate annual report. This chapter summarizes the work on this effort since the last semi-annual report.

Development of models for the array and noise scene have progressed to the evaluation stage. Calculations of array noise temperature for simple circular noise sources were performed to evaluate spatial coherence effects and network effects on radiometric measurements. The geometry for these calculations is given in Fig. 6-1. This study using simple circular noise sources is valuable since it suggests an experiment that can be used to verify the models we have developed. Also, we now believe that the array-fed reflector antenna can be modeled as an array observing a circular source the diameter of the reflector, at least for the low earth orbit observing scenario.

To illustrate spatial coherence effects, we modeled the two-, four-, and nine-element rectangular grid arrays (2 x 2 , 4 x 4, and 9 x 9 arrays with equal spacings along the principal axes) observing a 4-m diameter noise source *at a fixed distance* as the interelement spacing was varied from 0.5 λ to 2.0 λ. The observation frequency was 10 GHz. Results are shown in Fig. 6-2. The array noise temperature of all three arrays goes through a cyclical variation as the interelement spacing is increased. It appears, however, that the larger the array size, the more sensitive the array noise temperature is to interelement spacing.

Other calculations were made for arrays with fixed element spacing as the distance between the array and the noise source were varied. Results for two-element arrays are shown in Figs. 6-3 and 6-4. Figure 6-3 shows the results for two-element arrays with 0.5 λ and 1.0 λ spacings observing a 4-m diameter source. Figure 6-4 is for the same arrays but with a 20-m diameter source. The differences between these two plots illustrates the importance of understanding the spatial coherence effects of extended incoherent noise sources. The important parameter for spatial coherence effects is the angular separation between array elements *as viewed from the source.* The smaller the noise source extent, the broader, in terms of angle, the mutual coherence function (MCF). The 4-m noise source results indicate an array that is measuring a noise source with a high degree of spatial coherence. The 20-m source results are indicative of an array that is essentially incoherent. It is only at large distances from the source that the angular separation between elements is small enough for the MCF to be significant.

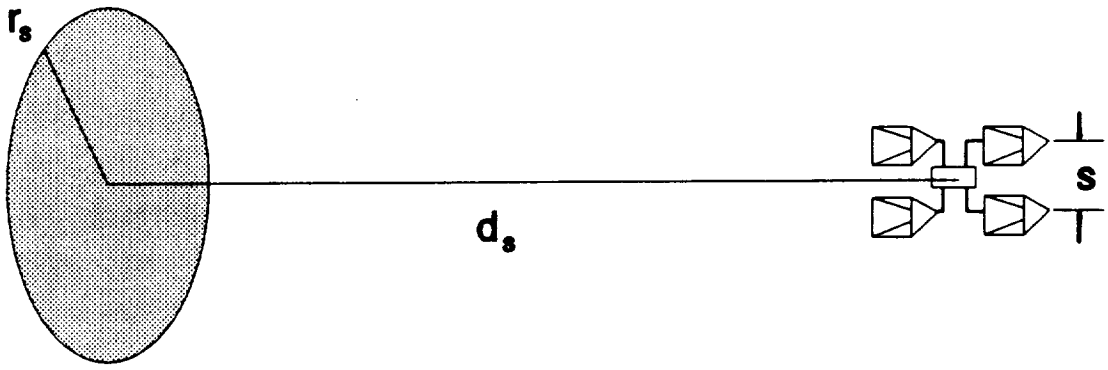

Figure 6-1. Geometry for array noise calculations.

Using the models we developed, we have also begun examining the effects of the array and feed network on radiometric measurements. We have made calculations on the effects of mutual coupling in the array, feed network mismatches, and feed coupling (or cross coupling within the feed network). An interesting result that is obvious from the network model is that mutual coupling has no effect on the noise temperature measurement *unless there are mismatches or coupling in the feed network.* For simplicity we used two element arrays to study these effects.

Our network model is completely generalized so that any array and feed network that can be characterized by its scattering parameters can be analyzed. However, the range of values that can be assigned to the scattering parameters makes it difficult to quantify the network effects since the scattering parameter effects are inter-related. We have attempted to best/worse case effects when possible.

We have studied mutual coupling effects with feed network mismatches only and with feed network mismatches and feed coupling. The mutual coupling phase was varied over 360° in order to observe the effects of phase on the measurement. Figure 6-5 shows the results for a feed network mismatch of -10 dB as the mutual coupling coefficient was varied from -50 dB to -10 dB. The two curves show the minimum and maximum array noise temperature. As the mutual coupling becomes greater (<-25 dB) the uncertainty in the measurement due to phase becomes greater. This effect is increased as the feed

mismatch becomes worse.

Figure 6-6 shows the array noise temperature versus mutual coupling with effects of feed coupling and feed mismatches included. For this case a feed coupling of -20 dB and feed mismatches of -10 and -20 dB were used. The effect is similar to that of only feed mismatches but the uncertainty due to the mutual coupling phase is greater.

While the formal project time period for the array feed studies ended August 15, work will continue on fully developing and, hopefully, verifying the models for radiometric arrays. Future efforts will concentrate on more fully exploring the network effects on array noise measurements and quantifying these and other sources of measurement uncertainty.

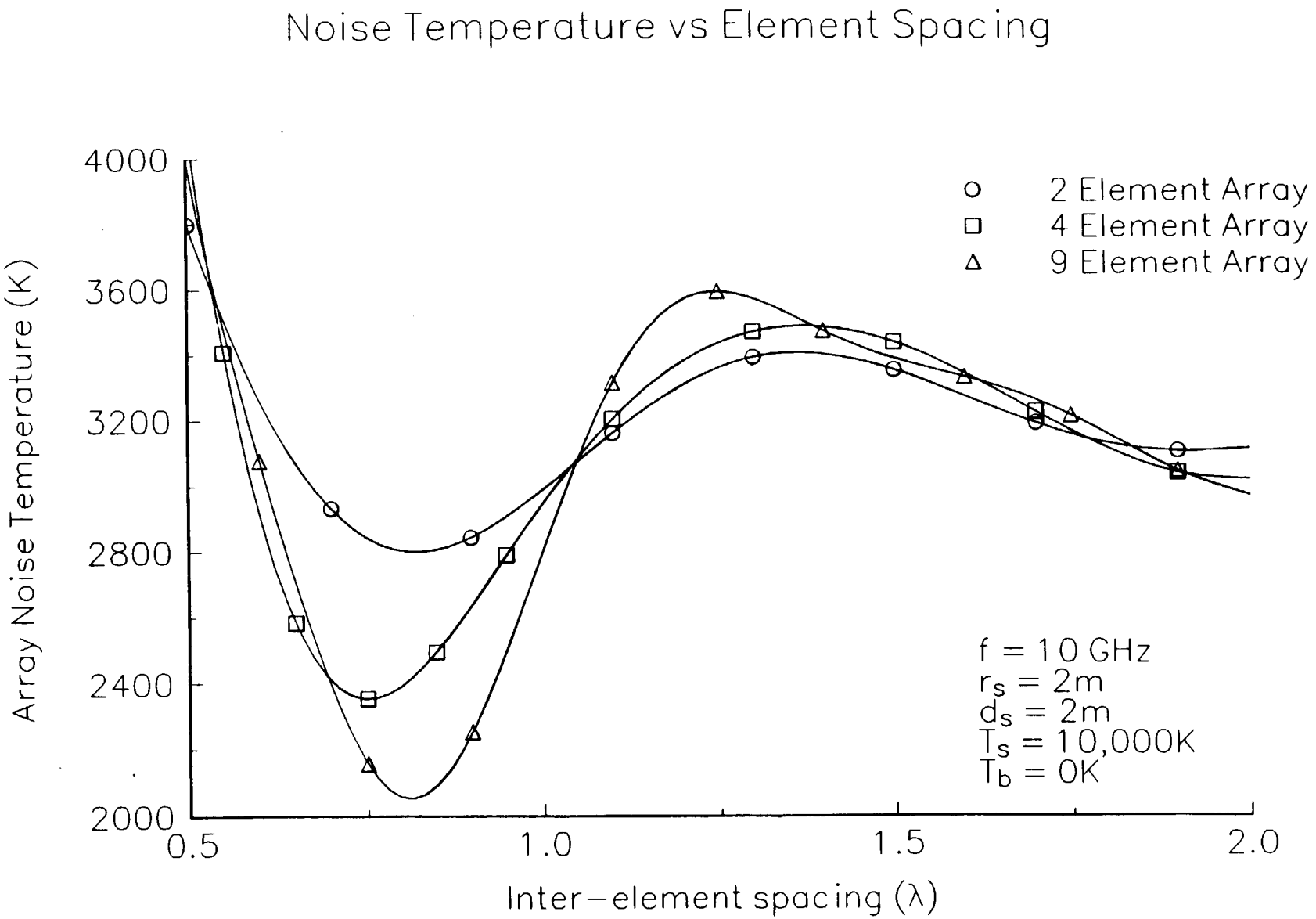

Figure 6-2. Array noise temperature versus array interelement spacing for fixed source-array spacing.

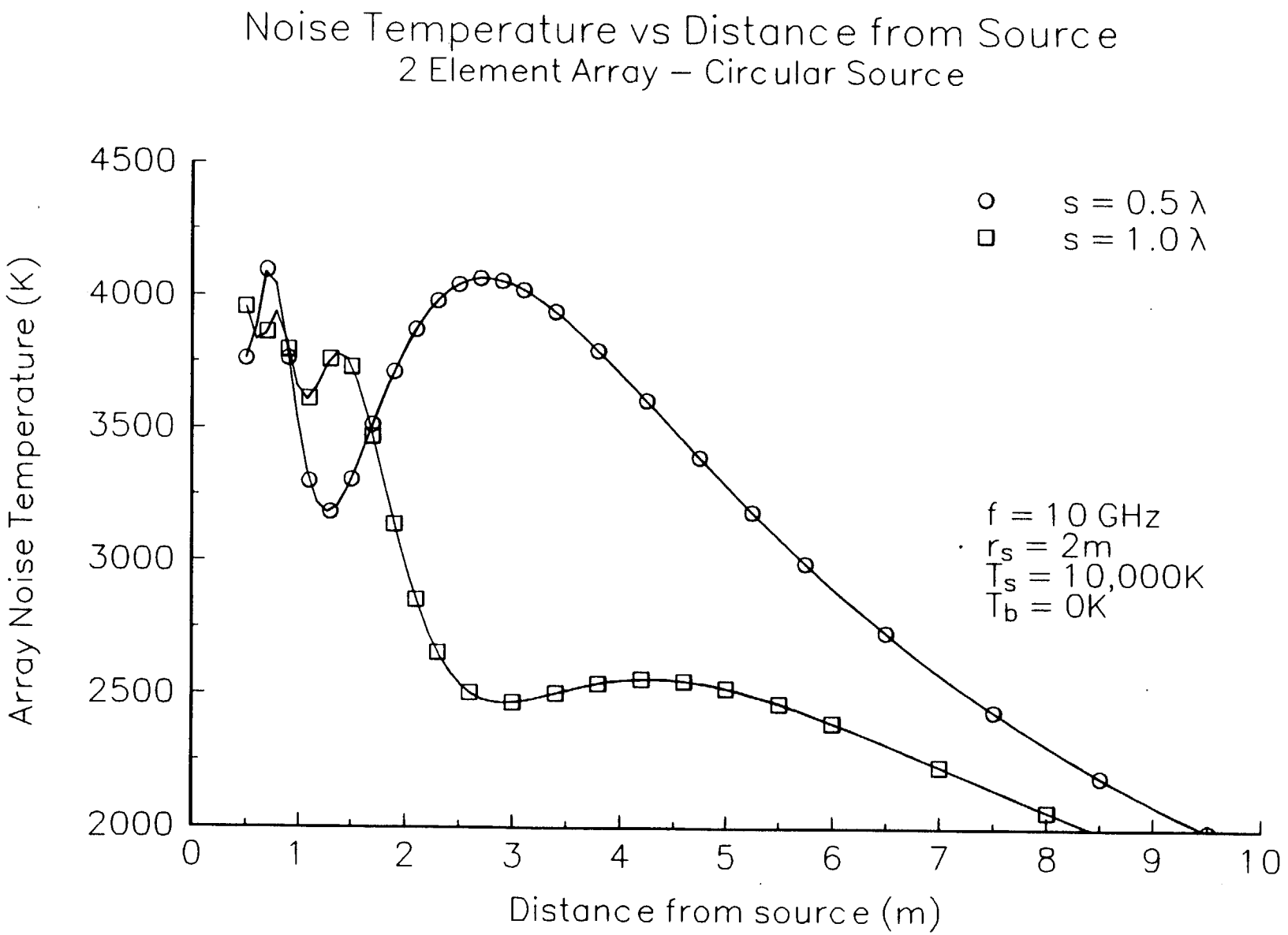

Figure 6-3. Array noise temperature versus source-array spacing for two element arrays with 0.5 λ and 1.0 λ interelement spacing and 4-m noise source.

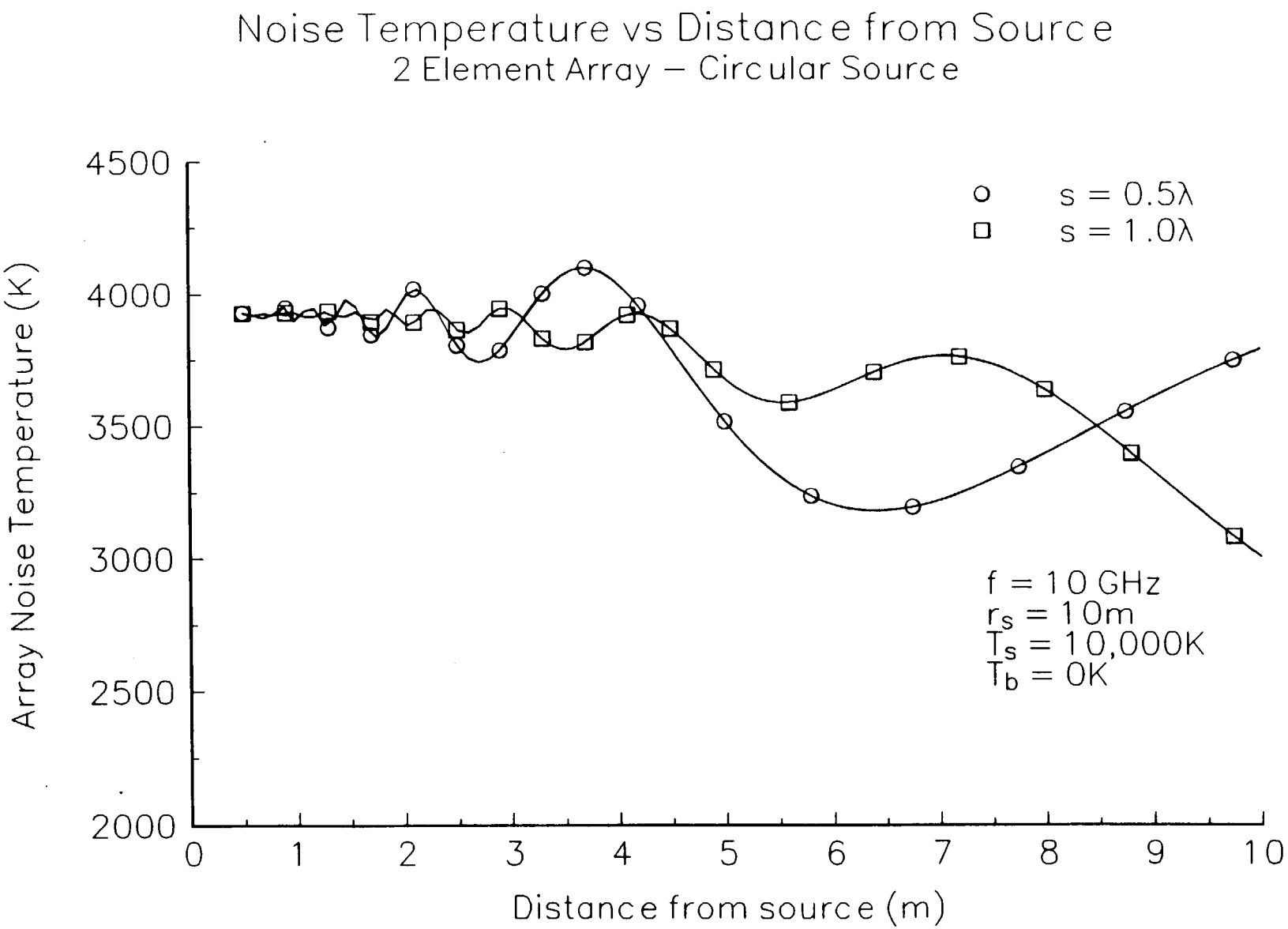

Figure 6-4. Array noise temperature versus source-array spacing for two element arrays with 0.5 λ and 1.0 λ interelement spacing and 20-m extent noise source.

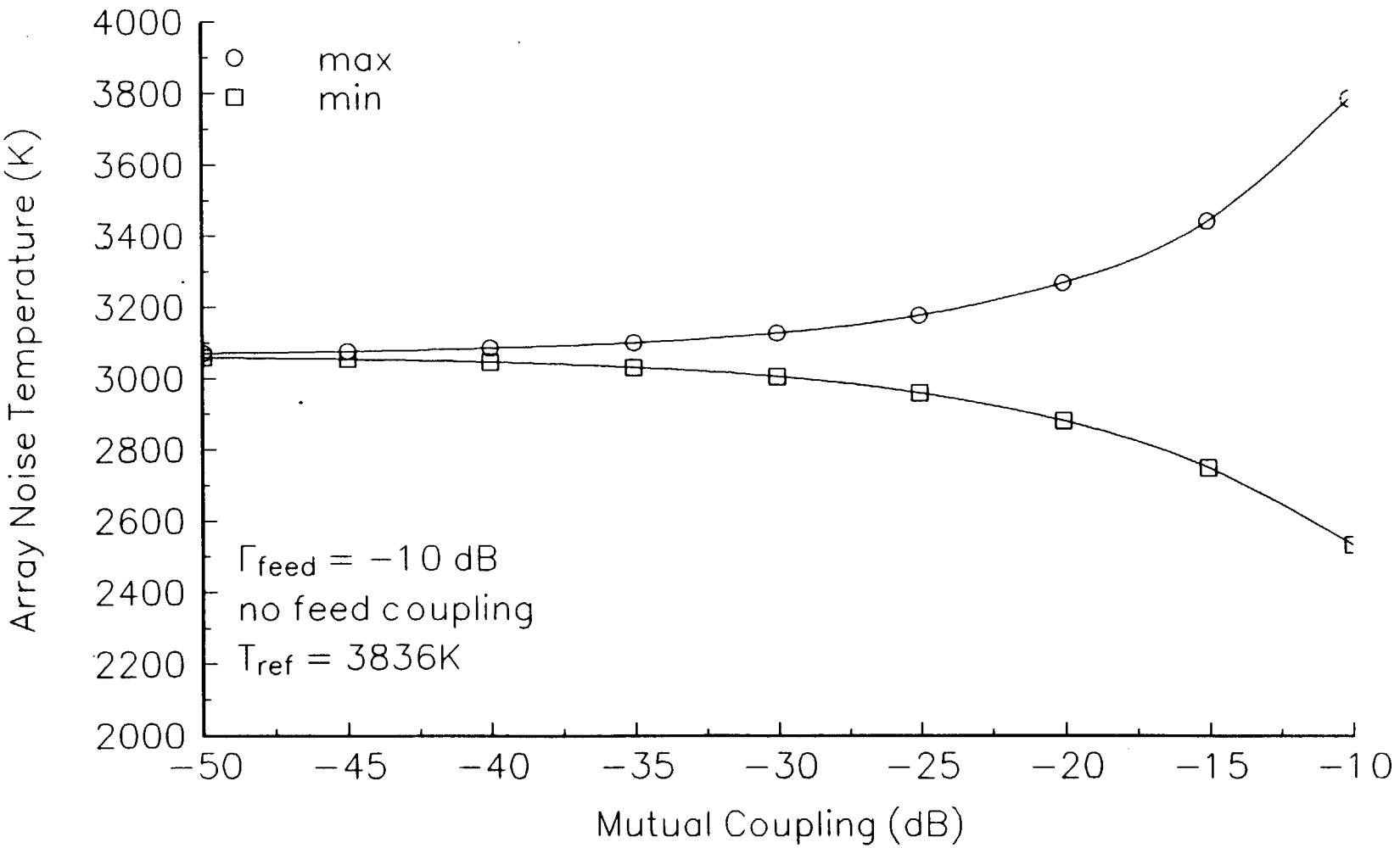

Figure 6-5. Array noise temperature versus mutual coupling for fixed -10 dB feed network mismatch and no feed coupling.

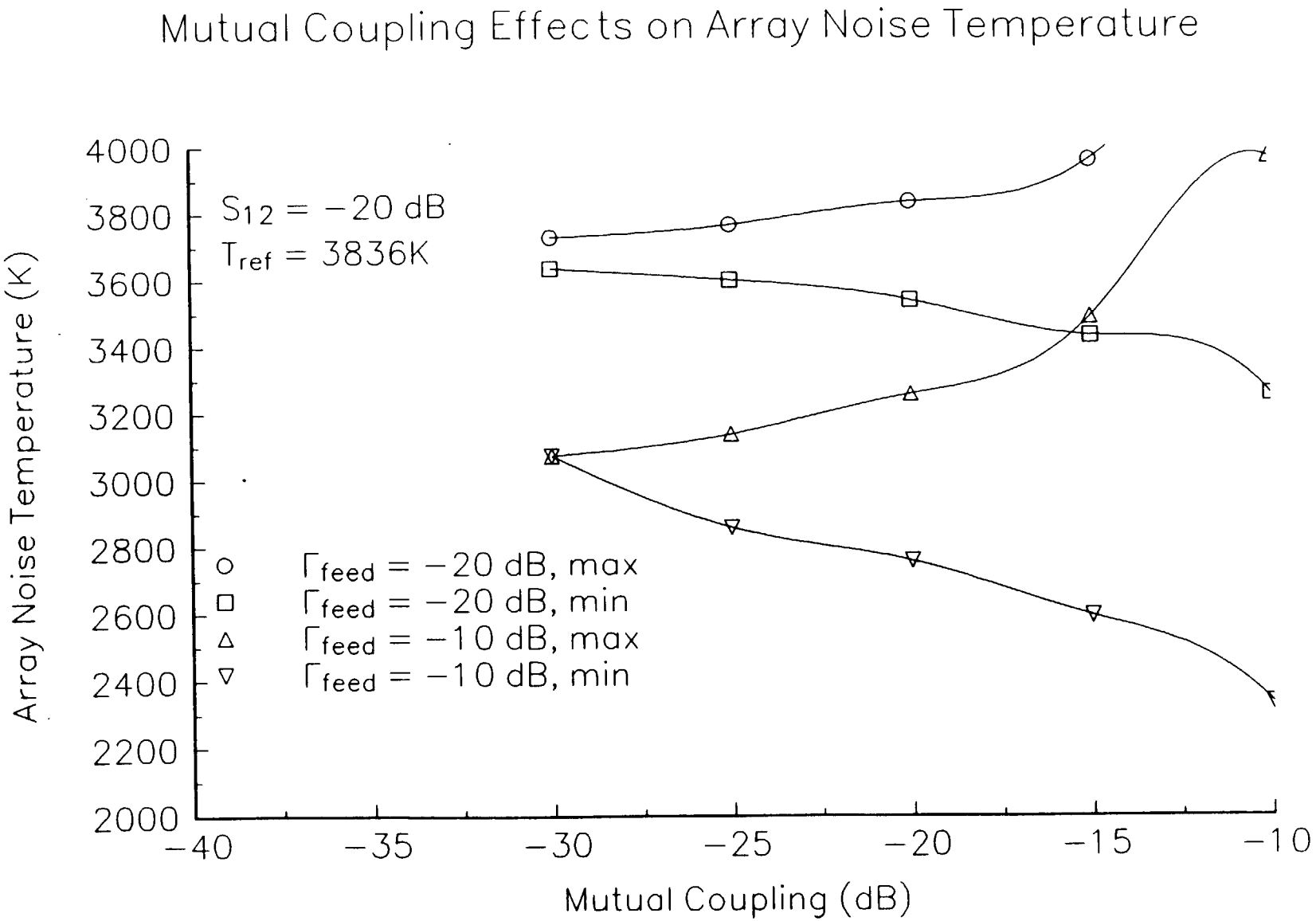

Figure 6-6. Array noise temperature versus mutual coupling for feed coupling of -20 dB and feed mismatches of -10 and -20 dB.

Chapter 7
PUBLICATIONS

7.1. Recent Publications

7.1.1. Conferences

(1) P.C. Werntz, K. Takamizawa, W.L. Stutzman and P. Foldes, "Wide Scanning Tri-Reflector System with an Elliptic Subreflector and Moving Tertiary Reflector," URSI Radio Science Meeting (Boulder, CO), January 1992.

(2) R.M. Barts, W.A. Davis and W.L. Stutzman, "A Multiport Noise Model with Applications to Remote Sensing Arrays," URSI Radio Science Meeting (Boulder, CO), January 1992.

(4) P.C. Werntz, M.C. Bailey, K. Takamizawa and W.L. Stutzman, "Array-Fed Reflector Antenna Systems for Wide Scan," AP-S Symposium, July 1992.

(5) K. Takamizawa, P. Werntz, and W.L. Stutzman, "Optimization of Multiple Reflector Antenna Configuration for Wide Angle Scan," AP-S Symposium, July 1992.

(6) J. LaPean and W.L. Stutzman, "Beam Scanning in the Cassegrain Antenna System by the use of Subreflector Movement," AP-S Symposium, July 1992.

7.1.2. Papers

(1) W.T. Smith and W.L. Stutzman, "A Pattern Synthesis Technique for Array Feeds to Improve Radiation Performance of Large Distorted Reflector Antennas," IEEE Trans. on Ant. and Prop., Vol. 40, pp. 57-62, January 1992.

7.1.3. Theses, dissertations, reports

7.2. Planned Publications

7.2.1. Conferences

(1) B. Shen and W.L. Stutzman, "Beam Efficiency Evaluation of Large Reflector Radiometer Antennas," URSI Meeting, Jan. 1993.

(2) B. Shen and W.L. Stutzman, "Methods to Improve the Aperture Efficiency and Simplify the Mechanical Motion of Spherical Main Reflector Scanning Antennas," URSI Meeting, Jan. 1993.

7.2.2. Papers

(1) B. Shen and W.L. Stutzman, "Design of Scanning Tri-Reflector Antennas with High Aperture Efficiency," submitted, July 1992.

(2) J.W. LaPean and W.L. Stutzman, "Wide Scanning Dual Reflector Antennas Using a Moving Subreflector," to be submitted.

(3) K. Takamizawa and W.L. Stutzman, "Optimization of Multiple Reflector Antenna

Performance Under Parameter Constraints," IEEE Trans. on Ant. and Prop., to be submitted.

(4) R.M. Barts and W.L. Stutzman, "Noise Modeling of Array Antennas with Applications to Microwave Remote Sensing," IEEE AP-S Trans., to be submitted.

(5) P. Werntz and W.L. Stutzman, "Wide Scanning Tri-Reflector Antenna System Using Moving Tertiary Reflector," IEEE Trans. on Ant. and Prop., to be submitted.

(6) B. Shen and W.L. Stutzman, "Design of a Scanning Spherical Tri-Reflector Antenna with a Mirror," to be submitted.

7.2.3. Theses, dissertations, reports

(1) J.W. LaPean, "Beam Scanning in the Cassegrain Antenna System Using a Moving Subreflector," Master's Thesis, Virginia Tech, October 1992.

(2) K. Takamizawa, "Optimization of Multiple Reflector Antenna Performance Under Parameter Constraints," Ph.D. dissertation, Virginia Tech, December 1992.

(3) P.C. Werntz, "Novel High Gain Wide Scan Tri-Reflector Antennas," Ph.D. dissertation, October 1992.

(4) B. Shen, "Design of High Efficiency Spherical Reflector Antennas with Multiple Subreflector for Wide Scan," Ph.D. dissertation, August 1993.

(5) R.M. Barts, "Applications of Array Antennas to Microwave Remote Sensing," Ph.D. dissertation, August 1993.

Distribution

1. NASA Langley
   M.C. Bailey
   T.G. Campbell
   L.C. Schroeder
2. NASA (3 copies)
   NASA Center for Aerospace Information
   P.O. Box 8757
   Baltimore/Washington International Airport, MD 21240
3. Peter Foldes, Inc.
4. VPI & SU Sponsored Programs (cover sheet)